2013-09-13

Four Phenomena Observed on Microseismic Data

St-Onge, Andre Maurice

UNIVERSITY OF CALGARY

Four Phenomena Observed on Microseismic Data

by

André Maurice St-Onge

A THESIS

SUBMITTED TO THE FACULTY OF GRADUATE STUDIES

IN PARTIAL FULFILMENT OF THE REQUIREMENTS FOR THE

DEGREE OF DOCTOR OF PHILOSOPHY

DEPARTMENT OF GEOSCIENCE

CALGARY, ALBERTA

SEPTMEBER, 2013

Abstract

Passive seismic data recorded in observation wellbores for hydraulic fracture monitoring are usually used to detect P- and S-wave arrivals from induced microseismic events. The time arrivals for these events are used to compute source locations to build a fracture location map. Along with these arrivals are a number of other coherent signal and noise events. The primary objective of this thesis is to examine various other types of coherent signal and noise on four microseismic datasets. This thesis is made up of four separate studies.

The first study examines numerous coherent low-frequency (<100 Hz) arrivals characterized by conspicuous dispersion and quasi-linear moveout. Their apparent velocities and dispersion characteristics are consistent with Lamb waves, an elastic guided wave that propagates within finite media such as plates or cylindrical casing. Lamb waves may be used for monitoring degradation of casing cement over time.

The second study examines two datasets to characterize frequency shifts in discrete narrow passbands caused by wellbore acoustic transmissivity due to geophone clamping. The passbands changed throughout two fracture stimulations in proportion to the hydraulic fracture pressure. Analytical and finite-element models suggest that these temporal variations may be caused by a relative change in geophone clamping force as the pressure external to the wellbore varies. This sensitivity suggests that passive seismic monitoring can be used for downhole detection of relative stress changes.

The third study focuses on frequency content variations of 20 high S/N P- and S-wave events. The 20 events were grouped into four clusters based upon a geolocation algorithm and event cross-correlations. Spectral analysis shows variation in the signal within event sets. A 2-D elastic finite-difference simulation using a layered model shows that this variation could be ascribed to path effects associated with propagation of the signal from the source to the receivers.

The fourth study examines a potential long-period long-duration (LPLD) seismic event and analyzes the phenomena in detail. LPLD events observed on microseismic data have been likened to deep low-frequency tremor attributed to slow-slip processes along pre-existing fractures or strike-slip regimes at subduction zones. The event may be the result of hydraulic fracture fluid leak-off out of the intended zone into a pre-existing fracture.

Preface

This thesis investigates phenomena recorded on microseismic data that have scant discussion in the literature. The intention is to describe the phenomena using physical principles and to investigate how their properties may be used to increase our understanding of the subsurface. This thesis includes two papers submitted for publication.

Chapter two has been submitted for publication in the journal Geophysics and is currently in review:

St-Onge, A., and Eaton, D. W., 2013, Lamb waves recorded in wellbores and their potential to predict cement bond failure

Chapter three is an expanded version of the following paper that has been submitted for publication in the journal Geophysics and is currently in review:

St-Onge, A., Eaton, D. W., and Pidlisecky, A., 2013, Borehole acoustic transmissibility and frac-induced stress changes

Acknowledgements

Thank you to Dr. David Eaton accommodating me when accommodation was required. Your approachability and positive outlook is refreshing to see in a university environment.

Thank you to Dr. Adam Pidlisecky for simply asking, “Does it change over time?”

I give an exploding hand pound to Maria and Agnieszka.

Finally, thank you to my family for all their support and patience, especially to my wife Jen. We met 34 years ago at university and had study dates; thank you for still engaging me in that pastime. I give thanks for David, Heather and Thomas, and Jessica, Amanda and Peter. May you grow up strong and healthy and be prosperous.

Sponsors of the Microseismic Industry Consortium are thanked for their support. Special thanks are extended to EOG Resources, Inc., ARC Resources Ltd. and ConocoPhillips Canada for the use of their microseismic datasets. Financial support for the borehole acoustic transmissibility study was provided by a grant from the Canada School for Energy and Environment (CSEE). This support is greatly appreciated.

This thesis is dedicated to Laura.

Table of Contents

Abstract i
Preface ii
Acknowledgements iii
Dedication iv
Table of Contents v
List of Tables viii
List of Figures ix
Epigraph xxi

CHAPTER ONE: INTRODUCTION 1
1.1 Introduction 1
1.2 Hydraulic fracturing 6
1.3 History of downhole seismic recording 10
1.4 Borehole and surface microseismic monitoring 11
1.4.1 Acquisition 11
1.4.2 Processing and interpretation 13
1.4.3 Summary 15
1.5 Signal and noise 16
1.6 Signal and noise recorded on borehole microseismic data 17
1.7 Thesis outline 19

CHAPTER TWO: - LAMB WAVES RECORDED IN WELLBORES AND THEIR POTENTIAL TO PREDICT CEMENT BOND FAILURE 21
2.1 Summary 21
2.2 Introduction 21
2.3 Characteristics of Lamb waves 24
2.4 Microseismic Data Examples 27
2.5 Discussion 39
2.6 Conclusions 44

CHAPTER THREE: BOREHOLE ACOUSTIC TRANSMISSIBILITY AND FRACTURE-INDUCED STRESS VARIATIONS 46
3.1 Summary 46
3.2 Introduction 47
3.2.1 Hydraulic fracturing and stress measurements 47
3.2.2 Cylindrical shell vibration 48
3.2.3 Acoustical response of a steel rod and a drill string 49
3.2.4 Acoustical response of a cased wellbore with clamped geophones 51
3.3 Vibrations of a resonating cylinder and borehole acoustic transmissibility 52
3.3.1 Vibration 52
3.3.2 Acoustic-transfer matrix 53
3.3.3 Comb-spectrum filters 54
3.3.4 COMSOL modelling 55
3.3.5 Analytical and finite-element modelling results 55
3.4 Data 58

3.4.1 Observations 58
3.5 Discussion 78
3.5.1 Alternative models 79
3.5.2 Physical model 83
3.5.3 COMSOL model 85
3.6 Conclusions 92

CHAPTER FOUR: P-WAVE PATH EFFECTS IN MICROSEISMIC DATA RECORDED IN A DEEP WELLBORE 94
4.1 Summary 94
4.2 Introduction 94
4.3 Observations 100
4.4 Finite-Difference Modeling 110
4.5 Discussion 115
4.5.1 Recorded data and the finite-difference model 115
4.5.2 Simple Finite Difference Model 117
4.5.3 Wedge Model 125
4.5.4 Depth Grouping 127
4.6 Summary 132
4.7 Conclusions 133

CHAPTER FIVE: A LONG-PERIOD LONG DURATION MICROSEISMIC EVENT 134
5.1 Summary 134
5.2 Introduction 134
5.2.1 Pembina Cardium Formation 136
5.2.2 Hydraulic Fracturing 139
5.2.3 Seismic Data 140
5.3 Observations 141
5.4 Discussion 149
5.4.1 Comparison to a recorded earthquake 149
5.4.2 Contractor report for pressures 151
5.4.3 Contractor located microseismic events 152
5.4.4 Interpreted fault location compared to other results 154
5.5 Conclusions 158

CHAPTER SIX: CONCLUSIONS 160
6.1 Summary of Thesis Work 162
6.1.1 Lamb Waves 162
6.1.2 Borehole Acoustic Transmissivity 163
6.1.3 Path Effects on Microseismic Data 163
6.1.4 Long-period long duration microseismic event 164
6.2 General Contributions 165
6.3 Future Work 167

Patent Application 169
References 170

APPENDIX 1 - Lamb Waves.....189
APPENDIX 2 - Lamb Frequency Equations for a Free Plate.....191
APPENDIX 3 - Dispersion Code.....192
APPENDIX 4 - Processing to isolate the line spectra.....192
APPENDIX 5 - Derivation of the acoustic transfer matrix 193
APPENDIX 6 - Borehole Finite Element Model.....197

List of Tables

Table 2.1–Wellbore parameters used to compute representative dispersion curves.....28

Table 3.1 – Parameters for the first 7 of 23 pipe sections used to Produce Figure 3.2……..……...…….…..56

Table 3.2 - Recording parameters for the two downhole assemblies manufactured by Avalon Sciences Ltd.....59

List of Figures

Figure 1.1 - A 0.3 s record from a hydraulic fracture monitoring (HFM) recording showing interpreted P- and S-waves shown by tick marks on most traces. Hodograms shown in the lower panel are two-component crossplots for the S-wave energy recorded on the traces at 1071 m depth. These body wave arrivals are interpreted signal.....4

Figure 1.2 – An average of the number of articles published by year by the SEG with the word microseismic in the search query. Since the year 2000, there has been a marked increase in published microseismic research.....5

Figure 1.3 – Map showing unconventional gas reservoirs in North America (CNEB, 2009). The microseismic data used in this thesis came from three wells denoted by orange and black stars.....6

Figure 1.4 – The percentage of U.S. rigs drilling horizontal wells has continued to increase since 2003 (CAPP, 2012).....8

Figure 1.5 – The number of horizontal wells drilled by year in Alberta, Saskatchewan and Manitoba has continued to increase, especially since 2006 (CAPP, 2012).....8

Figure 1.6 – Canadian production from hydraulically fractured horizontal wells (CAPP, 2012).....10

Figure 1.7 – Cross section of a wellbore with a clamped sonde. There are many waves that can be generated and propagated along the casing, cement, and cable or reflected by casing centralizers.....18

Figure 2.1 - Particle motion for Lamb waves in a cylinder for fundamental longitudinal, torsional and flexural modes, respectively. In cylinders, the Lamb wave motion is dominated by fundamental longitudinal L(0, 1) or torsional T(0, 1) modes (Long et al., 2003)…….……...…..25

Figure 2.2 - Dispersion curves for a tube wave and longitudinal Lamb waves calculated using the values in Table 2.1 with software from Karpfinger (2009). All longitudinal Lamb wave modes are dispersive. At a frequency of ~ 45 Hz, the velocity of the *L(0,1)* longitudinal mode is predicted to be ~ 5100 m/s. The D.C. estimate (marked by the red dot) is from Burago et al. (1980).....26

Figure 2.3 - Cross section through a wellbore. There may be fluid within the steel casing (black) cemented to the outermost strata. Each layer is characterized by its compressional and shear velocity, and bulk density…….....……..27

Figure 2.4 – An interpreted Lamb wave from dataset 1. The data are plotted after a 5/10-180/220 Hz. bandpass filter. The data have been rotated on the H-1 and H-2 components using vibroseis sweeps to orient the horizontal geophones. An S-wave arrival consistent with other S-wave arrivals at position 1 is recorded on the horizontal channels. At position 2, the upgoing reflection travelling 5100 m/s is modeled to be an L(0,1) longitudinal Lamb wave…..29

Figure 2.5 – One P-wave arrival (event 2) and two S-wave arrivals (events 1 and 3) from the first dataset……30

Figure 2.6 – Z-component frequency spectra for the upgoing wave at position 2 in Figure 2.4. The deepest traces are at the top and have the highest frequency content……..…30

Figure 2.7 – Plot of the centre frequencies from Figure 2.5. There is a 40 Hz drop in the peak frequencies over 210 m…….……....31

Figure 2.8 – Z-component vespagram for the upgoing waves in Figure 2.4. The Lamb waves have a V_{APP} ~ 5100 m/s…….……31

Figure 2.9 – Hodograms crossplotting trace amplitudes for the upgoing wave recorded at the -1390 m depth position from Figure 2.4. Most of the energy aligns with the Z-component…….……..32

Figure 2.10 – Plot of the upgoing trace energy from Figure 2.4…….…….33

Figure 2.11 - A Lamb wave event from microseismic dataset 2. The data are plotted after a 5/10-280/320 Hz bandpass filter. Energy with an apparent velocity of almost 7000 m/s at time position "1" is followed by another signal at time position "2". Positions "3"and "4" denote signal on the H-1 component and the Z-component……..….....……34

Figure 2.12– Z-component frequency spectra for the upgoing wave at position 2 in Figure 2.4. The deepest traces are at the top and have the highest frequency content…….35

Figure 2.13– Z-component frequency spectra for the upgoing wave at position 2 in Figure 2.11. The deepest traces are at the top and have the highest frequency content…….35

Figure 2.14 – Plot of the centre frequencies from Figure 2.13. There is a 40 Hz drop in the peak frequencies over 210 m……36

Figure 2.15 - Two "vespagram" (velocity spectral analyses) showing the linear apparent velocities for the upward travelling waves on the Z- and H-1

components in Figure 2.6. Numbers correspond to those used in Figure 2.6. The red areas show higher coherence in the vespagram ……38

Figure 2.16 – Hodogram crossplots from level 6 (1102 m depth) for the P-wave arrival (top left) for time position "4" in Figure 2.6. The pink line indicates the principal eigenvector from the covariance matrix (Kanasewich, 1981). The wave arrival has most of the energy on the Z-component……..…39

Figure 2.17 – Plot of the upgoing trace energy from Figure 2.4…….……..39

Figure 2.18 – Rate of occurrence (in 6 minute blocks) for 96 Lamb waves in survey #1 compared to the 700 P and/or S-waves……..……..….....……40

Figure 2.19 - Sonic and bulk density borehole logs and computed impedance from the monitoring well for dataset 1. The reservoir shale is highlighted in yellow. A carbonate layer with higher velocity underlies the targeted zone. Shear velocity logs were not recorded in the wellbore. The geophones are installed in a layer of little velocity or density contrast…….42

Figure 2.20 – Model for excitation of Lamb waves at the bottom of a wellbore. The P-wave impinges on the wellbore first and initiates a torsional wave. Subsequently, the S-wave impinges and initiates a longitudinal wave…...…43

Figure 2.21 - Longitudinal Lamb waves modeled using the values in Table 2.1. The upper (blue) curve is from a competent casing cement model; the lower (red) curve is from cement with reduced shear strength…….....….....44

Figure 3.1 – Schematic illustration of a steel cylinder with thin discs acting as acoustic impedance contrasts along the inside of the pipe. To calculate the acoustic displacement amplitudes at x=L, equation (3.1) would be implemented 7 times using the values in Table 3.1 The model for Figures 3.2 and 3.3 had 11 restrictions spaced 12.37 m apart for a total of 23 acoustic impedance contrasts along the pipe.....56

Figure 3.2 –Results from COMSOL finite-element modeling (dots) end Equation 3.2 (identical dots) compared to the acoustic transfer matrix (lines), based on an 11-segement model described by Figure 3.1 and Table 3.1.....57

Figure 3.3 – Fine structure of the comb spectra predicted by equation (3.3), showing that the passbands have a finite width and the higher frequency passbands scale at 5/4, 6/4, 7/4 ... of the lowest frequency in the comb-spectrum. Here, V=5780 m/s, L = 12.37 m, W = 0.001 m for the red passbands and W = 0.02 m for the blue passbands. Note the change in W adjusts both the transmitted frequencies and the width of the passbands.....58

Figure 3.4 – A perspective view of the recording geometry for dataset 1. The observation well is about 800 m southwest of the horizontal well. The treatment stages are shown by different colours.....60

Figure 3.5 - A 2 s seismic data plot (upper) and the first 0.1 s from this plot (lower) from the first dataset. Geophone levels for the first 5 traces starting at 2918 m depth appear to have random noise on all three of their components…..….. 62

Figure 3.6 – The frequency-amplitude spectrum for the 2918 m depth N-component trace from Figure 3.6. The lowest-frequency in the comb-spectrum (under the first red dot) occurs at 375 Hz. The two other red dots overlie the double and triple harmonics. The small green dots are equidistant between the simple harmonics. A model using the acoustic transfer matrix predicts all of the comb-spectrum frequencies……. 63

Figure 3.7 – The autocorrelation of trace 1 from Figure 3.5 showing only the positive lags. The decrease in the amplitude is the result of the short (0.3 s) autocorrelation window. The autocorrelation is not the result of random noise……64

Figure 3.8 – The temporal variation for first frequency in the comb-spectrum for stage 3 from dataset 1, as indicated by the red line. Equation (3.2) would predict the initial frequency of 375 Hz using a steel velocity of 5625 m/s, as the geophones are 15 m apart in the borehole. Also, plotted is the downhole pressure from the injection well (blue line). The fracture treatment was initiated at 19:48 hours on this plot……..……...65

Figure 3.9 – A perspective view of the central Alberta horizontal treatment well and vertical observation well. The observation well is only 50 m away from the horizontal well. Each of the 14 stages is a different colour.....66

Figure 3.10 - A 2 s seismic data plot (upper) and the first 0.1 s from this plot (lower) from the second dataset. The data sampling rate is 0.25 ms. There is a repeated time aligned event recorded on a number of traces, as indicated by the arrows…….....68

Figure 3.11 – The frequency amplitude spectrum from the first few minutes of the second dataset. The lowest frequency in the comb-spectrum under the first red dot occurs at 468 Hz. The green dots are equidistant between the red dots and ¼ incremental multiples of 468 Hz. All highlighted frequencies are predicted by the acoustic transfer matrix. The noise floor is at about 0.001.69

Figure 3.12 – The frequency amplitude spectrum for the lowest frequency in the comb-spectrum for 25 of 33 geophones from the second dataset. The 8 datasets not plotted were noisier. Each trace is offset 0.5 Hz from the

shallowest geophone at the top. Note the consistency in the data measurement.....70

Figure 3.13 – The detected fundamental vibration frequency for the Alberta hydraulic fracture monitoring program. Equation (3.2) would predict the initial frequency of 467 Hz with a corresponding steel velocity of 5780 m/s, as the geophones are 12.37 m apart in the borehole. Figure 3.3 is representative of the line spectra except the areas with the horizontal bars which are represented by Figure 3.10…….70

Figure 3.14 – Histogram of the differences between the individual detected frequency values in Figure 3.12 and the median of those values (Figure 3.13) for 25 of 33 geophones from the second dataset. The bottom plot is a 600X zoom of the top plot for histogram values between 0 and 5. There is consistency in the data measurement; only ~ 330 values out of ~ 200,000 deviated greater than 0.35 Hz from the median. The data values were detected in 2 s non-overlapping trace increments and were binned in 0.15 Hz intervals..... 71

Figure 3.15 – The frequency amplitude spectrum for the times indicated by the red lines in Figure 3.13. During this time, line spectra occur between the comb spectra in Figure 3.11.....72

Figure 3.16 – The temporal variation for the first frequency in the comb spectrum for dataset 2 (red curve). Equation (3.2) predicts a fundamental frequency of 467 Hz based on a steel velocity of 5780 m/s and geophone separation of 12.37. The surface treatment pressure for the 10 monitored stages is plotted in blue. The local pressure increases prior to breakdown are shown as thicker black lines…….…..73

Figure 3.17 - Crossplots showing a high cross-correlation for the five detected fundamental frequencies versus the first resonance in the comb. Before the crossplots, a 5 point median filter was applied to all datasets. There are about 16,000 values in each crossplot. The steps in the plots are caused by the frequency steps in the FFT.....74

..

Figure 3.18 – A larger plot of the 10/4 versus the fundamental vibration crossplot from Figure 3.12.....75

Figure 3.19 - Five amplitude ratios for the 4/4, 8/4, 12/4, 13/4 and 14/4 overtones compared to the 10/4 overtone. All of the amplitude ratios are consistent in amplitude except for the area denoted in red on Figure 3.13, where the frequency amplitude spectrum changed from Figure 3.11 to Figure 3.15.....76

Figure 3.20 – An expanded view of the 12/4 and the 10/4 Hz amplitude ratio from Figure 3.19.....77

Figure 3.21 – The comb-frequency for the 8/4 frequency at early middle and late times during the hydraulic fracture treatment. Within the limits of the Fourier transform, there is fine detail in the comb frequency. Also, the individual comb-spectrum frequencies occur over a defined bandwidth. The frequency variations are similar to a variable length Helmholtz resonator (see Selamet et al., 1995 or Mason, 1927).....77

Figure 3.22 – Conceptual model relating geophone-clamping mechanism to changes in external pressure. When stress changes impinge on the observation wellbore as indicated by the arrow, the geophone clamp spring reacts, changing the effective length (W) of stress concentration associated with borehole-geophone clamp interface……..……..79

Figure 3.23 –Pump jack vibration from a nearby surface pump jack. These data were recorded with a geophone placed on the pumpjack cement base. The vibration begins at 7.75 Hz and continues in almost integer multiples up to 99 Hz. These frequencies are lower than the acoustic transmissivity frequencies……..80

Figure 3.24 –A frequency amplitude plot of a spurious frequency in a geophone response curve (from Faber and Maxwell, 1997)……..…….81

Figure 3.25 – A photograph of the 1.8 m long copper pipe that was suspended by a rope and pressurized with air to pressures up to 827 kPa…….…..83

Figure 3.26 – Frequency amplitude plots for two local peaks at seven pipe pressures using the pipe shown in Figure 3.17. As the pressure decreased, the resonant frequency of the pipe decreased……..84

Figure 3.27 – A crossplot of the first local peak in Figure 3.18 versus pressure. As the pressure decreased, the resonant frequency of the pipe decreased……...84

Figure 3.28 – A plot showing the steel pipe movement for one of the COMSOL calculated eigenfrequencies…….…….. 85

Figure 3.29 - As the external pressure on the pipe in Figure 3.20 was increased, the COMSOL calculated resonant vibration of the pipe was reduced.....86

Figure 3.30a and b – Crossplot of the vibration frequencies vs. the treatment well downhole pressure from Figure 3.6 between 17:00 and 19:48 hours for dataset 1. The least squares best fit line has a coefficient of determination given by $R^2 = 0.83$. The implied change in clamping width ΔW from (3.2) as a function of the lowest comb-spectrum frequency is shown below…….….88

Figure 3.31 a and b – Crossplot of the vibration frequencies vs. the treatment well downhole pressures indicated in black on Figure 3.11. The least squares best

fit line in red has a coefficient of determination given by R^2 = 0.71. The implied change in clamping width ΔW from (3.2) as a function of the lowest comb-spectrum frequency is shown below…….……89

Figure 4.1 – A simple cross-section through layered media showing a subsurface source that generates a wavefield that is sampled by a borehole geophone. The layers can be described by their elastic properties.....96

Figure 4.2 – A number of possible path effects for microseismic data recorded by a geophone at depth. Multiply reflected energy, attenuation, mode converted energy, ghosting and head waves call change the character of the source wavelet.....97

Figure 4.3 – A plan view of the central Alberta horizontal treatment well and vertical observation monitor well. The observation well is 50 m north of the horizontal well. All wells displayed have produced hydrocarbons from a Cretaceous zone at about 1300 m depth.....101

Figure 4.4 – A perspective view of the central Alberta horizontal treatment well and vertical observation well. All values are in meters. The observation well is only 50 m away from the horizontal well. The 14 hydraulic fracture stages are shown in colour…….....…102

Figure 4.5 – Event 3 from the microseismic survey. The data for the horizontal channels were rotated using a vibroseis checkshot survey. A 10 to 800 Hz bandpass filter was applied to the data. The P- and S-wave arrivals are evident on most traces. The lack of consistent energy across the N and E horizontal components may be caused by poor geophone coupling or poor azimuth resolution…….……..…..…104

Figure 4.6 –Cross correlations for each trace from events 9 and 10. The high cross correlation resulted in the two events being attached to group C as shown in Figures 4.7 and 4.8……105

Figure 4.7 – Cross correlation amplitude matrix for the 20 events. The four clustered event groups are also shown. Some correlation coefficients are skewed by high amplitude signal signals and noise, such as the cross correlations for events 1 and 2. This matrix was refined by inspecting the entire set of cross correlations…….……....106

Figure 4.8 – Time vs. fracture distance cross-plot for 17 events from the microseismic survey. The events were grouped into four clusters lettered A to D based upon cross correlations between all event pairs. Three of the events were not used as part of the clusters.....106

Figure 4.9 – A close up of the vertical-component traces for the P-wave recorded on event 3 (left) and 4 (right). The P-wave arrivals for event 4 contain

perceptibly higher signal frequency content that can be seen in the narrower peaks and trailing troughs on the trace data.....107

Figure 4.10 – Frequency-amplitude spectra for the deepest vertical geophone for event 3 and 4. Above 250 Hz, event 3 recorded consistently higher signal. The signal increase between 270 and 330 Hz and 440 to 540 Hz was observed on a number of the events. Also shown is the noise spectrum estimated using the preceding 0.1 s window before P – wave energy onset…….…….....108

Figure 4.11 – Frequency-amplitude spectra for the vertical geophone 80 m above the reservoir zone for the four P-wave arrivals in group D on Figure 4.8. Three events have similar amplitudes at about 100 Hz and a similar shape thereafter. However, event 3 (dot-dashed blue line) has an overall lower frequency spectrum above 150 Hz……..…..…….109

Figure 4.12 – Frequency-amplitude spectra for the vertical geophone 6 m in the reservoir zone for the four P-wave arrivals in group D on Figure 4.8. The events have similar amplitudes. However, three of the events have higher frequency amplitude spectra between 280 and 320 Hz, and one event has an elevated spectrum between 440 and 540 Hz……..……..…….110

Figure 4.13 – P- and S-wave velocity log (left) and bulk-density log (right) from the monitor well, located 50 m north of the 1000 m horizontal treatment wellbore.....111

Figure 4.14 – P-wave velocity for the model constructed using the P-wave, S-wave and density profiles in Figure 4.13. Mode conversions were modelled, and the sources and receivers were placed to minimize model edge effects. A minimum-phase Ricker wavelet with a dominant frequency of 300 Hz was used.....112

Figure 4.15 – The P – wave energy from the 300 m modeled source.....113

Figure 4.16 – Frequency-amplitude spectra for a vertical geophone at 300 m depth for shots at 290 m (red dashed line) and 300 m (blue) depth in the finite difference model. Both sources and receivers were in the reservoir zone. The modeled events show differences in high-frequency character (gray shaded area) that resemble the events shown in Figure 4.8.....114

Figure 4.17 – Modeled frequency-amplitude spectra for the vertical-component wave field at 290 m depth (within the target zone) for sources located at three depths across the reservoir. About half of the 20 recorded events had spectral peaks similar to the 300 to 350 Hz peak for the 310 m depth.....114

Figure 4.18 – The P-wave velocities for a simple model to test some path effect hypotheses. The low velocity layer is 20 m thick.....118

Figure 4.19 – The vertical channel recording for a 300 Hz minimum-phase Ricker wavelet source at 120 m depth, 20 m above the low velocity zone. There is no attenuation in the model; all variations in the measured wavelet can be attributed to path effects.....119

Figure 4.20 – The frequency amplitude spectra for the receiver traces shown in Figure 4.19.....120

Figure 4.21 – Cross correlations for the traces in Figure 4.19 with the 100 m depth receiver (the 100 m level is an autocorrelation). There is little change in the cross correlation above the zone and a phase change below the zone. For the traces at 140 and 150 the correlations show energy lagged at two different times.....120

Figure 4.22 – Thin-bed reflectivity can introduce notches in frequency spectra (from Partyka et al., 1999).....121

Figure 4.23 – The vertical channel recording for a 300 Hz minimum-phase Ricker wavelet source at 160 m depth. The traces from 140 to 180 m recorded anomalous path effects. The first event at 180m could be a direct arrival.....122

Figure 4.24 – The frequency amplitude spectra for the receiver traces shown in Figure 4.23.....123

Figure 4.25 – The vertical channel P-wave recording for the second dataset. Note the 'ringy' energy recorded at the bottom two geophones. Both of these geophones were clamped within the reservoir zone. The minimum arrival time near the bottom of the array may locate the source within the reservoir.....123

Figure 4.26 – The spectra for the shallowest trace (1040 m) and the second from deepest trace (1165m) from Figure 4.25. The short time window gives the FFT a `blocky` appearance.....124

Figure 4.27 – The sampled energy at the base of the low velocity zone (160 m) for eight difference source depths using the model shown in Figure 4.22.....124

Figure 4.28 – Frequency spectra for the horizontal component traces in Figure 4.27 from 0.0 to 0.08 s. Note the spectral notches at the 150 m depth.....125

Figure 4.29 – A simple wedge model thickening a low velocity layer from three to 31 m.....126

Figure 4.30 – The vertical component sampling for the wedge model shown in Figure 4.29.....126

Figure 4.31 – Frequency spectra for the traces in Figure 4.30. Note the spectral notches at 19 and 21 m thickness.....127

Figure 4.32 – Computed 280 to 320 Hz vs. 50 to 150 Hz. amplitude ratios for the 20 events. The two deepest geophones, within the reservoir, have the highest ratios. The shallowest geophone is contaminated with high frequency noise. The low ratio at the -420 m geophone depth may be receiver path effects.....129

Figure 4.33 – Computed 280 to 320 Hz vs. 50 to 150 Hz. amplitude ratios for the six finite difference calculations. The reservoir zone is between the two red lines. Geophones at These ratios should be free of source and receiver path effects.....129

Figure 4.34 – Computed 440 to 540 Hz vs. 50 to 150 Hz. amplitude ratios for 19 of the 20 events. There are some patterns in the display, such as the high ratios at the two deepest geophones. The geophones at -408 and -420 m recorded consistently low ratio values. These could be receiver coupling effects, similar to site effects in earthquake seismology.....130

Figure 4.35 – The average frequency band ratio from Figure 4.34 averaged as a function of depth. The two deepest geophones have the highest amount of energy ratio. This could be lower dispersion in the lower velocity layer.....131

Figure 4.36 – Computed 440 to 540 Hz vs. 50 to 150 Hz. amplitude ratios for the six finite difference calculations. The reservoir zone is between the two red lines. These ratios should be free of source and receiver path effects.....132

Figure 5.1 – Pembina area Cardium pool outline (adopted from Fic et al., 2011). The hydraulic fracture treatment well discussed here is within the study area shown.....137

Figure 5.2 – Pembina area Cardium pool horizontal well licenses, by year. There has been a dramatic increase in horizontal drilling, beginning in 2009. Most of these wells were stimulated by hydraulic fracturing (NEB, 2011).....138

Figure 5.3 – Pembina area Cardium production (source: Accumap, accessed June 1, 2013), showing a dramatic increase in production since 2009 (see Figure 5.2).....138

Figure 5.4 – A plot showing the horizontal wellbore and the offset vertical monitor wellbore. The hydraulic fracture stages are shown in colour. The thicker green coloured stage is the 6th stage, as discussed below…….141

Figure 5.5 – A spectrogram for the 10th vertical component trace (1152 m depth) from the dataset along with the 10th vertical trace. The 60 Hz maximum signal at the onset of the event gradually decreases to about 30 Hz near the end of the event.....143

Figure 5.6 – A 20 s record (starting at 10 s with respect to Figure 5.5) showing an LPLD event recorded on all channels. About 90 individual events can be discerned.....143

Figure 5.7 – A trace-normalized three second recording from Figure 5.1. The data were rotated to north and east orientations and have been bandpass filtered with a 5-100 Hz filter. The coherent energy is strongest on the Z component, except for the arrival at ~ 10.3 s.....144

Figure 5.8 – A 300 ms window for the Z-component traces showing 5 events. The events appear similar in phase and frequency content. Compared to the red lines (V = 3790 m/s), there are subtle differences in the apparent velocity. This is consistent with Das and Zoback (2012)……..…..……145

Figure 5.9 – A velocity spectrum ("vespagram") for the traces shown in Figure 5.8. Events 3 and 4 appear to have a similar linear moveout in Figure 5.8, but the vespagram shows a higher absolute velocity for event 4.....145

Figure 5.10 – Hodogram crossplots for the event at 10.8 s in Figure 5.7. A large portion of the energy is on the vertical channels……...…146

Figure 5.11 – Spectrum from one Z-component trace at 1164 m depth for the LPLD, the microseismic event in Figure 5.12 (vertical channel at 1165 m depth) and background noise. The LPLD event has comparatively very low frequency……..…….147

Figure 5.12 – Representative high-frequency event from the microseismic survey. A 10 to 800 Hz bandpass filter was applied to the data. The well-define P- and S-wave energy do not resemble the event in Figure 5.5……..…….……...147

Figure 5.13 – The apparent velocity calculated for 28 events in the 20 s anomaly using the Z-channel data. The minimum VAPP ~ 3240 m/s, the maximum VAPP ~ 4890 m/s and the median VAPP ~ 3790 m/s. The line slopes are equivalent to the apparent velocity……..……148

Figure 5.14 – Comparison between a 3.5 Mw magnitude earthquake recorded at RDEA station on June 3, 2013 at 9:14 AM and the LPLD event (the trace amplitude a representative vertical trace (depth 1152 m) from Figure 5.6……..……..…….150

Figure 5.15 - The 3.5 Mw magnitude earthquake plotted on Figure 5.14 was recorded at RDEA station on June 3, 2013 and located at 52.443° -116.431° as shown…….150

Figure 5.16 – A plot of the surface pressure for 12 stages of the hydraulic fracture treatment. The estimated well head treating pressures to achieve breakdown is shown in blue; fractures were not initiated in the last 4 stages……..151

Figure 5.17 – A plot of the surface pressure for 12 stages of the hydraulic fracture treatment with the detected microseismic events. The potential LPLD event occurred at the bleed-off period of the sixth hydraulic stage (the first stage was not pressurized)……..152

Figure 5.18 – A plan view of the contractor's located events detected using monitor well 'A'. Stage 4 had located events in the green shaded and open green circles (highlighted for effect only, not event magnitude). Stage 5 events were located close to most fracture stage 6 events, as shown on the bottom view. The red North 45° East striking fault is interpreted by contractor……...153

Figure 5.19 - A plan view of the contractor's located events for stage 6 overlain with the calculated emergent angles from Figure 5.11…….154

Figure 5.20 - A plan view of the contractor's located events a Cardium hydraulic fracture treatment (from Duhault, 2012)…….155

Figure 5.21 – The North America portion of the world stress map showing the North 45° East principal stress direction for Alberta (from Heidbach et al., 2008)…….156

Figure A-1 – Free plate schematic showing geometry for internally reflected body waves (from Davies, 2008). The plate has a thickness h and traction-free surfaces.....189

Figure A-2 – Wavenumber graphical representation of the free plate dispersion relation for coupled SV and P partial waves (from Davies, 2008). Here k represents wavenumber, ω represents angular velocity and V represents velocity. The axial components of k_s and k_l are required to be the same.....190

Figure A-3 – a schematic representation of a cut away cylinder where plane waves can travel either left to right (p+) or right to left (p-). The cylinder has diameters defined by radii r_i and r_o (inner and outer, respectively).....193

Epigraph

In dealing with a scientific problem, I first arrange several experiments, since my purpose is to determine the problem in accordance with experience, and then to show why the bodies are compelled so to act.

Leonardo Da Vinci (1452-1519)

Chapter One: Introduction

1.1 Introduction

This thesis examines passive seismic data recorded in deep vertical boreholes acquired during the monitoring of hydraulic fracture treatments. The data were collected by sondes clamped to the sides of steel casing cemented to geologic strata. The purpose of the data collection was to record body wave energy emanating from induced seismicity caused by the hydraulic fracturing in offsetting horizontal wells. Hydraulic fracturing is the process of introducing fluids at high pressure to a reservoir zone with the intent to create cracks in the zone to increase the reservoir permeability. This increased permeability is expected to improve the hydrocarbon productivity, improving the economics of drilling the wellbore (Holditch, 2006).

The hydraulic fracturing process changes the stress or volume within the targeted rock mass. The physical response of the rock is to redistribute the stress by shearing, creating a fracture, or slipping along existing fractures (Schmitt et al., 2012). A by-product of this shearing or slipping is the creation of body waves, namely P- and S-wave energy that will emanate outward from the fracture position (Warpinski, 2009). This process represents induced seismicity from hydraulic fracturing.

The use of continuous geophone records to detect seismicity induced by hydraulic fracturing is colloquially known as microseismic monitoring. If the P- and S-wave energy can be discerned on the collected data, their arrival time and direction of arrival can be used to locate the source position. The events usually have lower magnitude

(moment magnitude less than 0) P– and S–wave arrivals, hence the name "microseismic data" (Maxwell et al., 2010).

Microseismic data can also be used for the passive monitoring of areas of interest to try to detect geohazards such as fluid movement along a fault (Rutledge et al., 2004). Ground motion sensors (e.g. geophones) can be placed at the ground surface or down a deep wellbore. Geophones deployed in an array can be used to locate P- and S-wave energy using various location algorithms. Based on recorded waveforms, characteristics such as magnitude, arrival times, and direction of arrival are determined. For most microseismic data analyses, this is the extent of single event interpretations recorded at a single wellbore (Maxwell et al., 2010). A collection of source positions can be used to produce a map that can be interpreted as a hydraulically-induced fracture network (Mayerhofer, 2010). The geometrical patterns in this map can be used to estimate the efficacy of the hydraulic fracture stimulation in terms of increased reservoir flow paths (and hence permeability) between the reservoir and the draining borehole.

The collection of microseismic data results in the recording of both signal and noise. Signal is defined here as seismic energy that can be used to provide information about the subsurface. Interpreted signal is that part of the signal that is analyzed to make inferences about the subsurface properties. Uninterpreted signal is either recognized as signal and not analyzed, or it is unrecognized as signal. Noise can be broken down into coherent and random noise. Generally, coherent noise can be predicted temporally or spatially, while random noise cannot. This thesis focuses on the analysis of uninterpreted signals and coherent noise recorded by microseismic arrays in vertical wellbores.

An example of an interpreted signal is shown in Figure 1.1. In this example, 12 three-component geophones clamped in a borehole at depths of about 1100 m recorded P- and S-wave energy on all of the trace data. The energy onset for the P-wave and S-wave events is shown (as determined by an Akaike Information Criterion algorithm, St-Onge, 2011). Using these traveltimes, the distance to the source of the event can be determined based on a velocity model for the acquisition area. The hodograms shown in Figure 1.1 are amplitude crossplots for one trace of S-wave energy for the event. P-wave hodograms, or in some cases S-wave hodograms, can be used to estimate the azimuth for the arrival. For a geophone array deployed in a single monitor wellbore, the distance and the azimuth are both required to determine the source location (hypocentre). Most contractors providing microseismic data interpretations follow this (or a similar) geolocation procedure for data interpretation from data collected in single wellbores.

The analysis of uninterpreted signal forms parts of this thesis. Generally uninterpreted changes in frequency amplitude spectra of P– and S–wave signals are analyzed here and modelled to add to the interpretation of P– and S–wave energy as it is used in geolocation algorithms. These frequency-dependent amplitude changes are interpreted to be caused by path effects as the waves travel through a medium.

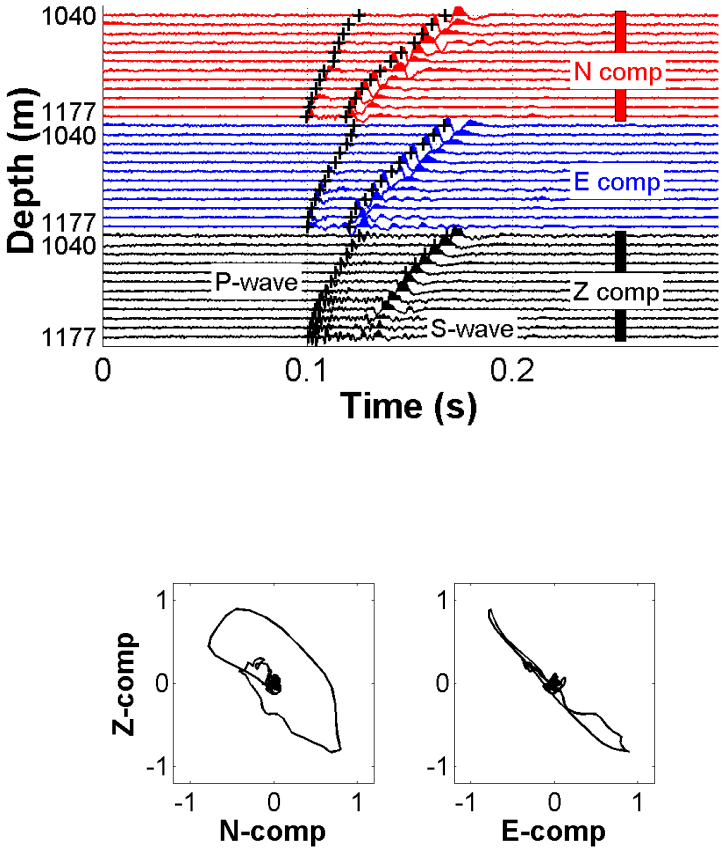

Figure 1.1 - A 0.3 s record from a hydraulic fracture monitoring (HFM) recording showing interpreted P- and S-waves shown by tick marks on most traces. Hodograms shown in the lower panel are two-component crossplots for the S-wave energy recorded on the traces at 1071 m depth. These body wave arrivals are interpreted signal.

Coherent noise recorded on microseismic data is defined here as any repeatedly recorded energy on two or more traces that is not a P- and/or S-wave arrival. Coherent noise on microseismic data is often persistent, repeatable, and may be caused by various types of waves travelling in the borehole (Schoenberg, 2001). A number of examples of

coherent noise such as Lamb waves and Stoneley waves are presented and analyzed in this thesis. It is hoped that the analysis will lead to a better understanding of the coherent noise to enable extraction of useful subsurface information - in effect, turning coherent noise into an alternative type of signal. The idea that uninterpreted signal and coherent noise can be analyzed as signal is one impetus for this thesis.

A second impetus for this thesis is the increased use of microseismic data to measure induced seismicity from the hydraulic fracturing of horizontal wells, as it has grown dramatically in recent years (Figure 1.2). This induced seismicity is unrelated to earth tremors, volcanoes or other naturally occurring processes. The recording, processing

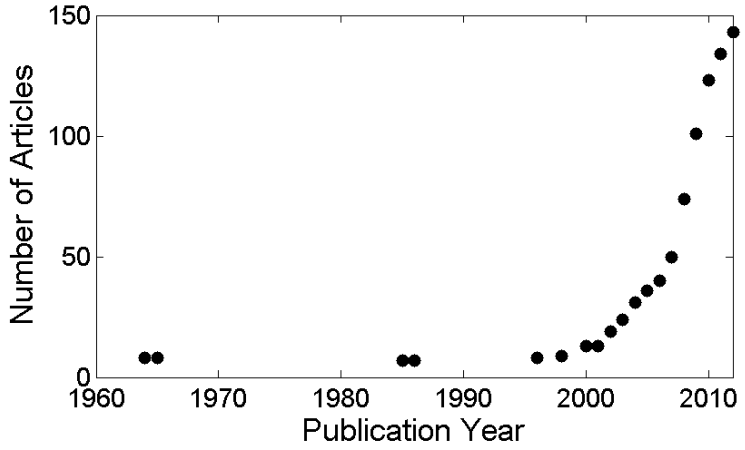

Figure 1.2 – An average of the number of articles published by year by the SEG with the word microseismic in the search query. Since the year 2000, there has been a marked increase in publications related to microseismic monitoring.

and interpretation of microseismic data for hydraulic fracture monitoring (HFM) are still in relatively early stages of development. A third impetus for this thesis is to try to

advance this science in light of the increased use of microseismic data collection, analysis and interpretation.

1.2 **Hydraulic fracturing**

There are large areas of North America that have low-permeability unconventional reservoirs, as shown in Figure 1.3. Generally, these reservoirs require unconventional methods

Figure 1.3 – Map showing unconventional gas reservoirs in North America (CNEB, 2009). The microseismic data used in this thesis are from three wells denoted by orange and black stars. A key aspect of economic production in these low permeability rocks is hydraulic fracture stimulation, usually in horizontal wells (Nobakht and Clarkson, 2013).

Hydraulic fracturing is defined as the process of using fluid or gas under pressure to create cracks or open existing cracks, usually in hydrocarbon bearing rocks (CSUR, 2013). The purpose is to increase reservoir permeability to increase production, making low productivity areas more economical to drill and produce. Since 2003 an increasing number of horizontal wells have been drilled, and an increasing number of those are completed by hydraulically fracturing the formation (CSUR, 2013). More drilling rigs in the U.S. are now drilling horizontal wells than vertical wells, as shown in Figure 1.4. Also, there has been a sharp rise in the drilling of horizontals wells in western Canada, as exemplified by the data shown Figure 1.5. Hydraulic fracturing of a formation can be accomplished by injecting water, oil, and/or chemicals into the subsurface at high pressures.

Drilling a horizontal well usually begins by drilling a vertical or near-vertical section to a predetermined depth. Then an angled drill bit is oriented to a compass direction and a mud motor is used to rotate the bit. The directionally oriented bit will drill the wellbore at a small angle to the vertical. Eventually the wellbore will become horizontal. Usually the well then is cased from surface casing to the start of the horizontal portion (intermediate casing) by cementing steel pipe within the borehole. The drill bit is then drilled through the reservoir for planned distances that can be 1600 m or greater.

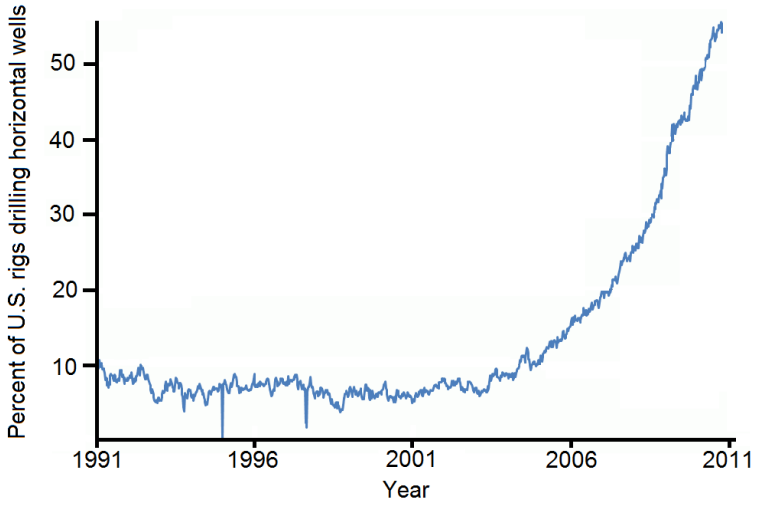

Figure 1.4 – The percentage of U.S. rigs drilling horizontal wells has continued to increase since 2003 (CAPP, 2012).

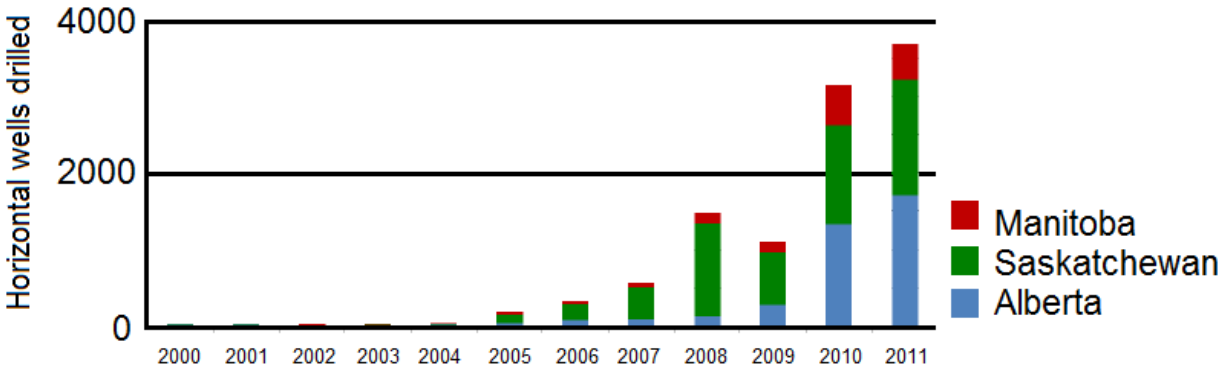

Figure 1.5 – The number of horizontal wells drilled by year in Alberta, Saskatchewan and Manitoba continues to increase, especially since 2006 (CAPP, 2012).

The well can remain open within the reservoir (open-hole completion), or it can have steel casing (cased-hole completion). Cased-hole hydraulic-fracture completions take longer to perform because they require that the casing be opened up to the reservoir

by detonating small charges to perforate holes in the steel casing. A well can be hydraulically fractured after it has been perforated (or in the case of an open-hole completion, any time after the drilling rig has moved off of the wellbore).

If the well is hydraulically stimulated, fractures are initiated by pressurizing the reservoir. Usually twice the formation pressure will initiate a fracture (Song et al., 2001), although the exact fracture pressure is typically ascertained after a number of hydraulic fracture treatments have been completed in an area (Valko and Economides, 1995). Once a fracture is initiated, fluids are continuously pumped at high pressures to continue fracture propagation. At some point, slurry that contains spherical sand or ceramic grains ("proppant") is pumped into the fracture. After the fracture treatment, the fluid is recovered and some of the proppant remains in the fractures to try to prevent complete closure. The purpose of the procedure is to create a set of connected fractures that will increase the reservoir permeability.

Horizontally drilling unconventional reservoirs can enhance the economic viability in a number of ways. Horizontal wells without hydraulic fracturing can have two to three times the amount of production than a vertical well in the same area (Butler, 1994). If fractured, these wells can have 2-3 times initial increased productivity (Butler, 1994). Relative to vertical wells, horizontal wells can drain larger areas and have a lower drawdown pressure, which can increase productivity and estimated ultimate recovery. Some jurisdictions such as the Province of Saskatchewan currently offer royalty holidays as an incentive to drill horizontal wells. All of this has resulted in increased horizontal drilling as can be seen in Figures 1.4, 1.5 and 1.6.

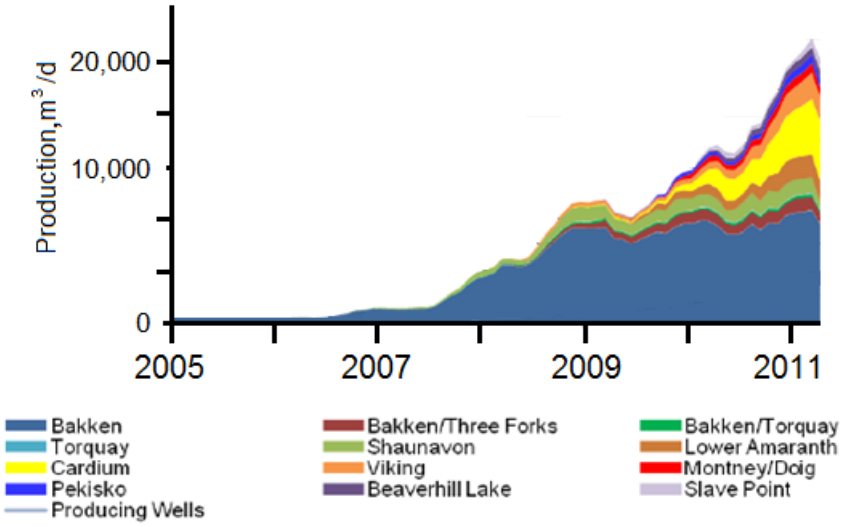

Figure 1.6 – Canadian production from hydraulically fractured horizontal wells (CAPP, 2012).

1.3 **History of downhole seismic recording**

The recording of seismic data in boreholes began about 80 years ago. One of the earliest references that geophones could be used in a borehole was by McCollum and LaRue (1931), who suggested the installation of geophones in a borehole to record surface sources. These early measurements were the start of velocity "checkshot" surveys. These surveys tie surface seismic data to formation structure tops in a borehole. Usually only the first break energy was utilized in early checkshot surveys.

Velocity checkshot surveys were the precursor to vertical seismic profiling (VSP), where a number of sources (or receivers) were placed in a borehole along with a number of receivers (or sources). VSP surveys were not widely used until the early 1980s (Hardage, 2001). VSP surveys can be processed to produce a nearly multiple-free

seismic trace to determine the phase of surface seismic using cross correlation. A logical extension of VSP data is to place source and receivers in boreholes. Crosswell profiling has been used since the early 1980s (Hardage, 2001) to map reservoir characteristics such as porosity zones.

A natural extension of crosswell or VSP data collection is the use of sondes in boreholes to listen for and record microseisms. The acquisition of borehole microseismic data may have begun with the use of borehole seismic to map enhanced oil recovery processes (Wayland and Lee, 1986). Some of the key advances after this included the U.S. Department of Energy M-site experiment from 1992 to 1996 to monitor six hydraulic fracture injections into fluvial sandstone using multi-level triaxial receivers in two wells to show images of hydraulic fracture geometries at depth (Warpinski et al., 1996). Rutledge and Phillips (2003) showed that manually repicking microseismic data from a hydraulic fracture treatment in Cotton Valley, East Texas resulted in increased location accuracy. Maxwell et al., (2000) discuss monitoring of the progression of a hydraulic fracture stimulation to provide a real time interpretation. During this time, there have been consistent improvements in the acquisition, processing and interpretation of microseismic data.

1.4 **Borehole and surface microseismic monitoring**

1.4.1 Acquisition

Currently, microseismic data are generally acquired at the surface with geophones at the ground surface or in shallow boreholes ranging from 20 to 180 m (Microseismic,

2013), or in deep boreholes that extend near the reservoir depth. Some surface microseismic monitoring is done with 1000 or more geophone stations (Abbott et al., 2007). Up to 50 geophones can be placed down a borehole. Some monitoring is permanently in place for "life of field" studies (see Forgues et al., 2011, or Lakings et al., 2006 or Chambers and Kendall, 2010); however, most monitoring is only for the duration of the hydraulic fracture treatment (Warpinski, 2009).

Surface and deep borehole methods each have advantages and disadvantages for microseismic acquisition. For example, Eisner et al. (2011) discuss the benefits of microseismic data acquired at the ground surface. Among the advantages is the ability to deploy a large number of sensors at the ground surface. Also, there is a much larger solid angle of acquisition than downhole data recorded at a limited number of boreholes. The larger solid angle can result in improved source position accuracy (Eaton and Forouhideh, 2011). Hydrocarbon production shut-in to deploy downhole sondes is avoided. Eisner et al. (2011) also note that the primary challenge in surface monitoring is reduced signal amplitude at the surface, coupled with increased noise levels. Therefore, the main challenge of surface microseismic monitoring is the detection of microseismic events at lower S/N than data recorded in a borehole.

Acquiring microseismic data in deep boreholes close to areas of hydraulic fracture stimulation has some advantages. The deeper borehole sondes can record significantly higher frequencies and S/N than surface sondes. The sondes are closer to the microseismic sources, resulting in less attenuation, spherical spreading and reflectivity losses, especially at higher frequencies. The sondes should be able to record smaller

magnitude P– and S-wave arrivals that might not be detected at the surface. However, there could be a problem obtaining observation boreholes available for microseismic monitoring. For example, a company that wishes to record microseismic data may not have an adjacent borehole available for use. Moreover, there are associated costs of pulling production tubing and other required work on existing boreholes.

For both surface and borehole microseismic data, it has been recognized that there is currently a lack of recording standards and formats for microseismic data. To address this deficiency, the chief geophysicists' forum of the Canadian Society of Exploration Geophysicists has published recommended standards for recording, processing and interpretation of microseismic data in Canada (Maxwell and Reynolds, 2012). It is not clear if these standards have been accepted or are widely used at the present time.

1.4.2 Processing and interpretation

When compared with multifold surface seismic data, there is relatively little signal processing applied to microseismic data that are processed for geolocation results (Maxwell et al., 2010). The azimuthal orientations of downhole horizontal component geophones are usually determined with check-shot surveys. Here, surface sources at known locations are used to excite body waves recorded by the downhole geophone array. These data are used to orient the horizontal signals into compass north and east directions. This can be done using hodograms or principal component analysis (Bale et al., 2012). Sometimes a DC removal filter is applied to the data (St-Onge and Eaton, 2011). Usually, deconvolution is not applied to the data. Recently, methods have been

developed for migration of continuous microseismic data to help determine source locations (Warpinski, 2009).

The basic processing flow for microseismic interpretation is as follows. A representative velocity model is constructed using well log or other data. The velocities are extended or interpolated into a 3-D volume velocity model (Fu and Luo, 2009). The microseismic data are recorded, and automatic algorithms detect P– and S-wave arrivals in the data (Akram and Eaton, 2012). The velocity model is used to calculate source locations based upon the travel time differences in the body wave energy. The velocity cube may then be updated if required (Akram and Eaton, 2013). An update may be warranted if a linear least squares difference between the observed and calculated arrivals is minimized with the update. A hodogram analysis can be done to find the direction of arrival for the wave (Wong et al., 2010). Finally, the locations are graphically compared to other calculated locations (Mostafa et al., 2012). These can be effectively visualized as a "movie" of calculated events as a function of time. Most companies that process and interpret microseismic data appear to keep their algorithms confidential as a competitive advantage.

Indeed, "it is important for practitioners to make all facets of microseismic technology more transparent to the end user" (Warpinski, 2009). To this end, there are a number of recent advances in microseismic data processing and interpretation. Farghal and Levin (2012) discuss an algorithm to group microseismic events from the same area to improve upon their position calculation. These "multiplets" are determined by cross-correlation, and their relative distribution is improved. Das and Zoback (2011) have

identified long-period long-duration microseismic events that may be originating from movement along pre-existing fault zones. Identification of these events could have ramifications for the long-term monitoring of hydraulic fracture treatments. Finally, Zimmer (2011) presents a quantitative interpretation of shear-wave splitting to determine fracture geometry and density. All of these exemplify potential new applications currently under development that could improve current microseismic interpretation and application beyond its' current use.

1.4.3 Summary

The future growth of microseismic monitoring of hydraulic fractures treatments at the surface or down boreholes will be determined largely by the oil and gas production companies that employ the technology. A review of recent reports from production companies presents limitations to microseismic monitoring that have to be addressed. Johnston and Shrallow (2011) and Seibel et al. (2010) discuss ambiguity in downhole microseismic monitoring, the non-uniqueness of fracture location and the bias in results towards the observation well. Hayles et al. (2011) present a surprisingly large distribution of microseismic event locations from three different contractors. They conclude: "many of the lessons learned by seismologists have not crossed the chasm between the geophysical and engineering realms and microseismic processing remains in its infancy." Finally, Li et al. (2012) present interpretations from four microseismic providers with widely different solutions, and note "to our dismay, there was very little agreement in the results from the four companies."

1.5 **Signal and noise**

Seismic signal is defined here as a wave that can provide information about the subsurface. Usually the signal is P- and/or S-wave energy that has travelled from a microseismic source. Seismic noise is defined here as energy recorded by sensors that provide no information about subsurface geology. Seismic noise can be divided into coherent and random noise (see Yilmaz, 2001; Todorov and Margrave, 2010). Coherent noise usually results from real phenomena that are generating energy recorded by a geophone array. Examples of coherent noise at the surface are ground roll or multiple reflections. In a borehole, coherent noise may include energy trapped in the casing/casing cement/interface boundary, such as Stoneley waves. Coherent noise can be defined by apparent velocity across the spread, average frequency content and dispersion.

Random noise is not correlated from trace to trace. Examples of random noise at the surface are wind noise or instrument noise. In a borehole, random noise may be caused by ambient noise in the Earth. Random noise can usually be defined as a time-stationary process with no cross-correlation. Random noise is not specifically analyzed in this thesis.

An estimate of the relative level of a signal imbedded in random noise can be accomplished by estimating a signal-to-noise (S/N) ratio. In this thesis, signal-to-noise ratio is defined by (1.1):

$$S/N = P_{t1}/P_{t2} = \text{RMS}\,[(A_{t1}/A_{t2})^2] \qquad (1.1)$$

Where P = trace power which is equivalent to the sum of the squares of A, the raw trace amplitudes between t_1 and t_2. For this thesis, t_1 = 0 to 0.1 s after P- or S-wave energy onset and t_2 = 0 to 0.1 s before P- or S-wave energy onset.

1.6 **Signal and noise recorded on borehole microseismic data**

Other than P– and S–wave arrivals, within the literature there has been little discussion of coherent signal and noise on microseismic data. Geophysicists are aware that surface microseismic data typically has a low signal-to-noise ratio. Cultural noise and ground roll, for example, can all be recorded on surface seismic data. Although wind noise and ground roll may less prevalent on borehole microseismic data, there are a number of coherent noise phenomena that may be recorded. A number of these are presented in Chapter 6 of this thesis.

Many types of noise can be transmitted to and within borehole steel casing. Surface noise such as nearby drilling and production operations can reach the borehole and be transmitted along the borehole (Warpinski, 2009). There may also be surface seismic data being acquired in the area that could be recorded by the microseismic geophone array. Cultural noise such as vehicle or rail traffic can create noise sources. The hydraulic fracture treatment itself may be a noise source. These sources of noise can be transmitted in water in the borehole, in the steel casing, or in the casing cement (e.g. Rama Rao and Vandiver, 1999). Consider Figure 1.7, showing where noise can travel along the casing, within a fluid filled borehole, or along the cement interface. All of these waves have

characteristic frequencies, modeshapes, particle motion and attenuation (Rama Rao and Vandiver, 1999).

Some sonde configurations and installation characteristics can lead to noise amplification. For example, geophone coupling within the pipe can be a problem. Geophones must be adequately clamped to casing that has competent cement to prevent excessive vibration (Gaiser et al., 1988). Reflections from simple supports such as pipe centralizers can occur (Galvagni and Cawley, 2010). Transmission of Stoneley waves or Lamb waves within the borehole may also occur. For example, Rama Rao and Vandiver (1999) extensively studied acoustic of fluid-filled boreholes and found that many types of wave modes can be present and travel in the casing, the casing cement, or the fluid.

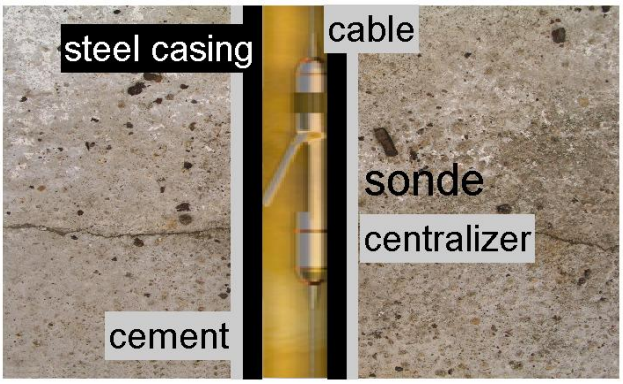

Figure 1.7 – Cross-section of a wellbore with a clamped sonde. There are many waves that can be generated and propagated along the casing, cement, and cable or reflected by casing centralizers.

The signal and coherent noise studied in this thesis is interpreted to be similar to microseismic data acquired in other areas with similar geology. The data presented here were acquired as part of eight microseismic datasets licensed to the University of Calgary for analysis purposes. The datasets are from Alberta and British Columbia and comprise passive seismic recordings of hydraulic fracturing of low permeability and porosity reservoirs from 1800 m to over 3000 m depth. Some of the datasets contain very high signal to noise ratio data, as presented in Chapter 3. On the other hand, some of the data have marginal signal to noise ratio P– and S–wave arrivals, as presented in Chapter 4.

1.7 **Thesis outline**

This thesis investigates four phenomena recorded on microseismic data that have received scant discussion in the literature. The intention is to describe the phenomena using physical principles and to investigate how their observed characteristics may be used to increase our understanding of the subsurface. This thesis is ordered into five following chapters and associated appendices. The content of four of the chapters have been or will be submitted to peer-reviewed journals for publication.

The first study examines numerous coherent low-frequency (<100 Hz) arrivals characterized by conspicuous dispersion and quasi-linear moveout. Their apparent velocities and dispersion characteristics are consistent with Lamb waves, an elastic guided wave that propagates within finite media such as plates or cylindrical casing. Lamb waves have the potential to be used for monitoring degradation of casing cement over time.

The second study examines two datasets to characterize frequency shifts in discrete narrow passbands caused by wellbore acoustic transmissivity due to geophone clamping. Evidence is presented showing that the resonances changed during two fracture stimulations in response to changes in hydraulic fracture treatment pressure. Analytical and finite-element models suggest that these may be caused by a relative change in geophone clamping force as the pressure external to the wellbore varies. This sensitivity suggests that passive seismic monitoring can be used for the downhole detection of relative stress changes.

The third study focuses on frequency content variations of a set of 20 high S/N P- and S-wave arrivals. The 20 events were grouped into four clusters based upon a geolocation algorithm and event cross-correlations. Spectral analysis shows variation in the signal within event subsets. A 2-D elastic finite-difference simulation using a layered model shows that this variation could be ascribed to path effects associated with propagation of the signal from the source to the receivers.

The fourth study examines a potential long-period long-duration (LPLD) seismic event and analyzes the phenomena in detail. LPLD events observed on microseismic data have been likened to deep low frequency tremor attributed to slow-slip processes along pre-existing fractures or strike-slip regimes at subduction zones (Das and Zoback, 2012). The event may be the result of hydraulic fracture fluid leak-off out of the intended zone into a pre-existing fracture.

Chapter Two: - Lamb waves recorded in wellbores and their potential to predict cement bond failure

2.1 **Summary**

Microseismic data recorded during several hydraulic fracture treatments in western Canada reveal numerous coherent low-frequency (<100 Hz) arrivals characterized by conspicuous dispersion and quasi-linear moveout. The apparent velocities, observed dispersion and frequency attenuation of these events are consistent with Lamb waves, a type of elastic guided wave that propagates within finite media such as plates or cylindrical casing. The postulated Lamb waves documented in this study appear to originate at (or near) the base of the wellbore casing and are interpreted to arise from impingement of P- and S-waves generated by microseismic events induced during hydraulic fracturing. Excitation of longitudinal or torsional Lamb models may depend on the polarization of the incident wave, and may be limited to P- and S-wave arrivals that contain sufficient energies at low frequencies. The propagation characteristics of Lamb waves are defined by the acoustic and geometrical properties of the borehole fluid, casing and cement. A simple borehole model used as a basis for calculations suggest that Lamb wavespeeds may be sufficiently sensitive to the shear velocity of cement to enable their use for monitoring degradation of casing cement over time.

2.2 **Introduction**

Lamb waves, first described by Lamb (1917), are a type of elastic guided wave that propagates within finite media such as plates or cylindrical casing. In a thin

plate, Lamb waves can be described as the superposition of two Rayleigh waves travelling along both sides of the plate (Feenstra, 2005), or alternatively as a coupled P-S_V guided mode. In steel- cased and cemented wellbores, Lamb waves propagate dispersively at specific frequencies and velocities that are defined by the acoustic and geometrical properties of the borehole fluid, casing and cement (Burago et al., 1980). Observation of Lamb waves thus offers the potential to infer the acoustic properties of the borehole casing and the immediately surrounding material.

A variety of other types of waves can propagate along the axis of a cemented wellbore with steel casing. For example, bulk P- and S-waves can be transmitted in a wellbore within the steel casing or within the cement (Karpfinger, 2009). Compressional waves can also be transmitted as tube waves within the fluid in the wellbore (e.g. Bokov and Ionov, 2001). Rama Rao and Vandiver (1999) measured three modes of tube waves with velocities ranging from 700 to 1530 m/s at frequencies up to 1000 Hz. The three modes travel in the pipe, the pipe fluid or the pipe/strata interface and are characterized by their dispersion, attenuation, mode shapes and particle motions. Stoneley waves, a type of guided wave that propagates along a single interface, have been investigated by Stevens and Day (1986) as a tool to measure shear velocities around a wellbore. All of these waves have characteristic apparent velocities, dominant frequencies and dispersion properties. For example, P-waves propagate in steel (with Young's modulus between 188 GPa and 216 GPa) with velocities $5640 \leq V_P \leq 6100$ m/s and $3220 \leq V_S \leq 3280$ m/s (Raggio et al., 2007).

The characteristics of Lamb waves are best known for propagation within plates (Rocha-Gaso et al., 2009), but they have also been studied within a cylindrical co-ordinate system applicable to borehole casing. Lamb waves are characterized by discrete modes and for most cases a numerical approach is required to solve the governing equations. For wellbores, Burago et al. (1980) used Lamb waves to investigate porosity and permeability of the host rock. Their work showed that, in the case of low frequencies, the surrounding medium affects the velocity of the Lamb wave through the shear modulus of the cement in contact with the casing.

Lamb waves have been used for a number of years for non-destructive evaluation (NDE) of pipelines (see Davies, 2008). In this application, transducers are used as sources that selectively excite a Lamb-wave mode by generating a source pulse into the pipeline with the applicable phase velocity. These modes have long propagation distances, and their response to defects is well known from modelling, measurements and field observations. For example, Long et al. (2003) discuss high-frequency (MHz) Lamb waves in buried iron pipes and document methods to identify and diagnose problems such as cracks or pipeline irregularities.

In our experience, Lamb waves are common and readily observable during microseismic monitoring surveys acquired in cased and cemented wellbores; yet, there has been scant mention of them in the microseismic literature. In this paper, we present examples of events that may be low-frequency Lamb waves recorded during the microseismic monitoring of hydraulic fracture treatments. We begin by describing the general characteristics of Lamb waves and present a representative set

of dispersion curves for a typical cased wellbore. Next, we present and analyze recordings for two microseismic datasets from western Canada. These recordings are interpreted to be Lamb waves recorded during the same time frame as P- and S-wave arrivals throughout two hydraulic fracture treatments. Finally, we investigate the possibility that Lamb waves may be used to monitor the integrity of casing cement by modelling borehole geometry with competent and weakened cement behind casing.

2.3 **Characteristics of Lamb waves**

For a thin plate (where the plate thickness is less than one wavelength), a Lamb wave can be viewed as the superposition of two Rayleigh waves propagating simultaneously on both sides of the plate (Feenstra, 2005). Like Rayleigh waves, a Lamb wave can also be thought of as the constructive interference of P- and S_v-waves, as discussed in the Appendices 1 and 2. In a hollow cylinder such as a cased wellbore, the plate ends are wrapped back onto themselves to form a continuous boundary. Gazis (1959) provided the fundamental framework for the estimation of longitudinal and torsional Lamb wave velocities using Bessel functions and the linear theory of elasticity. The coupled particle motions result in three sets of modes, as shown in Figure 2.1.

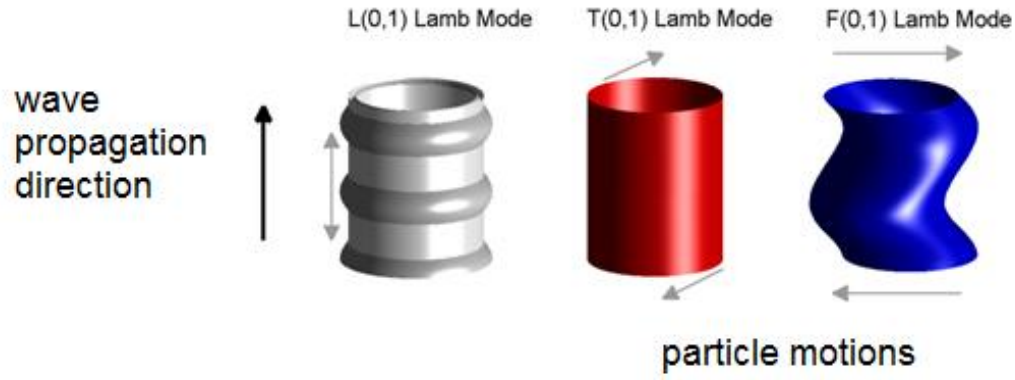

Figure 2.1 - Particle motion for Lamb waves in a cylinder for fundamental longitudinal, torsional and flexural modes, respectively. In cylinders, the Lamb wave motion is dominated by fundamental longitudinal L(0, 1) or torsional T(0, 1) modes (Long et al., 2003).

From Silk and Bainton (1979), the three modes are written as:

1. Longitudinal symmetric modes: $L(0, m)$, $(m = 1, 2, 3, 4\ldots)$

2. Torsional symmetric modes: $T(0, m)$, $(m = 1, 2, 3, 4\ldots)$

3. Flexural symmetric modes: $F(n, m)$, $(n = 1, 2, 3, 4\ \ldots, m = 1, 2, 3, 4\ldots)$

The parameter *m* counts the mode of vibrations within the wall of the cylinder and *n* counts the number of waves spiralling circumferentially around the cylinder.

Dispersion curves describe the group velocity of Lamb waves as a function of frequency. A representative set of dispersion curves for longitudinal Lamb modes is shown in Figure 2.2. These curves were calculated using numerical code developed by Karpfinger (2009), based on typical parameters for a cemented steel wellbore

(Table 1). For frequencies less than ~300 Hz, these curves show that for the longitudinal modes, only the *L(0,1)* longitudinal mode exists for this choice of model parameters. This mode exhibits significant dispersion, as manifested by frequency-dependent phase velocity. A torsional mode should also exist.

In principle, an infinite number of Lamb wave modes can exist in a physical model, at progressively higher frequencies with increasing mode number. In practice, Lamb modes are limited by the frequency band of the acquisition system, as well as the bandwidth of the source. Formulation of the dispersion curves comes from the solution of the period equation, as presented in Achenbach (1973) and given here in Appendix 2. In general, Lamb longitudinal modes travel at velocities less than the P-wave velocity of the casing, but greater than the S-wave velocity (Karpfinger, 2009).

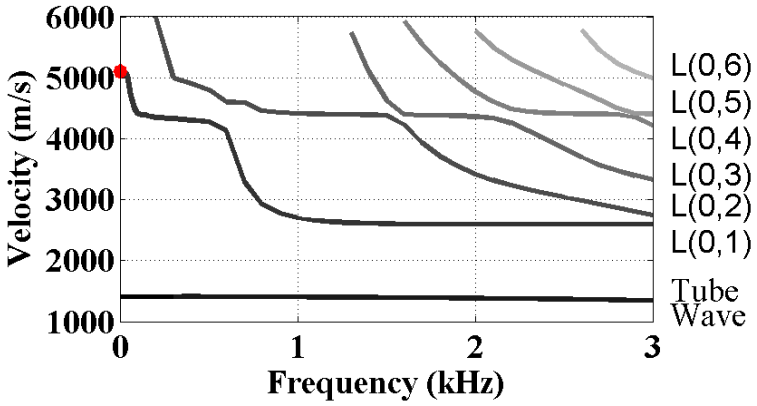

Figure 2.2 - Dispersion curves for a tube wave and longitudinal Lamb waves calculated using the values in Table 2.1 with software from Karpfinger (2009). All longitudinal Lamb wave modes are dispersive. At a frequency of ~ 45 Hz, the velocity of the *L(0,1)* longitudinal mode is predicted to be ~ 5100 m/s. The D.C. estimate (marked by the red dot) is from Burago et al. (1980).

2.4 **Microseismic Data Examples**

The data used for this study were acquired during microseismic monitoring of two hydraulic fracture treatments in western Canada. Microseismic survey # 1 recorded 8.5 hours of data at a 0.25 ms sample rate during the hydraulic fracture treatment of a horizontal well. The drilling depth to the zone of interest is ~ 2400 meters (~ -1550 m subsea). Eight levels of three-component passive seismic data were recorded in a vertical borehole with cross-sectional parameters shown schematically in Figures 2.3 and provided in Table 2.1.

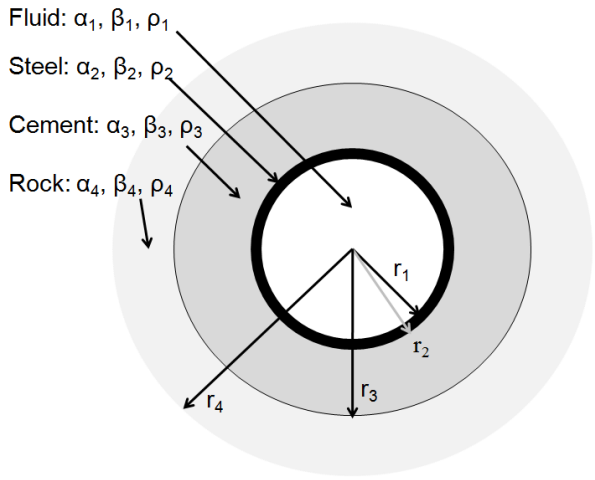

Figure 2.3 - Cross section through a wellbore. There may be fluid within the steel casing (black) cemented to the outermost strata. Each layer is characterized by its compressional and shear velocity, and bulk density.

				Radii, r_i (m)	
annular area	V_P (m/s)	V_S (m/s)	ρ, density (gm/cm3)	Survey 1	Survey 2
Inner Fluid	1500	-	1.00	0.100 m	0.100 m
Steel Casing	5930	3200	7.85	0.120	0.120
Borehole Cement	4200	2400	2.20	0.250	0.250
Rock Formation	4800	2800	2.60	2.700	2.700

Table 2.1 – Wellbore parameters used to compute representative dispersion curves. For Figure 2.3, $\alpha_i = V_{Pi}$ and $\beta_i = V_{Si}$.

Figure 2.4 shows a 0.5 s segment of data containing an example of an interpreted Lamb wave recorded on the array. Initially, the plot shows the interpreted arrival of an S-wave at position '1'. The S-wave has a slight hyperbolic movement and is recorded on most of the north and east component traces, similar to the interpreted S-waves in Figure 2.5 recorded on the same microseismic dataset. The wave at time position '2' is interpreted to be an upgoing Lamb wave. This wave is travelling at ~5100 m/s +/- 200 m/s. At the -1420 m depth, a wave begins to travel downward. Also, at the shallowest geophone level, the upward going wave reflects and travels downward at the same velocity as the initial upgoing wave. From Table 2.1, the initial upgoing wave velocity of 5100 m/s is less than that of steel and greater than that of the cement or the surrounding formation.

The event is much lower frequency than recorded P- and S-wave events. This can be seen by visual inspection of the P- and S-waves shown in Figure 2.5. Figure 2.6 shows the Z-component frequency spectra for the upgoing wave in Figure 2.4. These spectra and a plot of the peak frequency as a function of trace depth (Figure

2.7) shows frequency attenuation as represented by the decrease in the peak frequency as the wave travels 210 m up the borehole.

A Z-component "velocity spectral analysis" plots, or vespagram, for the upgoing waves in Figure 2.4 is shown in Figure 2.8. A vespagram is a plot of apparent velocity coherence for straight line apparent velocities as a function of recording time (Rost and Thomas, 2002).

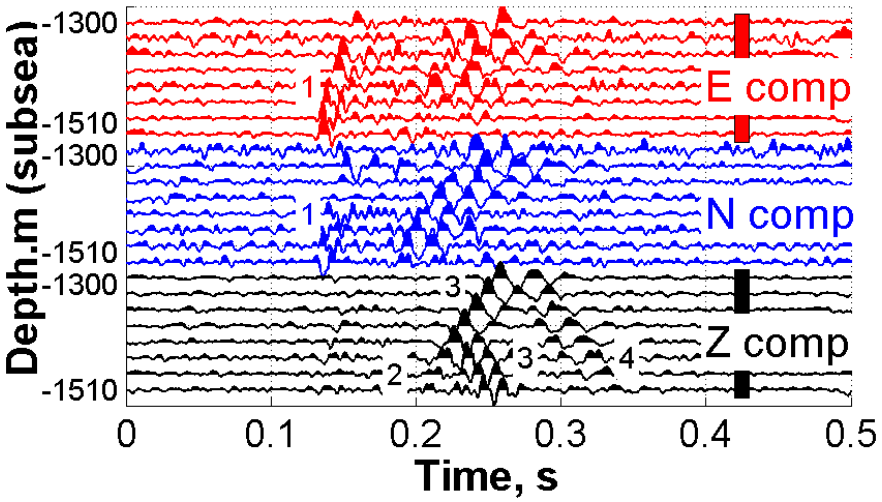

Figure 2.4 – An interpreted Lamb wave from dataset 1. The data are plotted after a 5/10-180/220 Hz. bandpass filter. The data have been rotated on the H-1 and H-2 components using vibroseis sweeps to orient the horizontal geophones. An S-wave arrival consistent with other S-wave arrivals at position 1 is recorded on the horizontal channels. At position 2, the upgoing reflection travelling 5100 m/s is modeled to be an L(0,1) longitudinal Lamb wave.

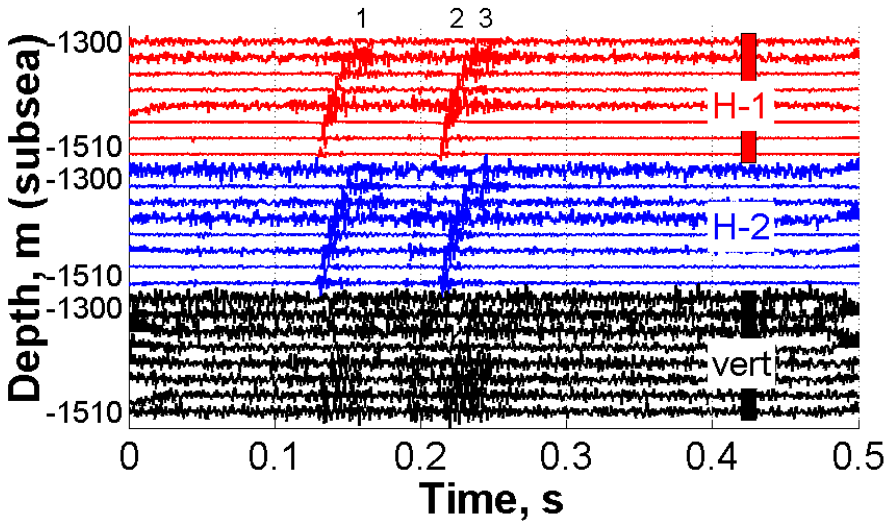

Figure 2.5 – One P-wave arrival (event 2) and two S-wave arrivals (events 1 and 3) from the first dataset.

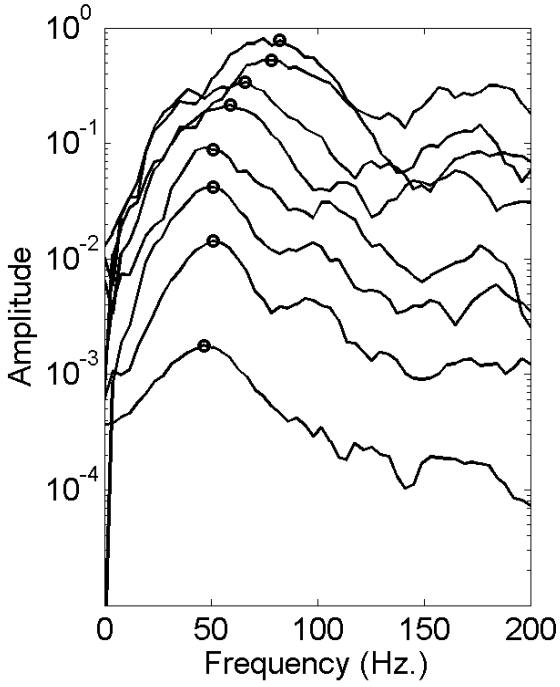

Figure 2.6 – Z-component frequency spectra for the upgoing wave at position 2 in Figure 2.4. The deepest traces are at the top and have the highest frequency content.

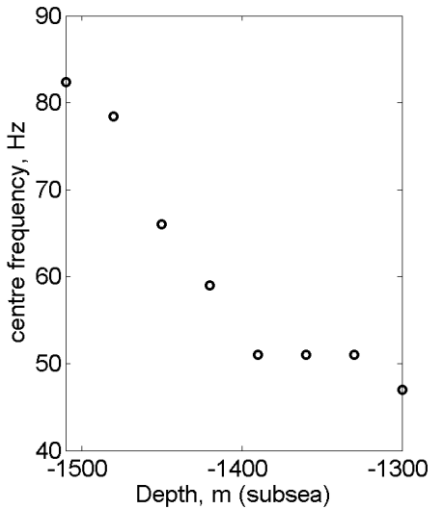

Figure 2.7 – Plot of the centre frequencies from Figure 2.5. There is a 40 Hz drop in the peak frequencies over 210 m.

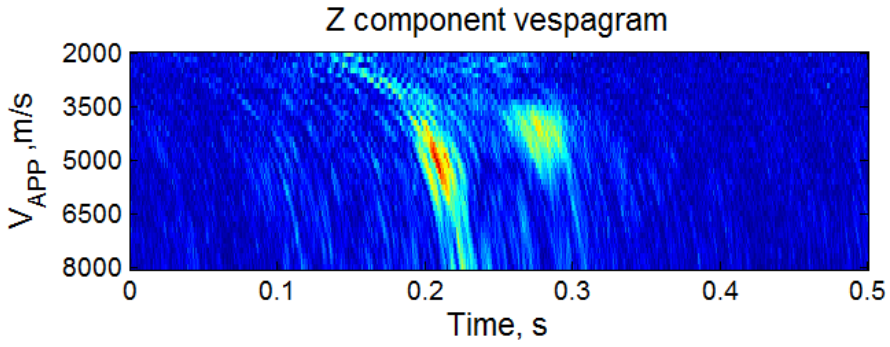

Figure 2.8 – Z-component vespagram for the upgoing waves in Figure 2.4. The Lamb waves have a V_{APP} ~ 5100 m/s.

Figure 2.9 shows hodogram crossplots for the upgoing wave at the -1390 m depth recording for the Z-component traces compared to either of the vertical component traces. Hodograms are a crossplot of the particle motion energy arrival

over a time window (Mahob and Castegna, 2001). Most of the energy is recorded on the Z-component.

Figure 2.10 shows the energy of the upgoing wave in Figure 2.4 as a function of geophone depth. The energy wave computed by the sum of the squares of all amplitudes 10 ms either side of the upgoing energy. The energy decreases by a factor of ~10 as the wave travels up the borehole. Note that Figure 2.4 is trace equalized.

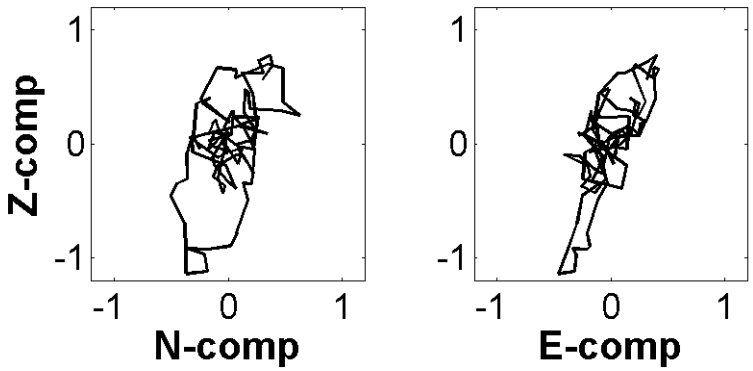

Figure 2.9 – Hodograms crossplotting trace amplitudes for the upgoing wave recorded at the -1390 m depth position from Figure 2.4. Most of the energy aligns with the Z-component.

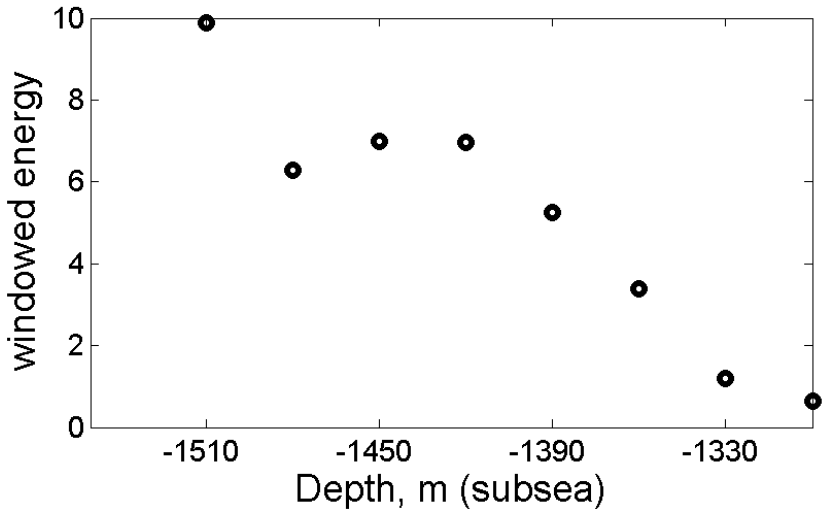

Figure 2.10 – Plot of the upgoing trace energy from Figure 2.4.

Over 60 events similar to the event in Figure 2.4 were observed during the 8.5 hours of recording for this hydraulic fracture treatment. They were similar in terms of lower overall frequency content, consistent apparent velocity of ~ 5100 m/s, hodogram analysis showing energy concentrated on the vertical component, frequency decrease with distance and amplitude attenuation. Also, most of the events had downgoing wave energy as shown in Figure 2.4

Microseismic survey # 2 recorded 5.5 hours of data at a 0.25 ms sample rate. Three-component data were recorded in a vertical borehole at 12 levels, with a geophone interval of 12.47 m. Dimensions and acoustic properties for the wellbore are shown in Table 2.1 and Figure 2.3. Figure 2.11 shows a 0.5 s segment of data from the survey containing an example of an interpreted Lamb wave. In Figure 2.11, a wave is initially recorded on all traces at the time indicated by time position “1” on

the figure. At time position "2" on all traces, there is a lower apparent velocity wave recorded. This is followed by a low velocity event at position "3" and a higher velocity event at position "4". The event at time position '4' is interpreted to be a Lamb wave.

Figure 2.12 shows an interpreted P- and S-wave from the same survey. These events have higher frequency content than the interpreted Lamb wave in Figure 2.11. The Z-component frequency spectra for event "4" in Figure 2.11 are shown in Figure 2.13, along with the peak centre frequency plot in Figure 2.14. There is a greater than 20 Hz decrease in the centre frequency as the wave travels 137 m up the wellbore.

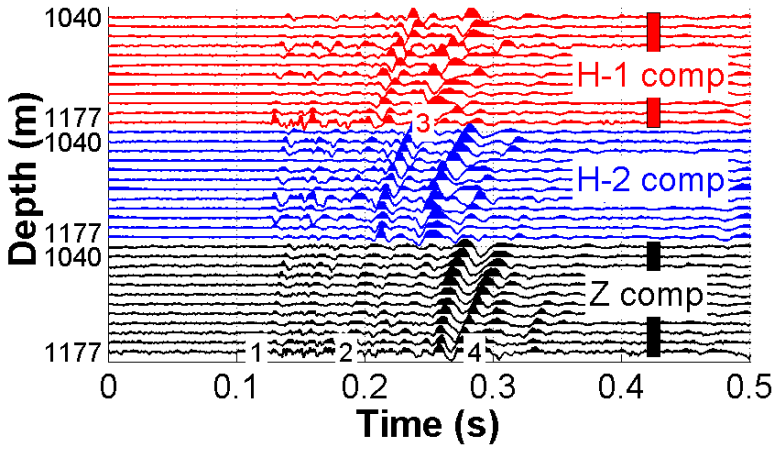

Figure 2.11 - A Lamb wave event from microseismic dataset 2. The data are plotted after a 5/10-280/320 Hz bandpass filter. Energy with an apparent velocity of almost 7000 m/s at time position "1" is followed by another signal at time position "2". Positions "3"and "4" denote signal on the H-1 component and the Z-component.

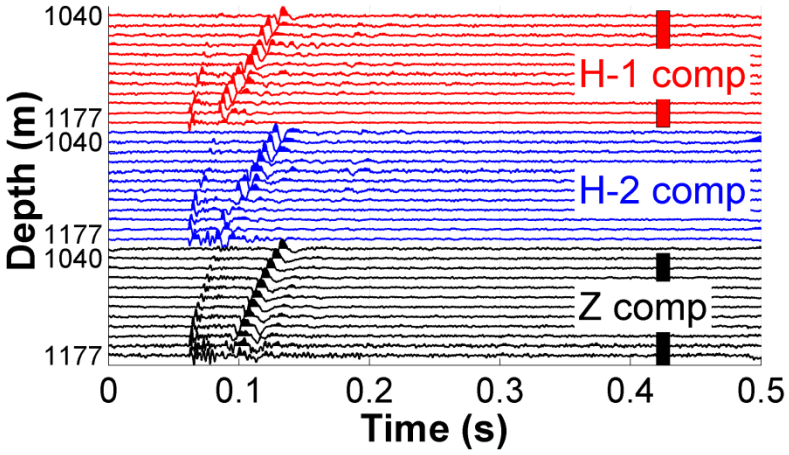

Figure 2.12– An interpreted P- and S-wave from the survey.

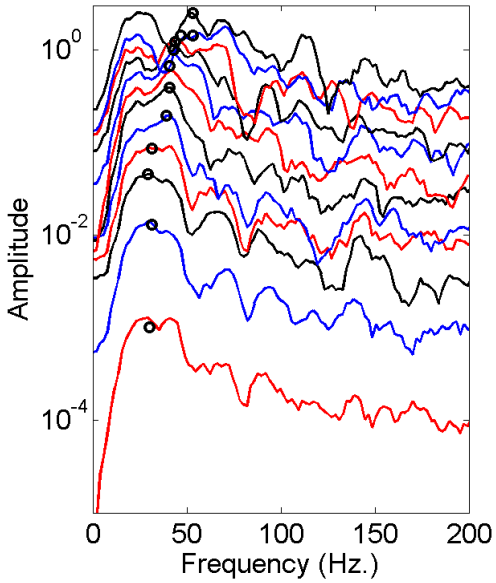

Figure 2.13– Z-component frequency spectra for the upgoing wave at position 2 in Figure 2.11. The deepest traces are at the top and have the highest frequency content.

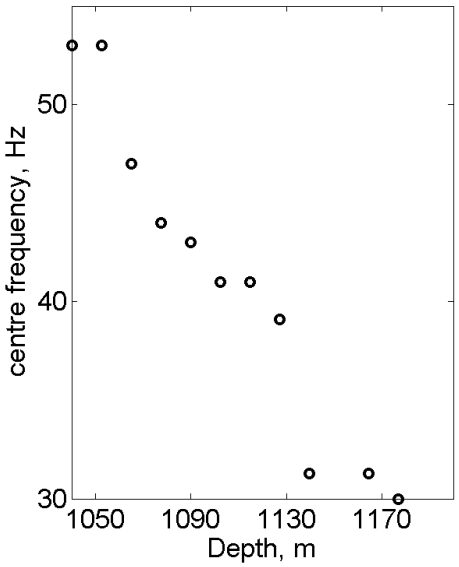

Figure 2.14 – Plot of the centre frequencies from Figure 2.13. There is a 40 Hz drop in the peak frequencies over 210 m.

Figure 2.15 shows two vespagrams for the lowermost Z-component and H-1 component geophone traces. Although significant smearing of the events is evident, the dispersive nature of the signals is apparent from the curved high-amplitude region in the vespagram. Note that the highest coherence for the interpreted Lamb wave is between ~5000 and ~6000 M/s.

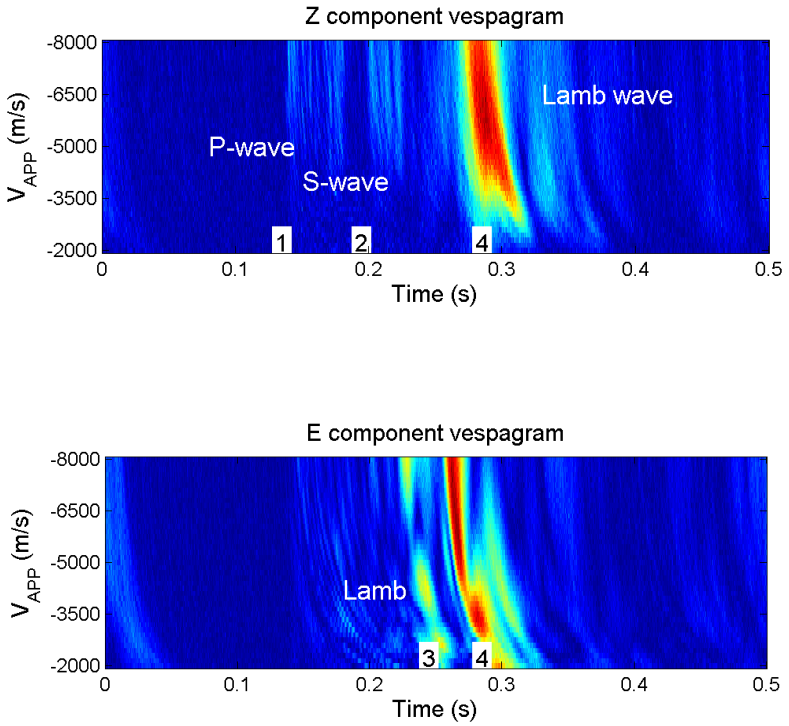

Figure 2.15 - Two vespagrams showing the linear apparent velocities for the upward travelling waves on the Z- and H-1 components in Figure 2.6. Numbers correspond to those used in Figure 2.6. The red areas show higher coherence in the vespagram.

Figure 2.16 shows hodograms from geophone level 6 for the wave arrivals at time position "4". Figure 2.17 shows the energy of the Z-channels in Figure 2.11 as a function of geophone depth. The energy wave computed by the sum of the squares of all amplitudes 10 ms between 0.25 and 0.35 s as shown in Figure 2.11. Unlike Figure 2.10, the energy does not decrease as a function of distance travelled.

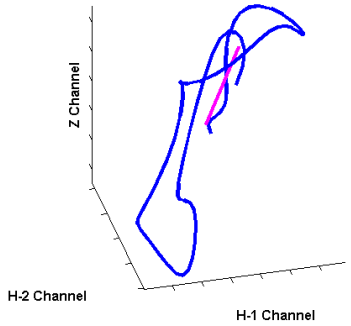

Figure 2.16 – Hodogram crossplots from level 6 (1102 m depth) for the P-wave arrival (top left) for time position "4" in Figure 2.6. The pink line indicates the principal eigenvector from the covariance matrix (Kanasewich, 1981). The wave arrival has most of the energy on the Z-component.

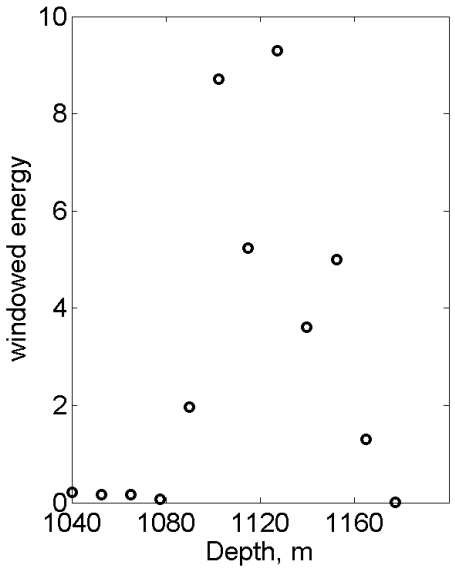

Figure 2.17 – Plot of the upgoing trace energy from Figure 2.4.

Based on careful inspection, 96 events similar to that in Figure 2.11 were observed in dataset 2. The events were similar in terms of lower overall frequency content, consistent apparent velocities as shown in Figure 2.15, hodogram analysis of energy concentrated on the Z-component, frequency decrease with distance and amplitude attenuation.

2.5 **Discussion**

The two events presented may be Lamb wave recorded on microseismic data. Both events (Figures 2.4 and 2.11) have apparent velocities consistent with Lamb waves travelling a cylinder. Both events have low frequency content compare to P- and S-wave arrivals (Figure 2.5 and 2.12).

The waves could be interpreted to be from P- and/or S-wave energy offset from the borehole with apparent velocities defined by their angle of arrival. However, the downgoing apparent velocity equivalence with the upgoing apparent velocity in Figure 2.4, the concentration of the energy on the Z-component for the hodograms in Figures 2.9 and 2.16 and the modeling results that Lamb waves should exist at low frequencies (Figure 2.2) support the postulation that the events are Lamb waves.

Lamb waves recorded in steel casing should arise from the impingement of P- and S-waves events with sufficient energy at low frequencies. To test for this, both datasets were examined. Figure 2.18 shows a histogram for the occurrence of the 96 events similar to the event in Figure 2.11 for microseismic survey #2. Over 700 P– and/or S-wave arrivals were observed during the same 8.5-hour time interval. The 96 events generally occurred during or after bursts of P- and/or S-wave activity. Not

all P and S-waves are followed by Lamb waves, as can be seen in Figure 2.12.

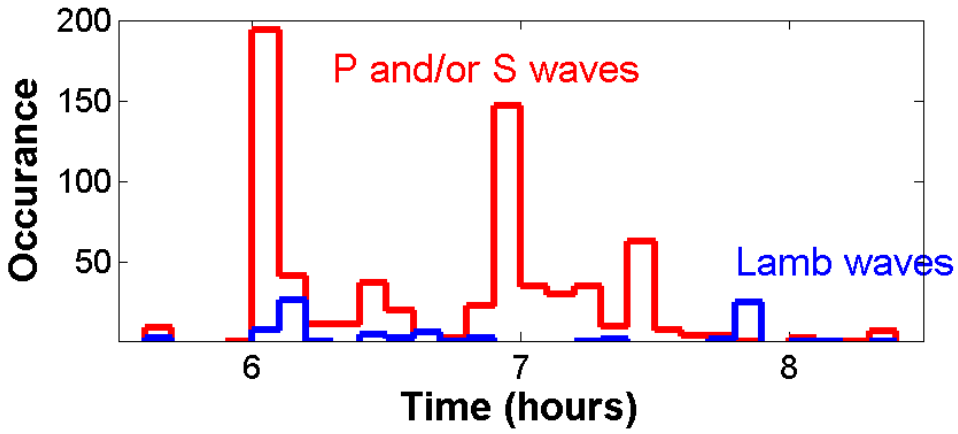

Figure 2.18 – Rate of occurrence (in 6 minute blocks) for 96 Lamb waves in survey #1 compared to the 700 P and/or S-waves.

In general, to excite a wave mode in non-destructive pipeline testing, the inherent motion (longitudinal or torsional) needs to be imposed on the casing. Individual modes are activated by choosing a frequency range and incident angle that will excite a particular mode. In the data shown here, a Lamb mode could be initiated if a P- or S-wave impinged upon the wellbore at the appropriate apparent velocity to excite a Lamb wave mode. A spherical wave could arrive at a cylindrical casing at a number of angles to initiate a Lamb wave. For the wellbore shown in Figure 2.5, P-waves incident to the casing up to a 55° angle could excite a coupled P – S_V wave in the steel.

When the upgoing Lamb wave in Figure 2.4 reaches the approximate midpoint of the downhole geophone assembly, a downgoing wave with a similar apparent velocity is initiated. At the top of the geophone assembly another downgoing wave

initiates. This appears to be the reflection of the upgoing wave. Such a reflection could occur if there were an assembly connected to the pipe (Galvagni and Cawley, 2010). Alternatively, poorly cemented casing may initiate the reflection (Li and Leary, 1990). Moreover, the downgoing reflection from the midpoint could be caused by the Lamb wave reflecting at a casing centralizer at that location. Casing centralizers are installed to the outside of production casing as the casing is sent down the wellbore. Their purpose is to allow for cement to surround the production casing within the wellbore. The centralizer locations were not recorded for this wellbore.

Figure 2.19 shows the sonic and density logs for the recording wellbore with the geophone locations. Within the depth limits of the geophone array, there is little impedance contrast that could cause a wave reflection. A shear wave sonic log was not recorded in this wellbore. Below the base of the wellbore, however, an impedance contrast is present where the reservoir shale unit overlies a high-velocity carbonate layer.

Most of the Lamb waves in survey 2 occurred shortly after the arrival of P- and S-waves. However, not all P- or S-wave arrivals initiated a Lamb wave. The observations of Lamb on additional datasets are required to definitively prescribe a cause and effect relationship for Lamb wave initiation.

Based on examination of the propagation of inferred Lamb modes, it appears that there is energy incident at the base of the casings that is exciting the steel to create an upgoing wave. Consider Figure 2.20. The target zone in both offsetting horizontal wellbores is just below the base of the monitoring wellbore, resulting in

subhorizontal arrival of P and S-waves at the base of the casing. Moreover, the bottom of both well casings had perforated casing and cement, since both wells were producers prior to installation of plugs to isolate the downhole microseismic toolstring from the producing zone. The pre-existing perforations could have made this part of the borehole more poorly coupled to the surrounding media, providing a preferential location for casing vibration and generation of Lamb modes.

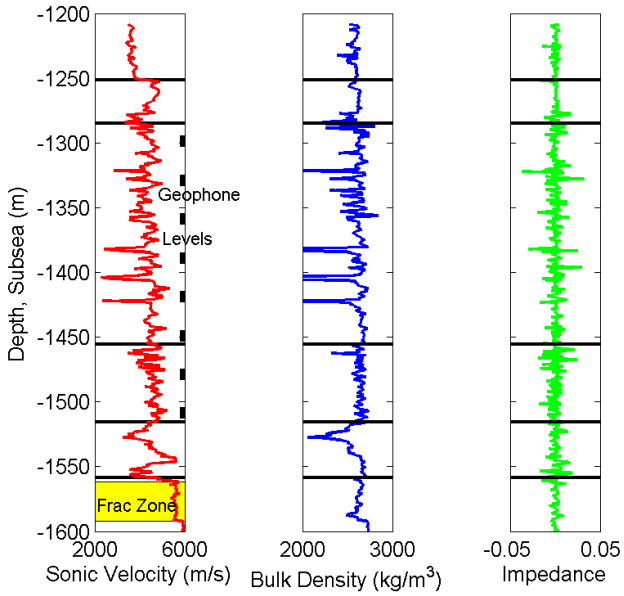

Figure 2.19 - Sonic and bulk density borehole logs and computed impedance from the monitoring well for dataset 1. The reservoir shale is highlighted in yellow. A carbonate layer with higher velocity underlies the targeted zone. Shear velocity logs were not recorded in the wellbore. The geophones are installed in a layer of little velocity or density contrast.

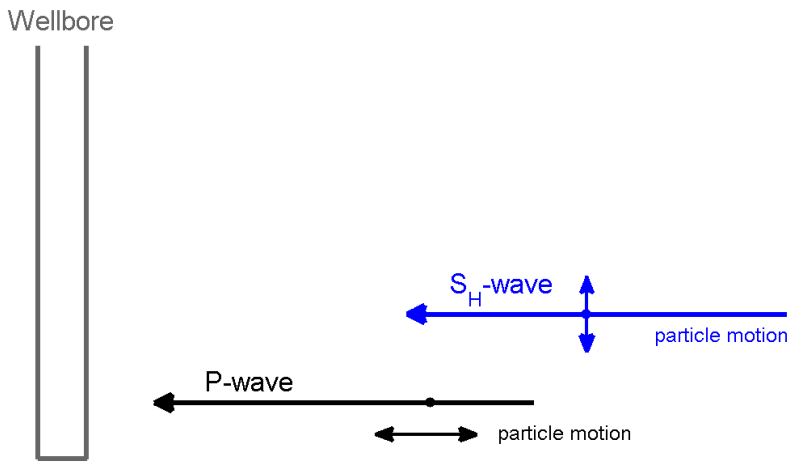

Figure 2.20 – Model for excitation of Lamb waves at the bottom of a wellbore. The P-wave impinges on the wellbore first and initiates a torsional wave. Subsequently, the S-wave impinges and initiates a longitudinal wave.

We now consider the effects of modifying the shear-wave velocity of the cement bonding. The purpose of this numerical study is to investigate the potential of Lamb waves as a tool for *in situ* monitoring of the condition of the cement behind the casing. The numerical approach of Karpfinger (2009) was used to model a longitudinal *L(0,1)* Lamb wave using degraded cement parameters shown in Table 2.1. A shear velocity reduction results from severe cement degradation, as highly fractured cement would have little or no shear strength (Pickett, 1963). The computed dispersion curves for these models are displayed in Figure 2.21. We note that the assumed reduction in shear velocity of the cement leads to a ~300 m/s decrease in the *L(0,1)* Lamb wave velocity at low frequencies. Based upon the measured variance of the interpreted Lamb wave velocities in this study (+/- ~200

m/s), it is uncertain if failed cement could be detected with these apparent velocity measurements. Repeat measurements of Lamb-wave velocity using a permanently installed geophone array may potentially identify cement deterioration.

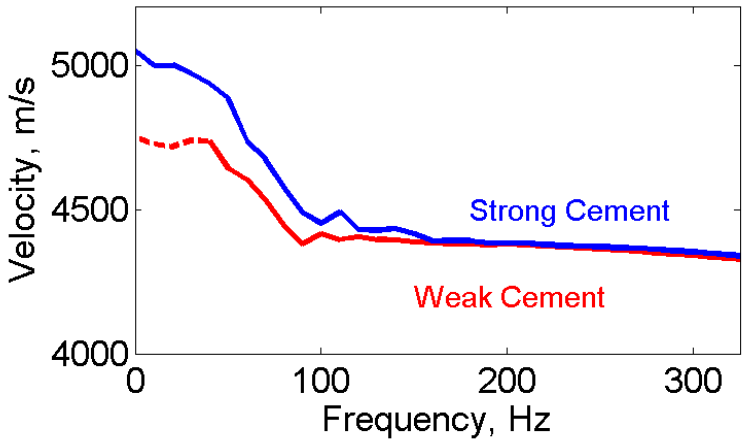

Figure 2.21 - Longitudinal Lamb waves modeled using the values in Table 2.1. The upper (blue) curve is from a competent casing cement model; the lower (red) curve is from cement with reduced shear strength.

2.6 **Conclusions**

Microseismic data recorded during the hydraulic fracturing of two horizontal wells in western Canada have been examined to identify coherent signal and noise. Numerous events interpreted to be Lamb waves were identified on both datasets based on apparent velocity, low frequency content and apparent velocity characteristics that are consistent with analytical and modeled results. The interpreted Lamb waves could have been initiated by P- and S-waves impinging on the cased wellbores near the bottom of the well, close to the treatment zone.

Numerical modeling of Lamb-wave dispersion indicates that it might be possible to use measured changes over time in Lamb wave velocity in a borehole to detect deterioration of cement behind casing.

Chapter Three: Borehole Acoustic Transmissibility and Fracture-Induced Stress Variations

3.1 **Summary**

Passive seismic data recorded in deep observation wellbores for hydraulic fracture monitoring (HFM) are typically used to detect P- and S-wave arrivals from induced microseismic events. These signals are usually recorded through steel casing using geophone arrays that are mechanically clamped to the inside of the casing. Clamping of the geophones can alter the acoustic properties of the casing, resulting in comb-like spectra containing discrete narrow transmission bands. These spectra can be simulated to a high degree of accuracy using an acoustic transfer matrix (ATM) approach, as similarly used to investigate signal transmission along segmented drill strings. Analysis of continuous passive recordings during hydraulic-fracture treatments shows that the transmission-band frequencies vary with time and correlate with injection pressure. Scaling of the frequencies with geophone spacing and temporal variations during the well treatment precludes a simple interpretation of these observations as tool resonances. The results of modeling, coupled with the field observations of injection pressure, indicate that the observed phenomena are related to stress perturbations in the host formation, suggesting a possible novel application of passive seismic monitoring for downhole detection of relative stress changes.

3.2 **Introduction**

3.2.1 Hydraulic fracturing and stress measurements

Hydraulic fracturing has emerged as an important method to improve permeability and production for tight hydrocarbon reservoirs. Microseismic methods are being increasingly used for hydraulic-fracture monitoring to locate induced fractures and fracture networks (e.g. Hayles et al., 2011; Johnston and Shrallow, 2011). Microseismic data are used to detect the arrival of P- and/or S-wave energy that reaches the borehole from an induced fracture source and to infer a "stimulated rock volume" (Mayerhofer et al., 2008). Pore-pressure changes from the injection of high-pressure fluids coupled with zones of weakness associated with activation and/or development of fracture networks are expected to produce significant changes in the stress environment around the wellbore (e.g. Haimson and Cornet, 2003; Hickman and Zoback, 1983).

This study evaluates the potential use of continuously recorded microseismic data to detect stress changes associated with hydraulic fracturing, as opposed to using these data for locating fracture networks directly. Understanding the stress environment is important in the development of oil and gas reservoirs and can impact many facets of exploration and production. For example the stress field plays a role in planning directional drilling (e.g. Lei et al., 2012), controlling the evolution of a reservoir during production (e.g. Alqahtani et al., 2011) and/or hydrocarbon flow paths (Brown, 2005), and prediction of hydraulic-fracture initiation according to the Mohr-Coulomb failure criterion (Suckale, 2010).

There are a number of ways to measure stress in the subsurface (Schmitt et al., 2012). For example, Grandi-Karam (2008) examined various ways to measure *in-situ* stress, including use of borehole logs and surface-seismic data. Schmitt et al. (1986) used holographic interferometry to measure *in-situ* stress in a borehole. Hatchell and Bourne (2005) interpreted movement of event locations (hypocentres) over time as an indication of strain-induced deformation and fluid migration in a petroleum reservoir. This work is pertinent for understanding reservoir changes over a long period of time. As discussed below, the potential also exists to use microseismic data for real-time detection of stress changes in the vicinity of a monitor wellbore.

3.2.2 Cylindrical shell vibration

Microseismic data are often acquired using an array of geophones within a borehole. A simple approximation for understanding the mechanical behavior of a steel-cased borehole is to consider it as a cylindrical shell with axial symmetry. The elastic vibration of cylindrical shells has been investigated for a number of years. For example, some attention has been given to wave modes within boreholes (e.g. Gazis, 1959; Rama Rao and Vandiver, 1999). Fung (1955) looked at the vibration of pressurized cylinders in rockets. The vibration of ring-stiffened cylindrical shells has also been examined for airplane design and submarine design (Virgin, 2007). Singh and Mallik (1979) examined the harmonic response of a pipe filled with flowing fluid and supported at periodic intervals. Wave theory has been used to predict the harmonic oscillations that occur as a function of fluid velocity; for example, Liu and Li (2011) presented a frequency-domain

approach for calculating the harmonic oscillation of pressure constrained liquid-filled pipes. All of these analyses consider vibrations inherent to a physical system similar to steel casing within a wellbore; however, none have addressed or explained the observed phenomena documented here.

3.2.3 Acoustical response of a steel rod and a drill string

This chapter examines discrete frequency pass-bands recorded by geophone arrays clamped to steel-lined wellbores cemented to surrounding strata. It is expected that equidistantly clamped geophones inside a cemented wellbore should have predictable acoustical properties that differ from the casing alone, as the geophone clamping alters the acoustic impedance of the casing. Analogous work in acoustic studies was performed in the early part of the last century. Stewart (1922) showed that a metal tube consisting of repeated sections of impedance contrasts can be used to construct low-pass, high-pass or band-pass filters for a simple plane wave travelling along and within the tube. The interference of transmitted and reflected waves (from the periodic impedance contrasts) results in the frequency filtering of the wave as it travels along the tube.

A number of investigators have examined the acoustical response of geometrical objects that were built to be analogous to electrical circuits. Mason (1927) examined combinations of steel tubes with connected Helmholtz resonators to construct acoustic filters similar to electrical filters and may have been the first to present the comb-filter equation (3.3) used in this study. Lindsay (1929) commented on the work of Stewart (1922) and Mason (1927) and examined the filter response of alternating very short and long length impedance contrasts in a steel tube. Their results also showed that the tube

acted as a frequency filter for a compression wave travelling along the tube. Linsday (1934) looked at the filtering of torsional and longitudinal waves through solid rods with equally spaced larger diameter disks attached to the outer diameter of the solid rod. Linsday and White (1934) continued the work of Lindsay (1934) by developing an equation to predict pass bands for an acoustic wave travelling along a steel rod loaded with equidistantly spaced weights attached by springs. The weighted springs changed the impedance contrast of the rod at the attachment points, where the incident 1-D acoustic wave was both reflected and transmitted. An acoustic wave passing through the rod was either low-pass, high-pass or band-pass frequency filtered, depending upon the geometric configuration of the experiment.

A drill string is a length of steel pipe between the surface and the drill bit. The acoustic properties of drill strings have been studied for assessing the viability of transmitting signals from the drill bit to the surface within the drill string. Drill strings usually consist of equidistant lengths of pipe that are threaded together. These threaded connections that have a larger diameter (hence a different impedance contrast) than the remainder of the pipe. Barnes and Kirkwood (1972), Drumheller (2002) and Lous et al. (1998) used an ATM approach to describe sound transmission through a drill pipe, in an effort to transmit drilling information along the drill string. An ATM relates the acoustic pressure, Φ, and volume velocity, U for a wave at two locations in a medium with prescribed acoustic impedance. As detailed below, the ATM approach can be used to describe filtering phenomena associated with such a regular arrangement of drill pipes.

3.2.4 Acoustical response of a cased wellbore with clamped geophones

Guided waves travelling within a steel rod or a drill string are analogous to waves traveling in wellbore casing with an array of clamped geophones. One objective of this study is to understand the filtering properties of a borehole containing a clamped geophone array that is subject to varying stress conditions in the surrounding strata. Given the similarities between borehole casing with equidistantly clamped geophones and drill strings, the mathematical formulism of the ATM can be applied to understanding the filtering response of clamped geophone arrays.

The focus of this work is to offer an explanation for observations from two microseismic datasets recorded in western Canada. Both datasets show regularly spaced narrow transmission pass-bands (herein referred to as a "comb-spectrum" because of the distinct equidistantly spaced pass-bands) with time-dependent spectral peaks. Strictly speaking, this is not a resonant phenomenon; although the observed comb-spectra resemble discrete resonant peaks, the underlying physical mechanism differs. Here, the narrow-band spectra represent the residue of suppression of frequency bands, rather than selective amplification of defined frequencies.

I begin by presenting equations to model vibrations in a resonating cylinder. Next, I present an ATM approach to model waves travelling in a hollow steel pipe with equidistantly spaced restrictions. This approach is supplemented by analytical and numerical (finite-element) modeling of a hollow pipe with restrictions. All three approaches show that a wave travelling in a pipe with equidistantly spaced restrictions will only be transmitted along the pipe at very narrow frequency pass-bands. These pass-

bands are determined by the geometry of the pipe and its restrictions and the wavespeed of the pipe material. A change in the pass-band frequencies can be modeled by a change in the size of the restriction. If the restriction is caused by a change of the relative clamping force of equidistantly spaced clamped geophones, I conjecture that temporal changes in the pass-band are a proxy for changes in external stress conditions. The comb-spectrum models provide an excellent fit to the observations. Moreover, crossplots of hydraulic fracture injection pressure and comb-spectrum frequency for the duration of two hydraulic fracture treatments support this conjecture.

3.3 **Vibrations of a resonating cylinder and borehole acoustic transmissibility**

3.3.1 Vibration

A cased borehole can be approximated as a simple closed (at one end) cylinder, which will resonate at a frequency proportional to the cylinder length divided by the appropriate wave velocity. The P-wave velocity in casing type 40 steel is about V_P = 5600 to 6100 m/s (Raggio et al., 2007). The corresponding resonant wellbore frequency with a casing length in the range of the microseismic monitoring wells would be ~ 1.0 Hz, much below the values discussed here. The resonant frequency of a closed cylinder will change if there are internal stiffeners placed a distance L apart in the borehole (Kwong and Edge, 1998). In this case, the fundamental resonant frequency and its integer harmonics are predicted by

$$f_{res} = n * V_P / L \text{ Hz}, \qquad n = 1, 2, 3. \tag{3.1}$$

For example, for dataset 2 presented below, the geophones were placed 12.37 m apart in the borehole. Equation (3.1) predicts a fundamental vibration frequency of 467 Hz (using V_P = 5780 m/s for the steel pipe compression velocity), which matches an observed spectral peak near the onset of the hydraulic fracture monitoring. Doubling and tripling of this value predicts the second and third simple harmonics.

3.3.2 Acoustic-transfer matrix

Markos and Soukoulis (2008), King (2007) and King and Cox (2007) discuss an ATM method for the analysis of the wave propagation in one-dimensional systems. A compression wave travelling in a cylindrical wellbore with azimuthal symmetry can be treated as a 1-D system. For the velocities and dimensions of wellbore casing, a compression wave can be treated as a plane wave. As detailed in Appendix 5, the ATM is given by

$$\begin{pmatrix} \Phi(0) \\ U(0) \end{pmatrix} = \begin{pmatrix} \cos(kL) & j\frac{Vp\,\rho_0}{S}\sin(kL) \\ j\frac{S}{\rho_0 Vp}\sin(kL) & \cos(kL) \end{pmatrix} \begin{pmatrix} \Phi(L) \\ U(L) \end{pmatrix} \quad , \tag{3.2}$$

where $\Phi(x)$ denotes acoustic pressure, $U(x)$ denotes volume velocity (i.e. particle velocity u multiplied by the annular area of the casing), k denotes wavenumber, V_P denotes compressional wave velocity, ρ_0 denotes density and $j = \sqrt{-1}$.

If a borehole has n equidistantly spaced lengths each with a different acoustic impedance, the ATM defined by (3.2) can be used n times to analytically solve for the change in acoustic pressure as a function of frequency encountered at a distance that encompasses the entire length of the impedance contrasts. There is one ATM for each

section of the cylinder that has acoustic impedance different than the adjacent sections. This is a convolutional filter and the response is multiplicative. An example of the implementation of (3.2) is discussed in section 3.3.5.

3.3.3 Comb-spectrum filters

Barnes and Kirkwood (1972), Drumheller (1989) and Lous et al. (1998) presented variations of a model to describe sound transmission through drill pipe with equidistantly spaced drill collars at the pipe connections. The aim of their research was to determine if sound could be transmitted through drill pipe to convey drilling information to the surface by sending pulses through the drill pipe. Drill pipe segments have thicker diameter portions known as drill collars or tool joints where the individual pipes are screwed together. As a result, drill collars have different acoustic impedances than the main sections of the drill pipe. This results in the drill pipe acting as a frequency filter.

Barnes and Kirkwood (1972) showed that for tool joints (each W meters wide) spaced L meters apart, frequencies that can propagate through the pipe are required to satisfy an inequality, given in our notation by

$$|\cos(2\pi fW/V_P)*\cos(2\pi f(L-W)/V_P) -$$

$$(v_{pipe}/v_{clamp} + v_{clamp}/v_{pipe})*\sin(2\pi f/V_p\, W)*\sin(2\pi f/V_p\,(L-W))| < 1 \quad , \qquad (3.3)$$

V_P is the steel pipe compression wave velocity, f denotes the frequencies transmitted through a solid steel cylinder with restrictions of width W placed a distance L apart. In the case of drill strings, the restrictions are steel discs attached to the inner diameter of the

cylinder. The term v_{pipe} is the volume for the pipe section which is given by $\pi*(r_o^2-r_i^2)*(L-W)$, where r_o = outer pipe radius, r_i = inner pipe radius. Similarly the term v_{clamp} is volume for the clamp section, given by $\pi r_o^2 W$. Mason (1927) may have been the first to describe an equation similar to (3.3).

3.3.4 COMSOL modelling

COMSOL is finite-element modeling software from COMSOL Multiphysics Ltd. The software allows the definition of complex shapes with material properties and boundary conditions. Partial differential equations can be added to this model and iteratively solved using a number of algorithms. Carcione and Poletto (2000) developed a finite-element model of a drill string and their results agree well with the ATM results. In this study, COMSOL was used to construct a finite-element model for a steel cylinder, as discussed in Appendix 6. The cylinder was equivalent in diameter to the steel casing used for both datasets presented here. The restrictions were represented as thin steel discs equivalent to the inside diameter of the cylinder. The restrictions were placed 12.37 m apart, equivalent to the geophone spacing in dataset 2. An acoustic wave was modelled in COMSOL, and the pressure amplitudes were recorded at various locations along the length of the cylinder.

3.3.5 Analytical and finite-element modelling results

Three different methods were used to model sound transmission through a steel cylinder with restrictions. First, an ATM was implemented using MATLAB to model the clamped geophones in dataset 2 as thin restrictions of steel inside a cylinder equal to the casing dimensions for both wellbores. The model is schematically shown in Figure 3.1.

The results of the calculations are shown in Figures 3.2 and 3.3. Figure 3.2 compares the ATM frequency passbands with the finite-element model results and equation (3.3), showing that these approaches yield consistent results.

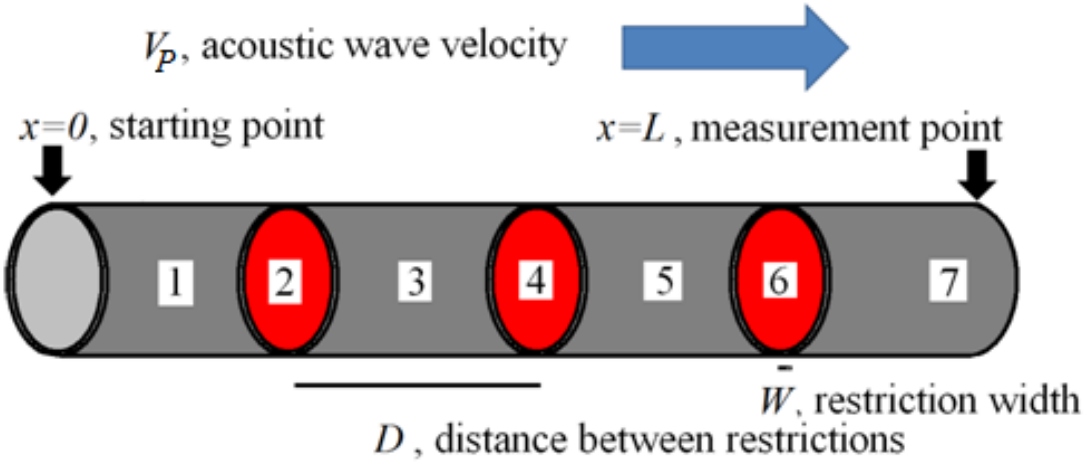

Figure 3.1 – Schematic illustration of a steel cylinder with thin discs acting as acoustic impedance contrasts along the inside of the pipe. To calculate the acoustic displacement amplitudes at x=L, equation (3.1) would be implemented 7 times using the values in Table 3.1 The model for Figures 3.2 and 3.3 had 11 restrictions spaced 12.37 m apart for a total of 23 acoustic impedance contrasts along the pipe.

Pipe section	ri, m	r_o, m	ρ_0, kg/m^3	V_P, m/s	L, m
1	0.100	0.117	7820	5780	12.37
2	0	0.117	7820	5780	0.001
3	0.100	0.117	7820	5780	12.37
4	0	0.117	7820	5780	0.001
5	0.100	0.117	7820	5780	12.37
6	0	0.117	7820	5780	0.001
7	0.100	0.117	7820	5780	12.37

Table 3.1 Parameters for the first 7 of 23 pipe sections used to produce Figure 3.2.

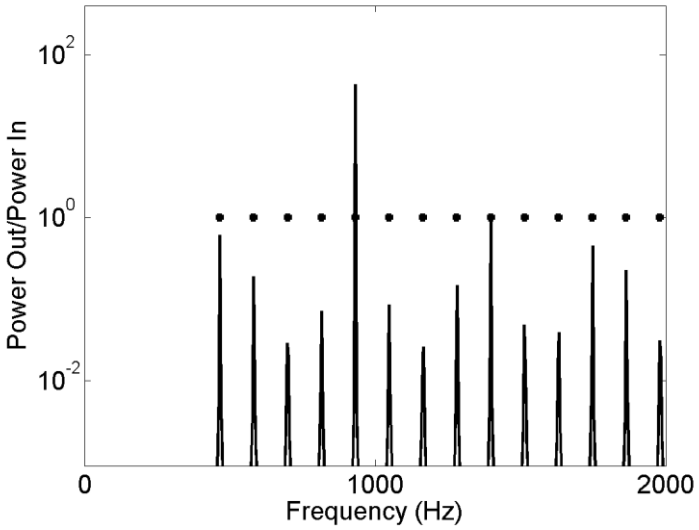

Figure 3.2 –Results from COMSOL finite-element modeling (dots) end Equation 3.2 (identical dots) compared to the acoustic transfer matrix (lines), based on an 11-segement model described by Figure 3.1 and Table 3.1.

The relative amplitudes of the frequencies in Figure 3.2 in the passband are very consistent and depend upon the number of elements in the ATM and the placement of the source within the borehole. Similar amplitude variations are observed in the data, as discussed below. This is one characteristic used to identify the comb-spectra as being the result of an acoustic transmissivity phenomenon.

Figure 3.3 shows that the passbands have a finite width that depends up the acoustic impedance of the restrictions as compared to the remainder of the cylinder. Also, the higher frequencies in the comb scale proportionately to the lowest frequency in the comb-spectrum. If the lowest frequency in the comb changes by Δf, the higher frequencies will

each scale by $n\Delta f$, where $n \geq 5$. These two observations also help to identify the comb-spectra as being the result of an acoustic transmissivity phenomenon.

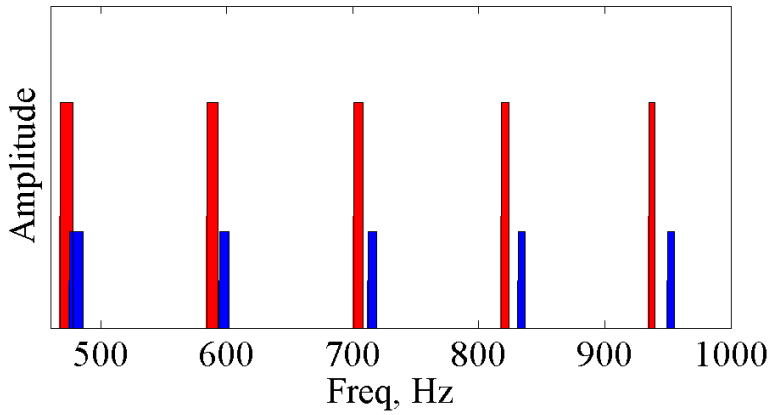

Figure 3.3 – Fine structure of the comb spectra predicted by equation (3.3), showing that the passbands have a finite width and the higher frequency passbands scale at 5/4, 6/4, 7/4 ... of the lowest frequency in the comb-spectrum. Here, V=5780 m/s, L = 12.37 m, W = 0.001 m for the red passbands and W = 0.02 m for the blue passbands. Note the change in W adjusts both the transmitted frequencies and the width of the passbands.

3.4 **Data**

3.4.1 Observations

The phenomena considered here are examined by analyzing data recording during two hydraulic fracture microseismic monitoring datasets from western Canada. Acquisition parameters are summarized in Table 3.2. Both datasets were recorded in boreholes with steel casing cemented to the surrounding strata. Figure 3.4 shows the recording geometry for the first dataset, which used a vertical monitoring well located 800 m SW of a 2200 m long horizontal treatment well. The reservoir is a low-porosity

Middle to Upper Devonian carbonate zone in northeast British Columbia. Although the reservoir has a thickness up to 140 m, the porosities only average 3.5% with an average permeability of ~ 300 nD. To increase productivity in this gas bearing zone, horizontal wells are usually drilled and hydraulically fractured. The hydraulic fracture treatment for the wellbore in Figure 3.4 was a 12 stage treatment. Each stage required the perforation of a solid steel liner in the wellbore and required one day to perform and used ~4000 m^3 of fluid and 300 tonnes of sand at downhole pressures approaching 100 MPa.

A geophone array with seven 3-component geophones recorded 9 of 12 hydraulic fracture treatments. The geophones were mechanically clamped to the borehole with ~4450 N (~1000 lbs) of force, as suggested by the manufacturer and reported by the contractor. Figure 3.5 shows a representative 2 s data sample extracted from 60 hours of continuous microseismic data. The geophones at level seven (the deepest level) recorded no data during this time period, and the five shallowest levels recorded what appears to be random noise at this scale. However, the 0.1 s expanded plot in Figure 3.5 shows the vertical alignment of high-frequency data on some traces, such as at 0.055 s on the Z-component traces.

Dataset	Tool spacing	Sample interval	Number of geophones
Dataset 1	15 m	0.333 or 0.5 ms	7 3-component
Dataset 2	12.37	0.25	12 3-component

Table 3.2 – Recording parameters for the two downhole assemblies manufactured by Avalon Sciences Ltd.

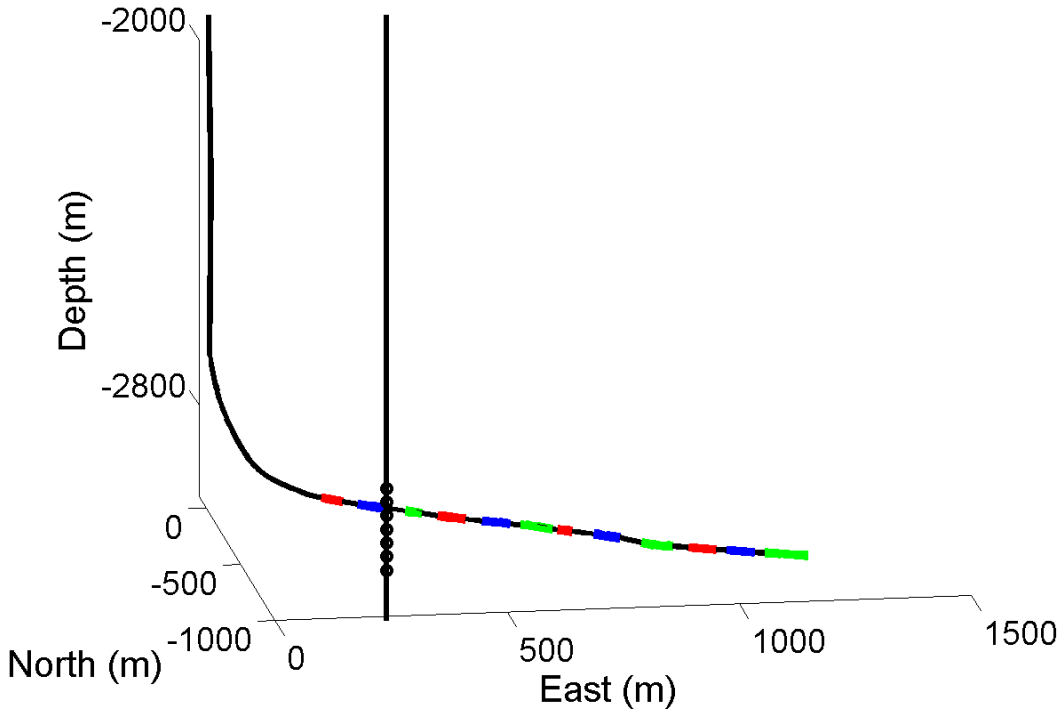

Figure 3.4 – A perspective view of the recording geometry for dataset 1. The observation well is about 800 m southwest of the horizontal well. The treatment stages are shown by different colours.

Figure 3.6 shows a representative frequency-amplitude spectrum for the shallowest north component trace from Figure 3.5. Several peaks correspond to commonly observed resonant noise sources, such as the 120 Hz harmonic of 60 Hz electrical noise. Lines highlighted with circles, however, represent frequencies that are unrelated to these noise sources. The lowest marked frequency (375 Hz) is interpreted as the first frequency in a "comb-spectrum". This frequency is equivalent to a P-wave travelling in a steel pipe at 5625 m/s divided by the geophone spacing distance.

Two of the higher comb frequencies in Figure 3.6 correspond with the simple integer harmonics of the first frequency predicted by equation (3.1). Intermediate frequencies in the comb-spectrum occur at ¼ intervals of the first frequency in the comb-spectrum and are predicted by (3.2) or (3.3). Thus, the next frequency in the comb occurs at 5/4 times the first frequency. These spectral lines have higher amplitude than the background level, and are well above noise thresholds. The comb-spectrum persists, subject to small variations as documented below, for the duration of the entire 60-hour monitoring on all data channels. The comb-spectra frequencies are in the audible band; the observed acoustical properties are similar to a clarinet (Dickens et al., 2007).

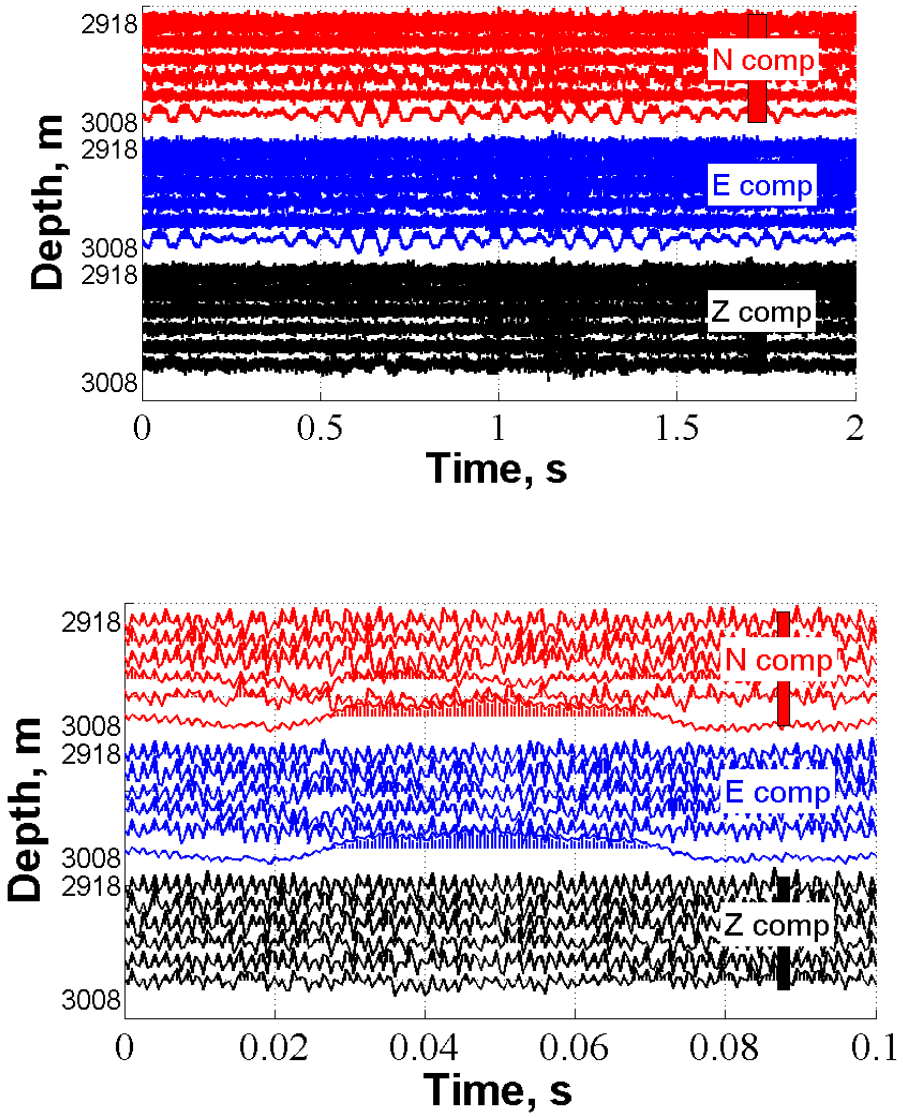

Figure 3.5 - A 2 s seismic data plot (upper) and the first 0.1 s from this plot (lower) from the first dataset. Geophone levels for the first 5 traces starting at 2918 m depth appear to have random noise on all three of their components.

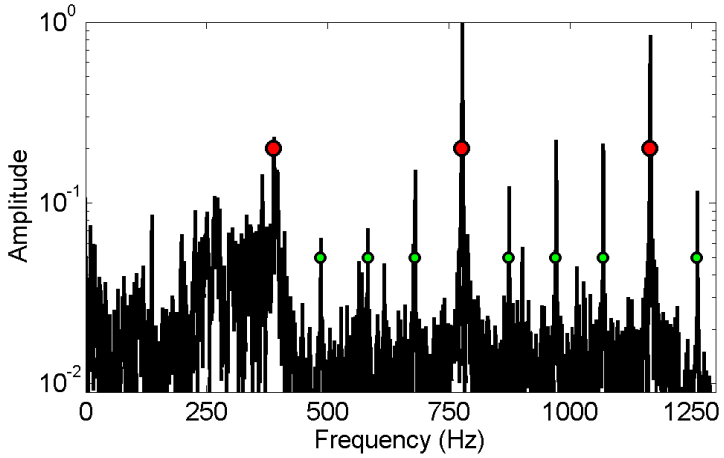

Figure 3.6 – The frequency-amplitude spectrum for the 2918 m depth N-component trace from Figure 3.6. The lowest-frequency in the comb-spectrum (under the first red dot) occurs at 375 Hz. The two other red dots overlie the double and triple harmonics. The small green dots are equidistant between the simple harmonics. A model using the acoustic transfer matrix predicts all of the comb-spectrum frequencies.

Figure 3.7 shows the autocorrelation for a portion of the shallowest N-component 2 s trace shown in Figure 3.2. This figure is representative of both datasets shown here. The autocorrelations do not have their energy concentrated near zero lag. The autocorrelation of signal that persists throughout a time series is itself a distribution that persists through time. As stated above, the comb-spectrum persists throughout both datasets, including 60 hours for the dataset in Figure 3.5.

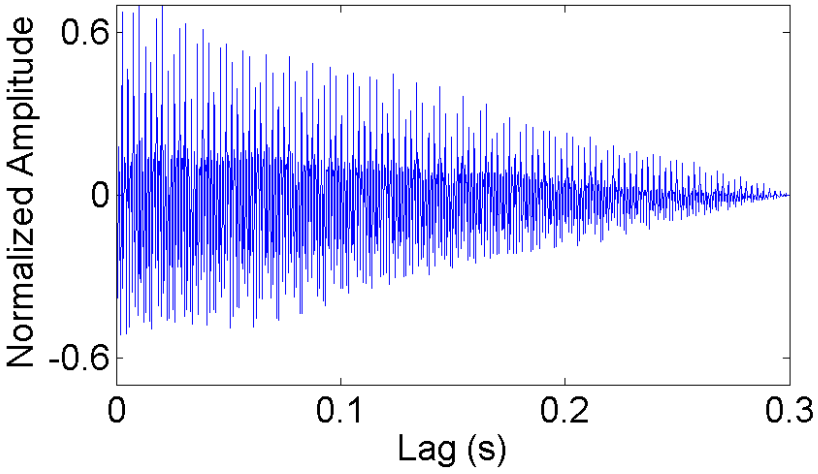

Figure 3.7 – The autocorrelation of trace 1 from Figure 3.5 showing only the positive lags. The decrease in the amplitude is the result of the short (0.3 s) autocorrelation window. The autocorrelation is not the result of random noise.

An automatic algorithm was implemented to detect peak frequencies (Appendix 4). The temporal variations in the first frequency (fundamental) component for one stage of the first dataset are shown in Figure 3.8. This graph shows the median values for the detected first comb-spectrum frequency on all horizontal and vertical channels that recorded data during the first recorded stage of the hydraulic fracture treatment. Throughout the monitoring, the first peak frequency gradually changed from about 370 Hz to 385 Hz and then fell abruptly to about 355 Hz. Also shown in this figure is a plot of the downhole treatment pressure as a function of time. Due to lack of clock synchronization between the microseismic acquisition system and the hydraulic fracture treatment program, a 20-minute time shift has been applied to the treatment data to align it (for purposes of illustration) with temporal variations in the comb-spectrum

fundamental frequency. The correlation between frequency and downhole pressure in Figure 3.8 is discussed below.

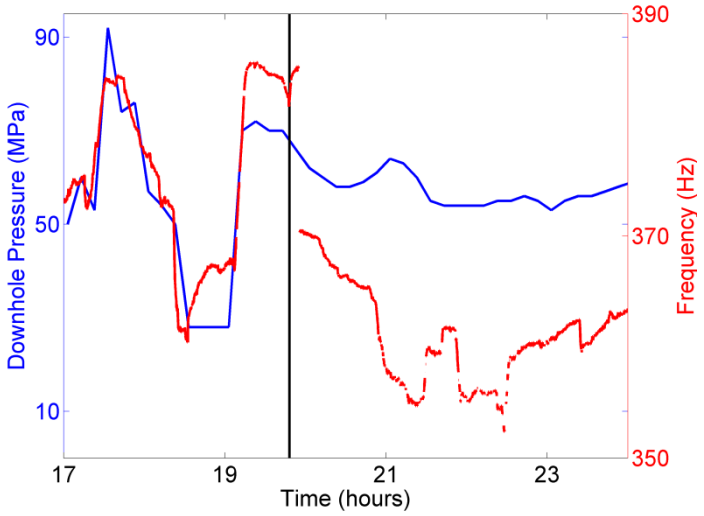

Figure 3.8 – The temporal variation for first frequency in the comb-spectrum for stage 3 from dataset 1, as indicated by the red line. Equation (3.2) would predict the initial frequency of 375 Hz using a steel velocity of 5625 m/s, as the geophones are 15 m apart in the borehole. Also, plotted is the downhole pressure from the injection well (blue line). The fracture treatment was initiated at 19:48 hours on this plot.

Figure 3.9 depicts the recording geometry for the second dataset. Here, a geophone array with 11 3-component geophones recorded 10 stages of a 14-stage treatment program that took place over ~ 4.5 hours. Each stage used approximately 100 m^3 of fluid and 25 tonnes of sand. The monitoring well was situated 50 m north of the treatment well. Following standard practice, the stages progressed from the "toe" (i.e. the terminus of the drilled wellbore) of the well and continued to the "heel". This was an open-hole

completion, i.e. there was no casing in the horizontal portion of the treatment wellbore. Much less time was required as compared to the first dataset because the reservoir zone did not have casing in the borehole.

The hydraulically fractured zone is a low permeability Cretaceous-aged Cardium sandstone/shale reservoir. In the area, porosities range from 9 to 13%, with permeabilities in the 0.1 to 10 mD range (Fik et al., 2011). Sonic logs for the area calculate P-wave velocities ranging between 3000 and 3800 m/s for beds 200 m above and below the reservoir zone.

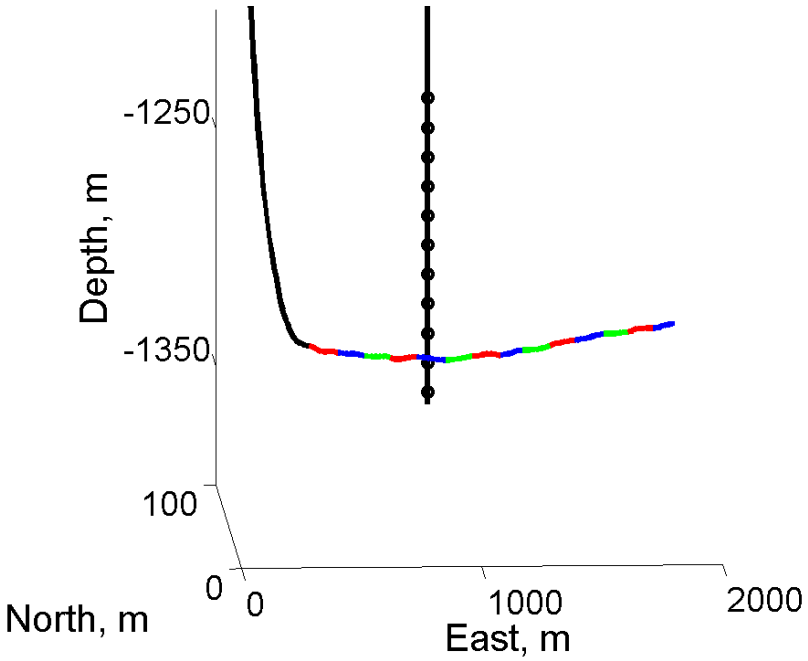

Figure 3.9 – A perspective view of the central Alberta horizontal treatment well and vertical observation well. The observation well is only 50 m away from the horizontal well. Each of the 14 stages is a different colour.

Figure 3.10 shows a representative 2 s data sample from 4.5 hours of continuous microseismic data from dataset 2. The geophones recorded no P- or S-wave energy during this time period. Similar to the previous example, the traces again recorded what appears to be random noise at this scale. However, a 0.1 s expanded plot in Figure 3.2 shows the vertical alignment of high frequency data on some traces at 8 locations, especially on the east and north component channels as indicated by the arrows in Figure 3.10.

Figure 3.11 shows the spectrum for a representative two-second window from this dataset. Again, some commonly observed resonances are present, such as the 60 Hz peak from electrical noise. As in the previous example, every geophone recorded a comb-spectrum. In this case, however, the first frequency spike of interest occurs at about 468 Hz, which again is equivalent to the P-wave velocity in steel pipe travelling at 5780 m/s divided by the geophone spacing distance. Two of the higher frequencies in the comb are simple integer harmonics of this initial value, whereas others are equally spaced between the fundamental and integer harmonics at ¼ intervals of the lowest frequency in the comb-spectrum.

The temporal variations in the lowest frequency of the comb-spectrum for all monitored stages of the second dataset are shown in Figure 3.12. This graph shows the median values for the detected fundamental comb-spectrum frequency on 25 of the 33 channels that recorded data. The other 8 channels exhibited a greater degree of variation caused by noisier results in the selection of the local maxima and are not shown here. Throughout the monitoring, the first peak frequency gradually rose from about 468 Hz to

476 Hz and then fell to about 462 Hz by the end of the treatment. The median value for these 25 frequency vs. time plots is shown in Figure 3.13.

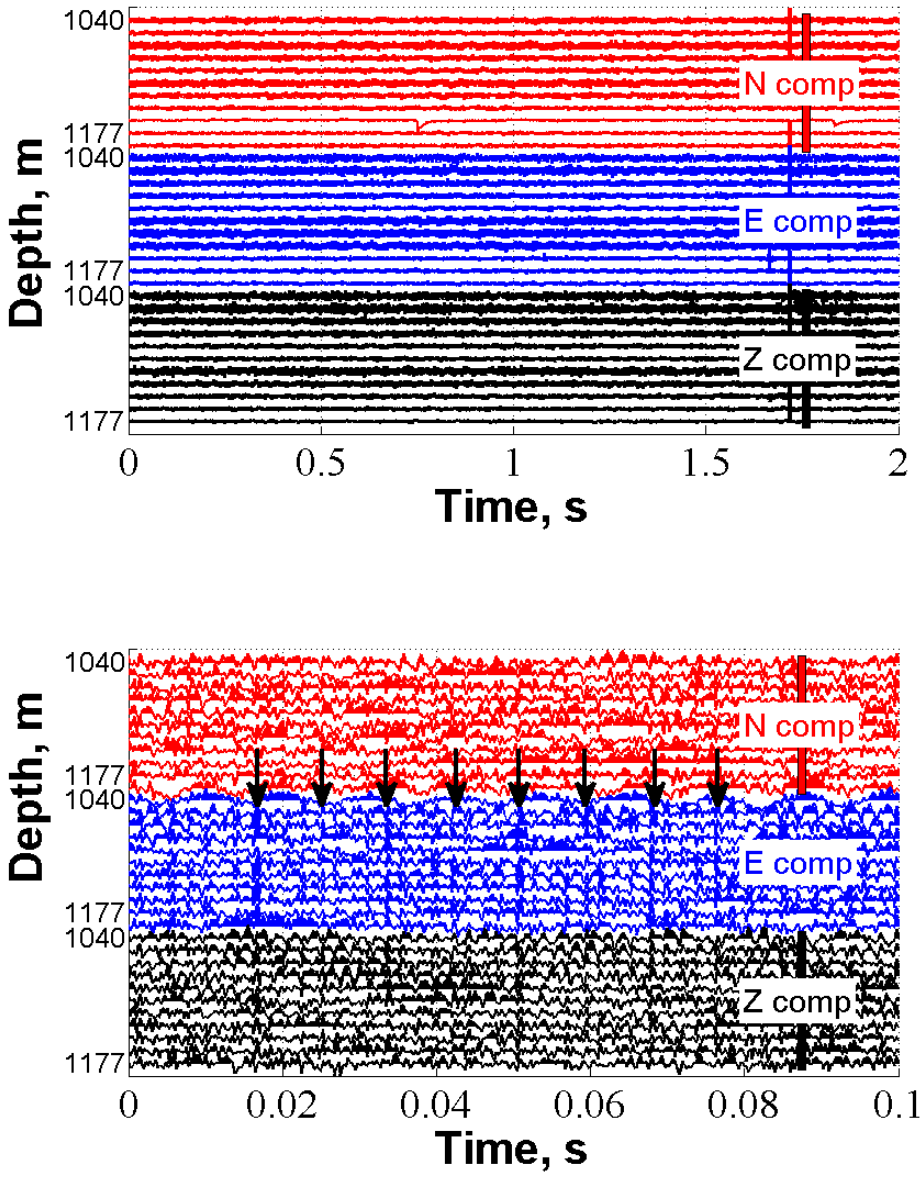

Figure 3.10 - A 2 s seismic data plot (upper) and the first 0.1 s from this plot (lower) from the second dataset. The data sampling rate is 0.25 ms. There is a repeated time aligned event recorded on a number of traces, as indicated by the arrows.

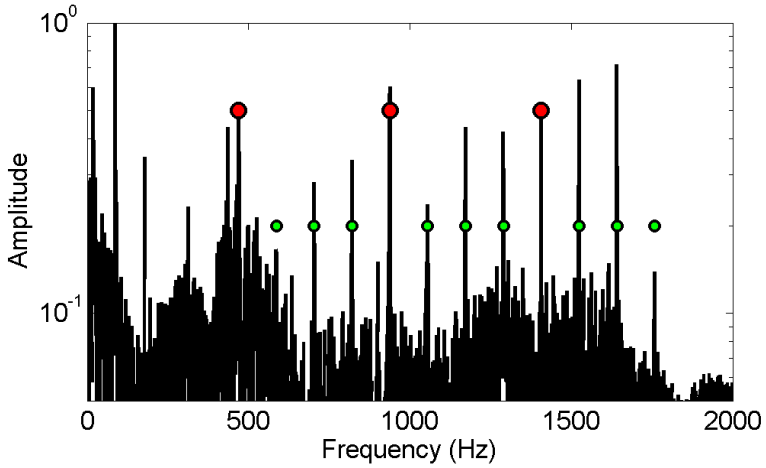

Figure 3.11 – The frequency amplitude spectrum from the first few minutes of the second dataset. The lowest frequency in the comb-spectrum under the first red dot occurs at 468 Hz. The green dots are equidistant between the red dots and ¼ incremental multiples of 468 Hz. All highlighted frequencies are predicted by the acoustic transfer matrix. The noise floor is at about 0.001.

Figure 3.14 shows a histogram of the differences between the raw detected spectra shown in Figure 3.12 and the median of these values shown in Figure 3.13. The central peak in the histogram contains just over 200,000 data points that are within 0.35 Hz of the median value. This was computed using 2 s windows for the 25 traces in Figure 3.8 for the 4.5 hours of recording. Only ~ 330 values varied greater than 0.35 Hz from the median value for the 25 traces. A time window of 2 s was chosen as a balance to minimize computation speed, provide a frequency resolution equivalent to 0.5 Hz and to avoid smearing a quick rate of change in the detected frequencies.

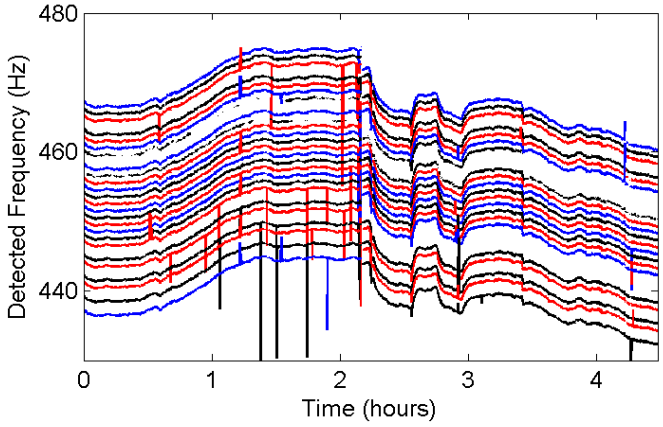

Figure 3.12 – The frequency amplitude spectrum for the lowest frequency in the comb-spectrum for 25 of 33 geophones from the second dataset. The 8 datasets not plotted were noisier. Each trace is offset 1 Hz from the shallowest geophone. Note the consistency.

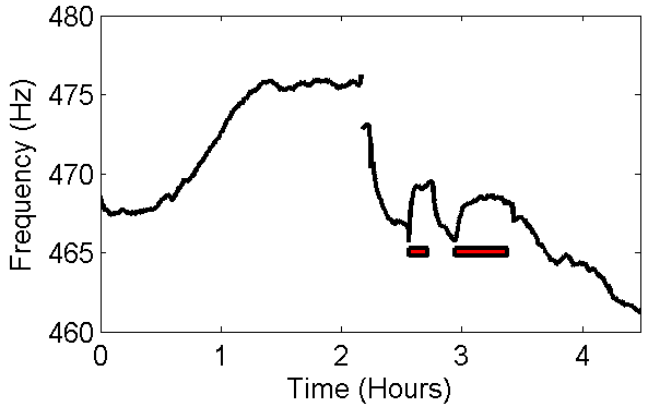

Figure 3.13 – The detected fundamental vibration frequency for the Alberta hydraulic fracture monitoring program. Equation (3.2) would predict the initial frequency of 467 Hz with a corresponding steel velocity of 5780 m/s, as the geophones are 12.37 m apart in the borehole. Figure 3.3 is representative of the line spectra except the areas with the horizontal bars which are represented by Figure 3.10.

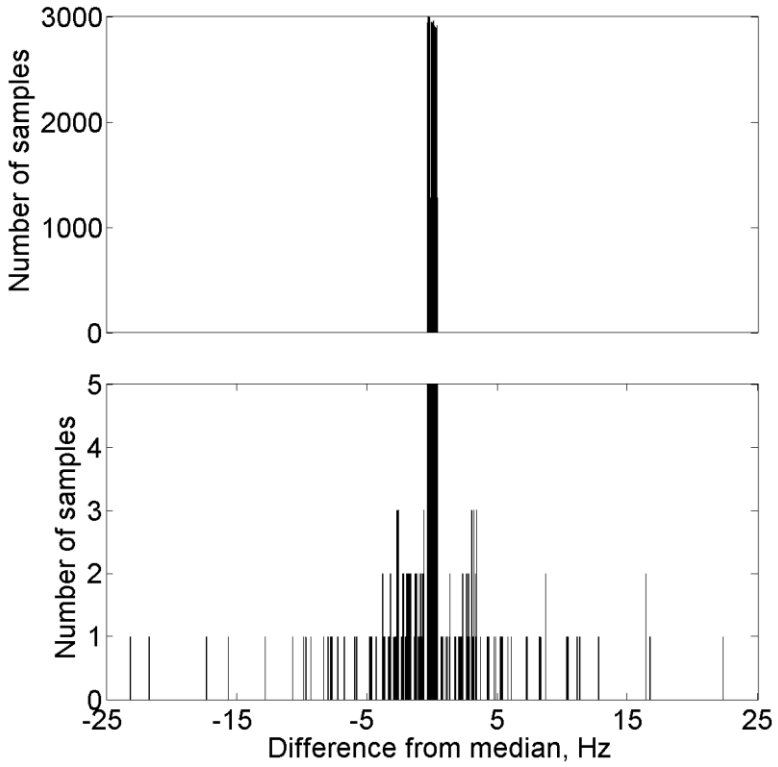

Figure 3.14 – Histogram of the differences between the individual detected frequency values in Figure 3.12 and the median of those values (Figure 3.13) for 25 of 33 geophones from the second dataset. The bottom plot is a 600X zoom of the top plot for histogram values between 0 and 5. There is consistency in the data measurement; only ~ 330 values out of ~ 200,000 deviated greater than 0.35 Hz from the median. The data values were detected in 2 s non-overlapping trace increments and were binned in 0.15 Hz intervals.

Most of the frequency amplitude spectra for the second dataset are similar to Figure 3.11. However, the comb-spectrum frequency amplitudes between 2 ½ and 3 ½ hours (as shown by the red bar in Figure 3.13) have the appearance of the spectra shown in Figure

3.15. The original comb-filter spectra remain, but their relative peak amplitudes have been altered, and there are new local peaks equidistance between the original comb-filter spectra.

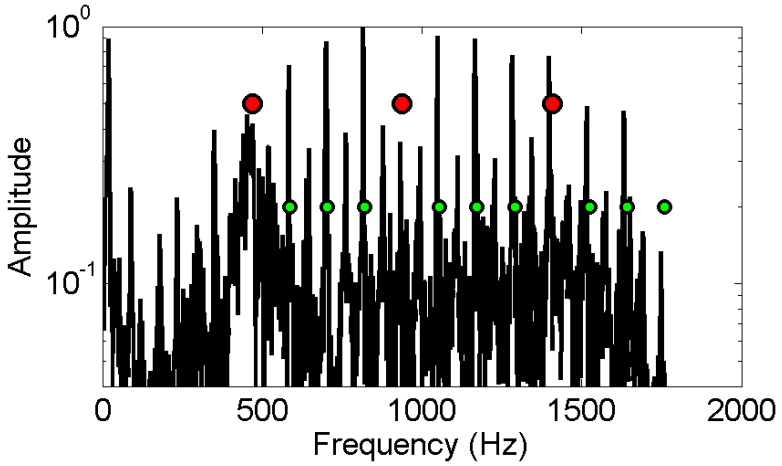

Figure 3.15 – The frequency amplitude spectrum for the times indicated by the red lines in Figure 3.13. During this time, line spectra occur between the comb spectra in Figure 3.11.

Figure 3.11 shows the temporal variation of the fundamental comb-spectrum frequency for the dataset along with a plot of the surface treatment pressure as a function of time (the downhole pressure data were unavailable for this analysis). The peak pressures for the ten treatment stages that were monitored appear to correlate with the frequency variations.

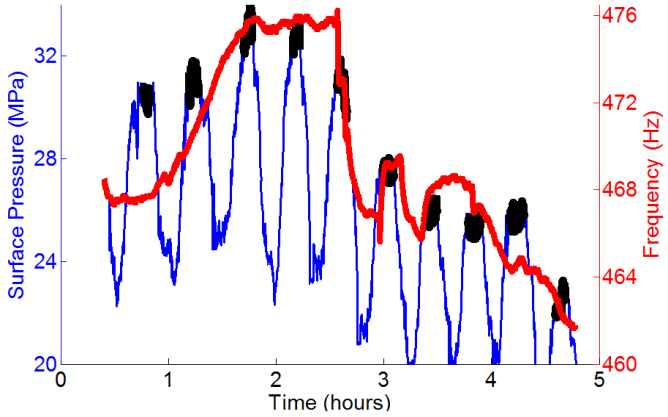

Figure 3.16 – The temporal variation for the first frequency in the comb spectrum for dataset 2 (red curve). Equation (3.2) predicts a fundamental frequency of 467 Hz based on a steel velocity of 5780 m/s and geophone separation of 12.37. The pressure for the 10 stages is plotted in blue. The pressures prior to breakdown are shown in black.

Although some details differ, the characteristics of both datasets are generally similar. Among the basic similarities is the comb-spectrum that persists throughout the duration of the recordings, independent of the occurrence of any other signal or noise. The comb-spectrum comprises a distinctive series of discrete narrow pass bands made up of frequencies that are 5/4, 6/4, 7/4, etc. of the lowest-frequency component. The comb-spectrum frequencies vary with the geophone spacing in a predictable manner. The amplitude ratios for the individual elements of this series do not appreciably change as a function of time. Finally, as elaborated below, the fundamental comb-spectrum frequency varies as a function of time, accompanied by proportional variations in higher frequency components. No other frequencies (such as 60 Hz electrical noise) exhibit this scaling behavior.

Different frequencies in the comb-spectrum are very strongly correlated. Figures 3.17 and 3.18 are crossplots of some of the frequencies in the comb-spectrum from the second dataset. Six frequencies in the comb-spectrum were estimated for the duration of the treatment in windows that were 2 s in length. The fundamental comb-spectrum frequency and five higher modes (specifically the 8/4, 10/4, 12/4, 13/4, and 14/4 peaks) were estimated from 25 traces for the duration of the treatment. The higher frequencies were crossplotted with the lowest frequency in the comb-spectrum. The results show that any one frequency in the comb-spectrum predicts the remainder of the comb-spectrum.

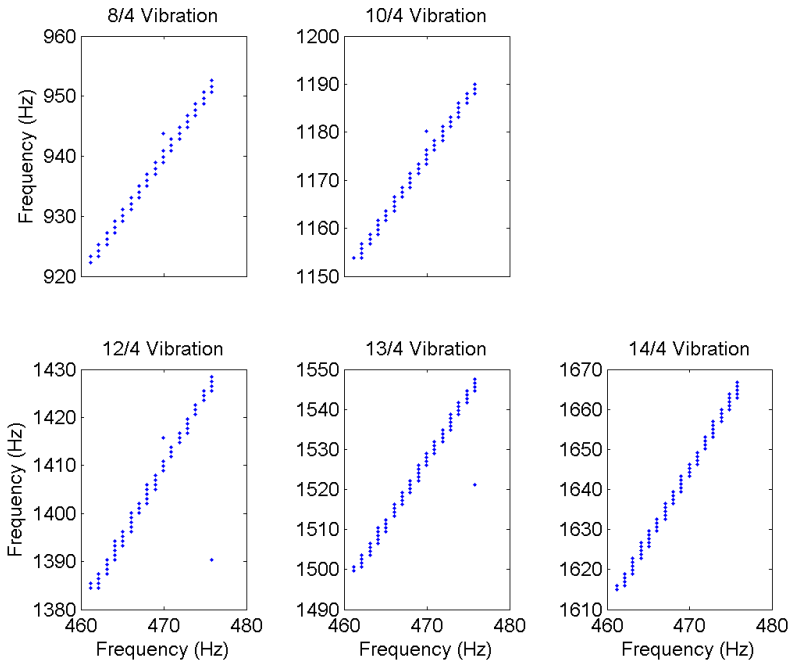

Figure 3.17 - Crossplots showing a high cross-correlation for the five detected fundamental frequencies versus the first resonance in the comb. Before the crossplots, a 5 point median filter was applied to all datasets. There are about 16,000 values in each crossplot. The steps in the plots are caused by the frequency steps in the FFT.

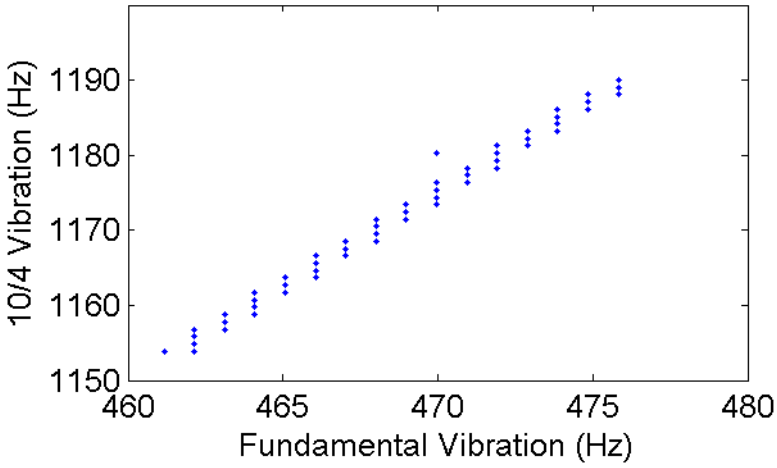

Figure 3.18 – A larger plot of the 10/4 versus the fundamental vibration crossplot from Figure 3.12.

Both Figures 3.19 and 3.20 show amplitude ratios for a number of specific frequencies in the comb-spectrum. The amplitude ratios are consistent for the duration of the monitoring, except as shown by the red area in Figure 3.13. This feature is discussed below.

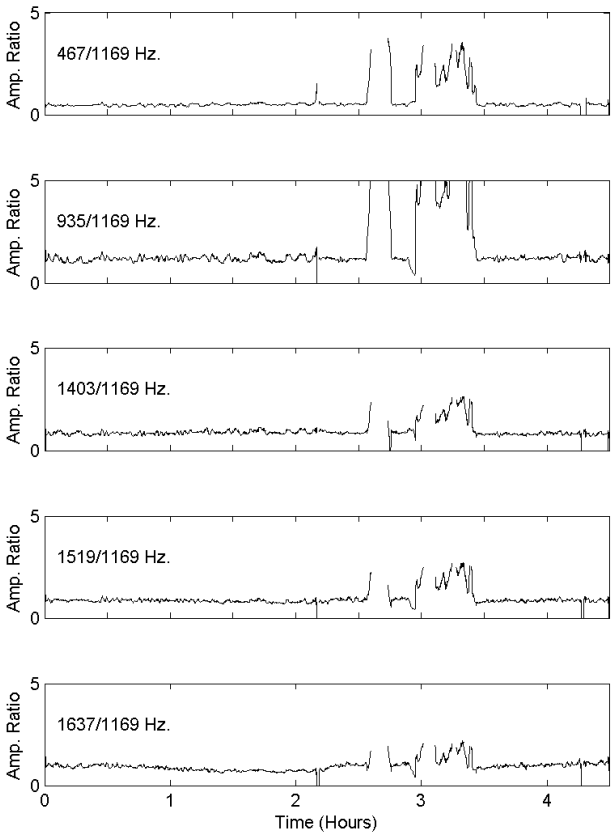

Figure 3.19 - Five amplitude ratios for the 4/4, 8/4, 12/4, 13/4 and 14/4 overtones compared to the 10/4 overtone. All of the amplitude ratios are consistent in amplitude except for the area denoted in red on Figure 3.13, where the frequency amplitude spectrum changed from Figure 3.11 to Figure 3.15.

Figure 3.21 shows another pertinent observation for the comb spectrum. This plot shows the detail for the 8/4 frequency in dataset 2 at three different times in the monitoring. The individual frequencies in the comb-spectra occur over a defined bandwidth. This bandwidth is consistent with the observations of Drumheller (1989) and Lous et al. (1998).

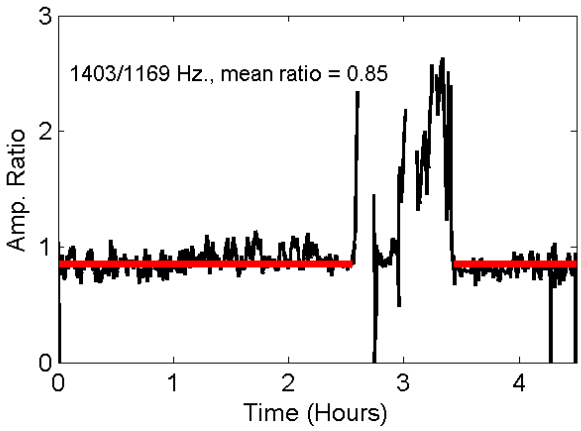

Figure 3.20 – An expanded view of the 12/4 and the 10/4 Hz amplitude ratio from Figure 3.19.

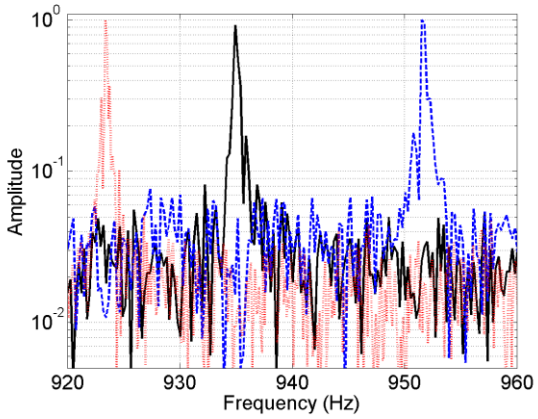

Figure 3.21 – The comb-frequency for the 8/4 frequency at early middle and late times during the hydraulic fracture treatment. Within the limits of the Fourier transform, there is fine detail in the comb frequency. Also, the individual comb-spectrum frequencies occur over a defined bandwidth. The frequency variations are similar to a variable length Helmholtz resonator (see Selamet et al., 1995 or Mason, 1927).

3.5 **Discussion**

Based on continuous deep borehole recordings obtained during passive seismic monitoring of several hydraulic fracture treatments, this study documents robust observations of distinctive, comb-like spectra. The comb-spectra are the results of a time-varying borehole acoustic transmissivity frequency filter. The comb-spectra persist over the duration of the treatment programs, including both active and quiescent monitoring intervals, and are characterized by a series of discrete, narrow transmission bands. The frequencies of the pass bands depend upon geophone separation forming a spectral pattern that is predicted, to very high accuracy, using an ATM approach developed to investigate signal transmission along drill pipes. The ATM formalism incorporates parameters that include the P-wave velocity of steel and the length of pipe segments and tool joints, denoted by L and W, respectively.

In the model preferred here, L represents the separation between clamped geophones, whereas W represents the effective length of clamping-induced stress concentration at the casing. The W value is not a physical length; it is a proxy for the effective length of stress concentration associated with borehole-geophone clamp interface. This area of concentration is a function of the effective stress at this interface and is, by extension, a function of the external confining stress on the borehole. As shown in Figure 3.22, a change in external stress, changes the relative clamping force of the sonde, changing the effective restriction width W.

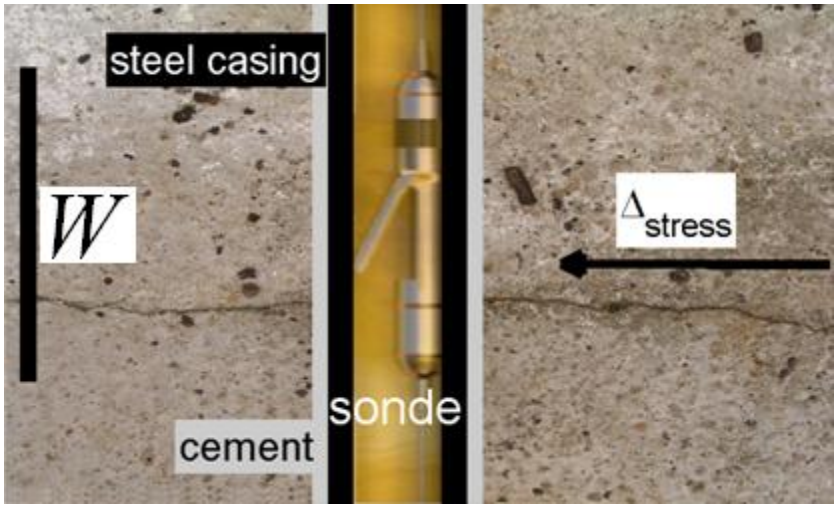

Figure 3.22 – Conceptual model relating geophone-clamping mechanism to changes in external pressure. When stress changes impinge on the observation wellbore as indicated by the arrow, the geophone clamp spring reacts, changing the effective length (*W*) of stress concentration associated with borehole-geophone clamp interface.

3.5.1 Alternative models

A number of alternative models for the comb spectra have been considered, but are considered unlikely because they do not adequately explain the observations. Alternative models include:

1. *Noise from surface pump jacks, transmitted to the geophones along the casing of the monitor wellbore:* observations of pump-jack noise from a well in the area show that these resonances begin at 7.75 Hz and continue in almost integer multiples to 99 Hz as shown in Figure 3.23. These frequencies are lower than the comb spectra presented here and are consistent with the observations of Forgues et al., (2011), and Marfurt et al. (1996).

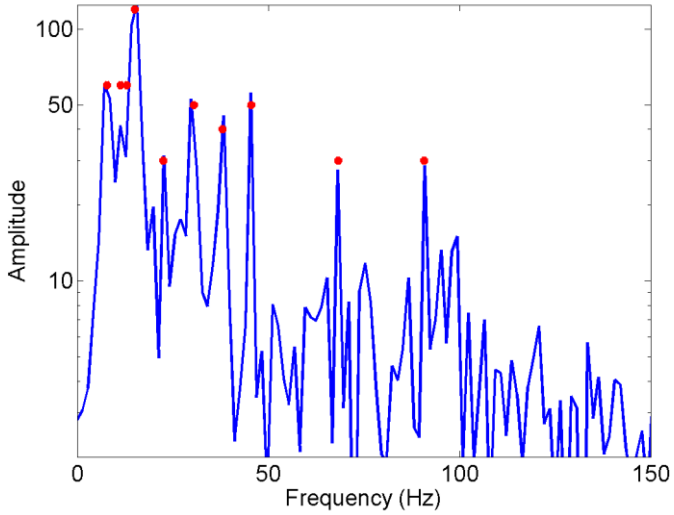

Figure 3.23 –Pump jack vibration from a nearby surface pump jack. These data were recorded with a geophone placed on the pumpjack cement base. The vibration begins at 7.75 Hz and continues in almost integer multiples up to 99 Hz. These frequencies are lower than the acoustic transmissivity frequencies.

2. *Pump and engine vibrations associated with the hydraulic treatment itself:* Abdel-Rahman and El-Shaikh (2009) discuss manifestations of pump vibration and their results show little correlation with the data shown here.

3. *Spurious resonances of the geophone sondes (Figure 3.24)*: although these resonances are known to exist (Faber and Maxwell, 1997) they do not explain the observed dependence of the spectral response on the geophone separation, or the observed temporal variations.

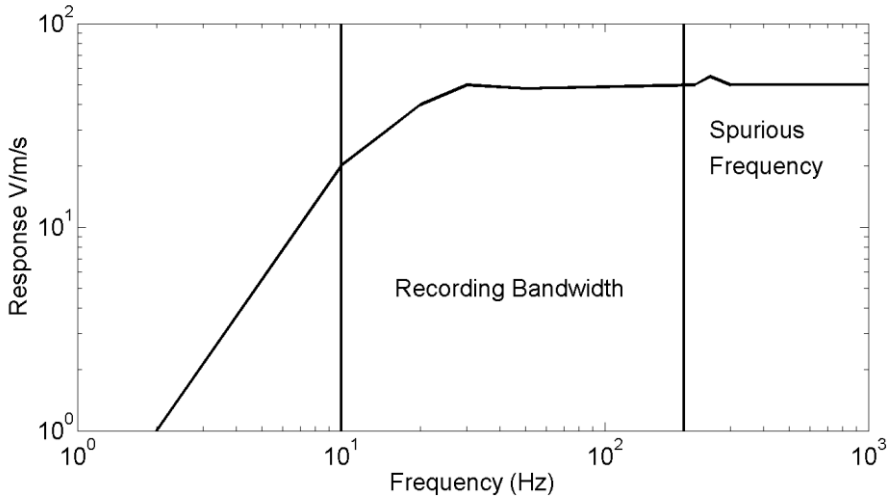

Figure 3.24 –A frequency amplitude plot of a spurious frequency in a geophone response curve (from Faber and Maxwell, 1997).

4. *Changes in fluid level or pressure due to ingress of fluids into the monitor well:* the fluid level was monitored in both datasets and no change in the fluid level was observed. Both of the monitoring wellbores were suspended low-productivity oil wells. Prior to the microseismic monitoring, the wells had removable inflatable packers placed at the bottom of the hole to isolate the perforations from the geophone array.

5. *The variations in the comb-spectra are due to lack of frequency resolution in the FFT*: The shortest analysis window was one second long, resulting in a frequency resolution of 1 Hz. The choice of window length for the FFT was chosen to be a balance between the frequency resolution determined by the FFT window length, the rate of change for the comb-spectrum frequencies, and the computation time required to analyze the data.

A one second window length provides a resolution of 1 Hz at 0.00025 ms sampling rate. The fastest rate of change for the fundamental frequency in the comb spectrum was 0.2 Hz/s (on the NEBC dataset). However, the average rate of change for the fundamental frequency in the comb spectrum was much greater than 1 Hz/s. For most of the data, the variations in the comb-spectra could not be due to the lack of frequency resolution in the FFT.

6. *The wireline cable supporting the geophone array was in tension, and noise propagated along the cable.* The geophones were supported by a cable under high tension. However, the apparent velocity of the phenomenon across the array was infinite, as can be seen in Figure 3.10 (lower). Noise along the supporting cable would have to have a realizable velocity.
7. *The geophone clamping mechanism is the source of the phenomenon, not the acoustic transmission along the pipe.* Both datasets presented here were recorded with geophone arrays manufactured by Avalon Sciences Ltd. Six other datasets were examined for evidence of comb-spectra, but no evidence was found. A possible explanation for these geophones arrays to create this phenomenon is the clamping mechanism. The sondes are clamped as shown in Figure 3.22 (the artwork for the sonde in the figure was provided by Avalon). The clamping mechanism may have a spring constant that results in a change of the resonance for the individual geophones. However, Lindsay and White (1934) experimented with different spring constants for weights attached with springs to steel rods to show transmissivity changes for waves travelling along the rod.

3.5.2 Physical model

A 1.8 m long 19 mm diameter domestic copper plumbing pipe was used as a physical model to test vibration frequency for an unbounded cylinder as a function of pressure. An oblique view of the pipe is shown in Figure 3.25. The pipe had an end cap soldered at one end and a valve soldered to the other end. The pipe ends were supported by a simple string to allow free movement of the pipe. An air compressor pressurized the pipe to pressures up to 827 kPa. A hammer struck the pipe at different pressures. A microphone was used to record the change in vibration as the pipe was pressurized and depressurized twice. Figure 3.26 shows the change in a double resonant vibration near 1430 Hz for one of the four trials. Figure 3.27 shows that the resonant frequencies crossplotted as a function of pressure. There was an observed decrease of 0.288 % per MPa of air pressure increase. Although the resonant vibrations changed as a function of pressure, the change was not large enough to explain the phenomenon observed here.

Figure 3.25 – A photograph of the 1.8 m long copper pipe that was suspended by a rope and pressurized with air to pressures up to 827 kPa.

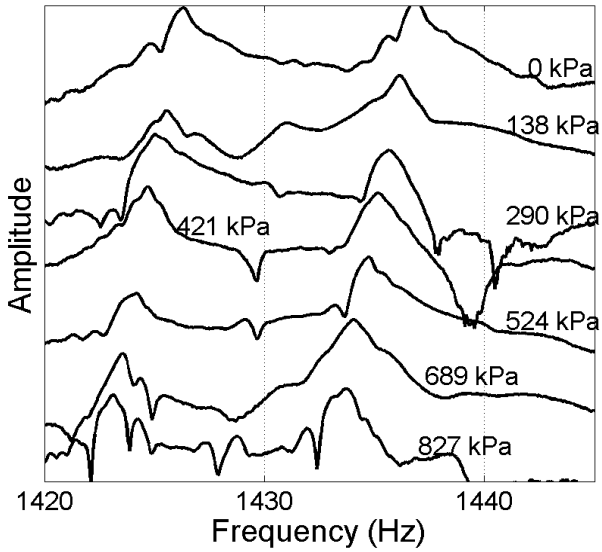

Figure 3.26 – Frequency amplitude plots for two local peaks at seven pipe pressures using the pipe shown in Figure 3.17. As the pressure decreased, the resonant frequency of the pipe decreased.

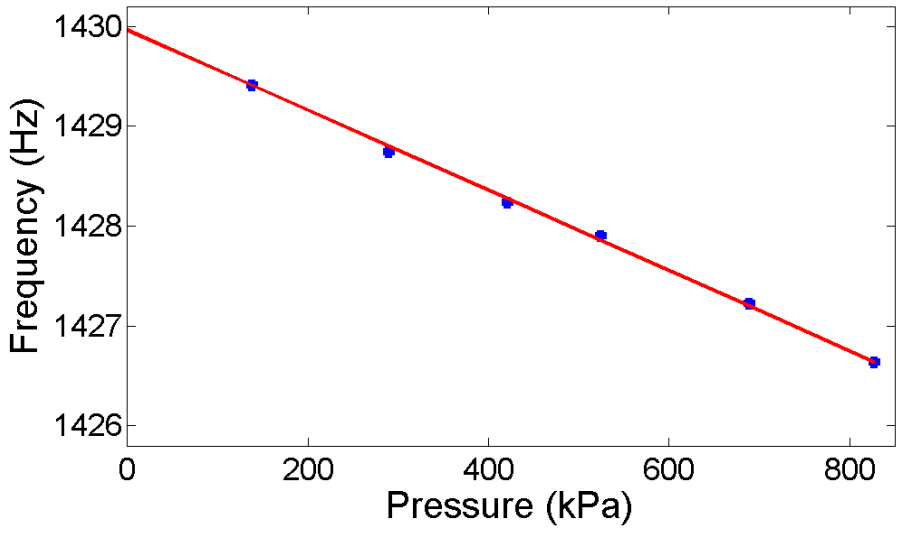

Figure 3.27 – A crossplot of the first local peak in Figure 3.18 versus pressure. As the pressure decreased, the resonant frequency of the pipe decreased.

3.5.3 COMSOL model

COMSOL was used to simulate a hollow steel cylinder encased in concrete with diameters equivalent to that for the casing used in the two datasets (inner casing diameter = 0.1 m, outer casing diameter = 0.117 m). The cylinder was 1 m long (to reduce the number of modeled elements). The steel pipe was fixed at both ends of the pipe. An internal acoustic source was used to excite the steel, and a number of eigenfrequencies were examined for resonances. One resulting resonance is shown in Figure 3.28. As the external pressure on the pipe was increased, the resonant vibration of the pipe was reduced as shown in Figure 3.21. Similar to the physical model, these frequencies were not equivalent to the results observed on the datasets.

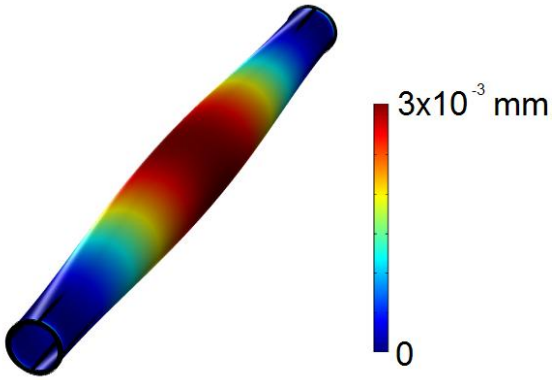

Figure 3.28 – A plot showing the steel pipe movement for one of the COMSOL calculated eigenfrequencies.

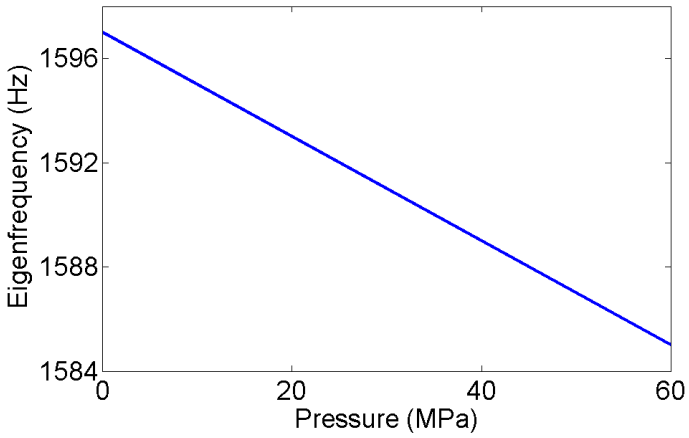

Figure 3.29 - As the external pressure on the pipe in Figure 3.20 was increased, the COMSOL calculated resonant vibration of the pipe was reduced.

The apparent correlation between changes in treatment pressure and changes in fundamental frequency of comb spectra (Figures 3.8 and 3.16) suggests a possible causal relationship. The correlation is investigated further in Figures 3.30a and 3.31a, which show linear relationships (the coefficient of determinations are R^2 = 0.83 and 0.71, respectively) between the fundamental comb frequency and treatment pressure for datasets 1 and 2.

The crossplot in Figure 3.30 is only for the downhole pressures before initiation of the hydraulic fracture treatment into the formation (refer to Figure 3.8). After fractures were initiated, there was much less correlation between the downhole pressure and the recorded comb-spectrum frequencies. This may have been due changes in stress conditions at the observation borehole by the fracture propagations at the horizontal wellbore.

The crossplot in Figure 3.30 is only for the surface pressures shown in black on Figure 3.16 (the downhole pressures were unavailable for this study). Only the peak pressures were used in the crossplot because it was felt that it would be these pressures that would dominate the downhole stress regime.

For comparison, the corresponding change in effective length of clamping-induced stress concentration (W) required to reproduce the observed range of frequencies as calculated by (3.2) and (3.3) and confirmed with COMSOL models is shown in Figures 3.30b and 3.31b. While this comparison should not be viewed as a calibration of the frequency-stress response of the clamped geophone arrays, it does provide a testable model prediction that can be evaluated in future studies.

The only change in the model required to model to reproduce the observations is the change in the effective clamping width W. If the geophone distance L or the velocity of the compression wave is changed, the model results will not match the observations.

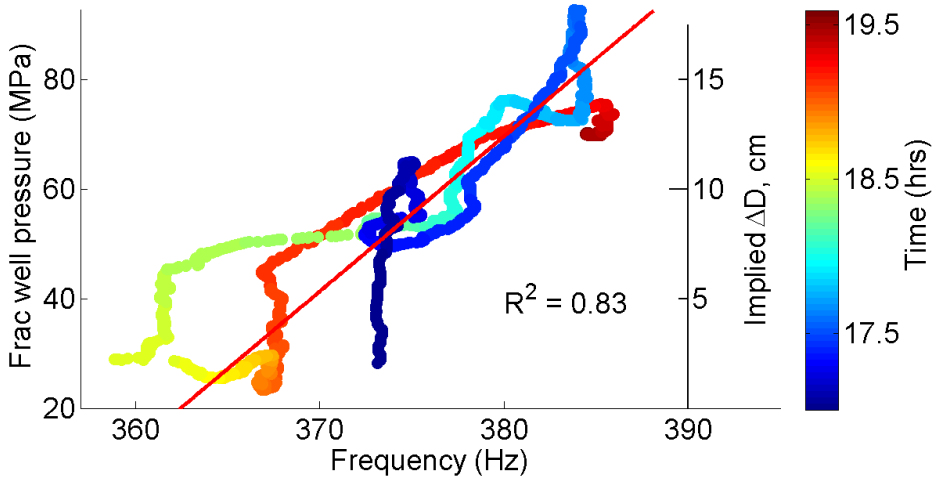

(a)

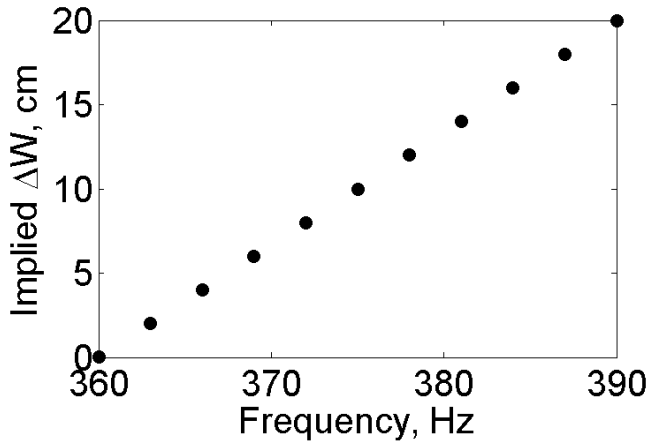

(b)

Figure 3.30a and b – Crossplot of the vibration frequencies vs. the treatment well downhole pressure from Figure 3.6 between 17:00 and 19:48 hours for dataset 1. The least squares best fit line has a coefficient of determination given by R^2 = 0.83. The implied change in clamping width ΔW from (3.2) as a function of the lowest comb-spectrum frequency is shown below.

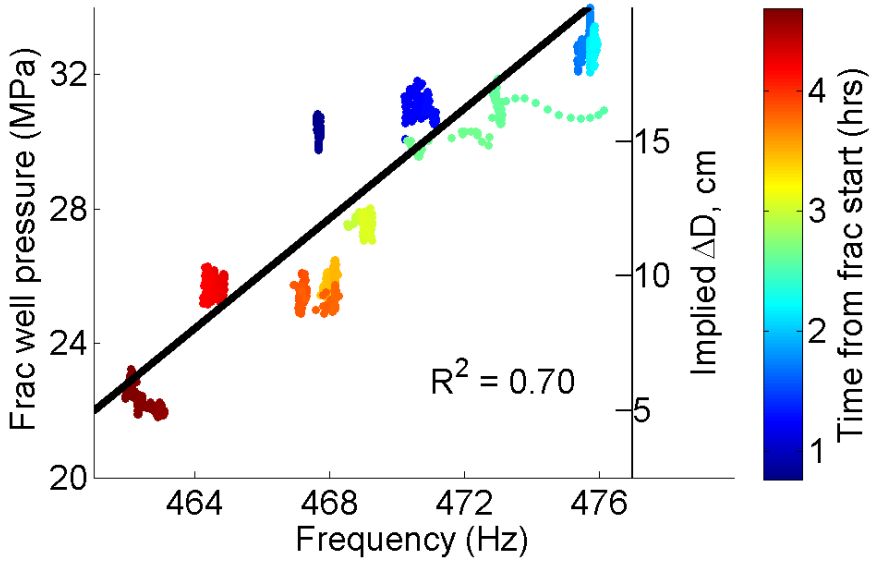

(a)

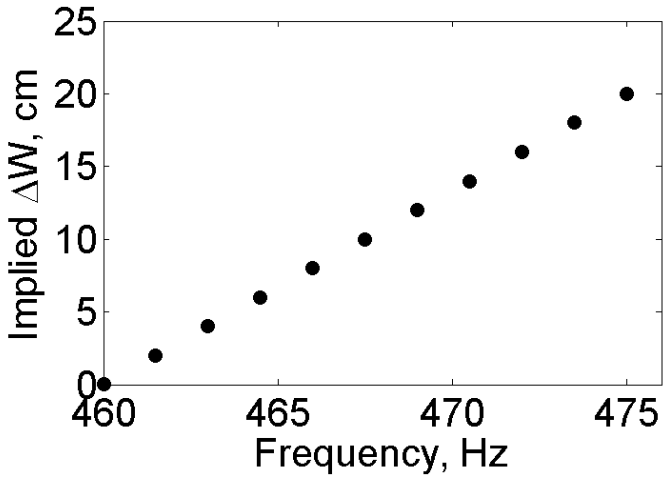

(b)

Figure 3.31 a and b – Crossplot of the vibration frequencies vs. the treatment well downhole pressures indicated in black on Figure 3.11. The least squares best fit line in red has a coefficient of determination given by R^2 = 0.71. The implied change in clamping width ΔW from (3.2) as a function of the lowest comb-spectrum frequency is shown below.

There are a few other potential applications of the borehole acoustic transmissivity phenomenon other than those presented here. Consider Figure 3.8. The frequencies in the comb spectrum changed markedly after the initiation of the fracture treatment. This was also observed on the five other stages in the dataset but not presented here. This change can be used as a confirmation that the hydraulic fracture treatment is changing the stress field at the monitoring wellbore. However, currently, this is an uncalibrated observation.

It is unknown why a portion of the comb-spectra from dataset 2 have the appearance of Figure 3.15. This change occurred after the recording of the LPLD event discussed in Chapter 5. The addition frequency spike in the comb-spectra could be explained by a torsion wave travelling along the borehole at ½ the velocity of the compression wave. However, these observed comb-spectra require further investigation.

Carcione and Poletto (2000) discuss borehole acoustic transmissivity passbands similar to those observed here as the characteristic acoustic response for a drill string array. The same analogy can be made here. The passbands plotted in Figures 3.6 or 3.11 can be considered to be the characteristic acoustic response for waves travelling within the casing. This consideration defines a potential benefit of the borehole acoustic transmissivity phenomenon is the natural filtering of noise propagating within the borehole. If Lamb waves were generated and transmitted in the casing, as discussed in Chapter 2, the effect of the geophone array would be to filter this wave travelling along the steel pipe. The array should not affect the recording of P- and/or S-waves directly arriving at the geophones.

A requirement for calibration of the borehole acoustic transmissivity phenomenon is either direct measurement of stress in the monitor wellbore, or calculation of stress changes at the geophone array caused by the fracture treatment project. Although a complete geomechanical model is beyond the scope of the present study, Figure 3.32 shows an approximation based on the far-field perturbation to hydrostatic stress due to a crack formed under tension (Lawn and Wilshaw, 1975), which is equivalent to the external stress changes from a tensile crack opening due to internal fluid pressure (Walter and Brune, 1993). This calculation considers the stress field associated with the tip of a crack with a half-length of 100 m, and models the perturbation to hydrostatic stress as the mean isotropic component of the crack-tip induced stress tensor. Figure 3.32 shows that pressure changes caused by a crack tip that is 200 – 800 m from the geophone array are about 30-72% of the fluid pressure within the tensile crack. This represents a significant fraction of the fluid pressure and provides support for the observed correlations in Figures 3.30a and 3.31a.

The far-field pressure perturbation in Figure 3.32 shows that hydraulic fracturing could be changing the hydrostatic stress at a monitoring wellbore. If this stress changes the effective clamping force of ~1000 pounds for each of the geophones in the equidistantly spaced geophone array, it would change the impedance contrast at the geophone locations. The changes modelled using (3.3) and shown in Figures 3.30b and 3.31b show that these relatively changes can be modelled by using a clamp width as a proxy for the impedance contrast change caused by the relative clamping force change.

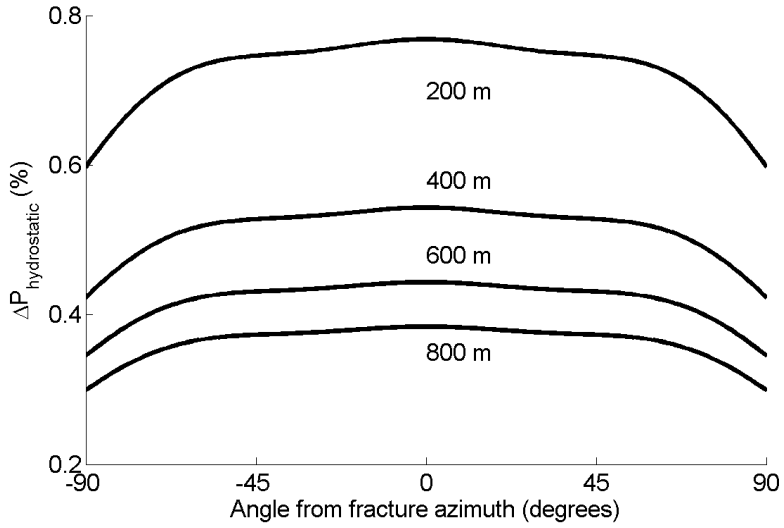

Figure 3.32 - The calculated far-field perturbation to hydrostatic stress due to a tensile crack of half-length 100 m. A relative hydrostatic pressure value of 0.5 means that the perturbation is 50% of the internal fluid pressure in the crack.

3.6 **Conclusions**

Microseismic data recorded during passive seismic monitoring of two multistage hydraulic fracture treatment programs in western Canada show distinctive comb spectra that exhibit distinct temporal changes. The frequency characteristics of the comb-spectra match those predicted using an acoustic transfer matrix approach developed to investigate signal transmission in drill strings. The fundamental and higher passband modes depend upon the geophone spacing, implying that they cannot be modelled as an instrument resonance phenomenon. In the cases considered here, the fundamental frequency exhibits variations throughout the monitoring. I interpret the cause of these variations as relative changes in geophone clamping force, in response to changes in *in-situ* stress conditions.

Perhaps the most important implication of this work is that the proposed model implies that potential exists to use variations in comb spectrum during a hydraulic fracture treatment to monitor *in-situ* stress variations, which could be of considerable value as a novel tool for passive seismic monitoring of reservoir conditions.

Chapter Four: P-wave path effects in microseismic data recorded in a deep wellbore

4.1 **Summary**

Microseismic data recorded during a hydraulic-fracture treatment in western Canada included 20 high signal to noise ratio (S/N) events over a two-hour time period. Seventeen of the 20 events were grouped into four clusters based upon event cross-correlation analysis. Spectral analysis of the P-wave arrivals shows variation in signal between different sets of events, especially within the 280 to 320 Hz and 440 to 540 Hz frequency ranges. A 2-D elastic finite-difference simulation using simple layered model based on sonic logs shows that this variation may be due to path effects associated with propagation of the signal from the source to the receivers, including wide-angle multiple reflections and head waves. Beyond recognizing their influence on recorded signals, path effects could be used to reveal a more complete model of the rock geometry at the hydraulic fracture level and to group events from the same spatial region and/or depth. A spectral ratio method is presented that may lead to a semi-automated scheme to group events.

4.2 **Introduction**

Path effects represent modifications to waveform amplitude and phase that occur due to wave propagation within a heterogeneous medium (Hogan and Eaton, 2012). The physical processes for the recording of a seismic wave generated at a source and

transmitted through media to be sampled some distance away can be summarized as the convolution of the source, receiver and path effect (Yilmaz, 2001), as shown by (4.1):

$$d(t) = s(t) * r(t) * p(t) + n(t), \tag{4.1}$$

where $d(t)$ = recorded data, $s(t)$ = source function, $r(t)$ = receiver impulse response, $p(t)$ = path effects, $n(t)$ = random noise and t = time.

Equation (4.1) can be used to describe active or passive data sampled by a seismic recording system. Consider a source some distance away from a geophone. The source will have a radiation pattern defined by the source mechanism (Shabelansky et al., 2012). Although the recording system and sampling process can produce distortions (Scherbaum, 1994), within the bandwidth considered here these effects are relatively minor. A characteristic impulse response is used here to represent the response of the recording system.

Path effects are defined in this thesis as shown in Figures 4.1 and 4.2. All other effects on the amplitude of the energy travelling from the source to the receiver are defined as path effects. There are a number of reasons for path effects in microseismic data, as shown in Figure 4.2. There can be multiply reflected energy, mode converted energy, ghosting, head waves and other phenomena that result in the decrease or amplifications of frequencies or changes in phase as a wave travels from its` source position to a recording location. Moreover, path length and bed thickness can lead to destructive and constructive interference phenomena, particularly for a wave guide associated with a low-velocity layer. Graves and Clayton (1992) remark that it is usually more difficult to obtain the path effect description than the source or receiver function.

Their remark was intended for waves travelling obliquely through media, but a similar inference applies for waves travelling subparallel to bedding (Hogan and Eaton, 2012).

With reference to Figure 4.2, seismic attenuation can be defined by:

$$S(f) = S_0(f)\, e^{-\alpha z} \tag{4.2}$$

where $S(f)$ = amplitude of frequency after propagating a distance Z, S_0 = initial amplitude spectrum, f = frequency in Hz, z = propagation distance in m, $\alpha = \pi f/QV$, where Q = quality factor, a dimensionless unit used to estimate frequency dependent amplitude loss (Aki and Richards, 2002) and V = phase velocity of the wave in the medium, m/s.

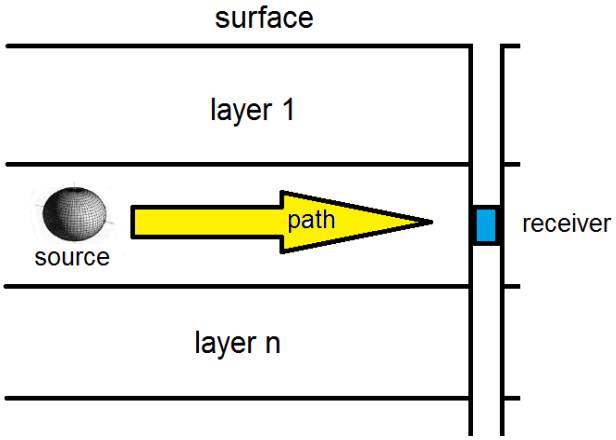

Figure 4.1 – A simple cross-section through layered media showing a subsurface source that generates a wavefield that is sampled by a borehole geophone. The layers can be described by their elastic properties.

Path effects for downhole seismic monitoring differ fundamentally from path effects for surface seismic monitoring; in most cases, downhole microseismic recordings

consist of waves transmitted in a more-or-less horizontal direction, whereas surface microseismic data typically contain signals that propagate along nearly vertical paths. For the case of relatively layered sedimentary strata, downhole microseismic observations record waves that propagate approximately parallel to the layering. Consequently, there is a tendency for multi-path arrivals to scatter from interfaces at post-critical incidence angles of incidence. Previous acoustic modeling studies show that this propagation geometry highly oblique to layering may lead to more pronounced path effects (Hogan and Eaton, 2012, Lines et al., 1992 or Greenhalgh et al., 2007).

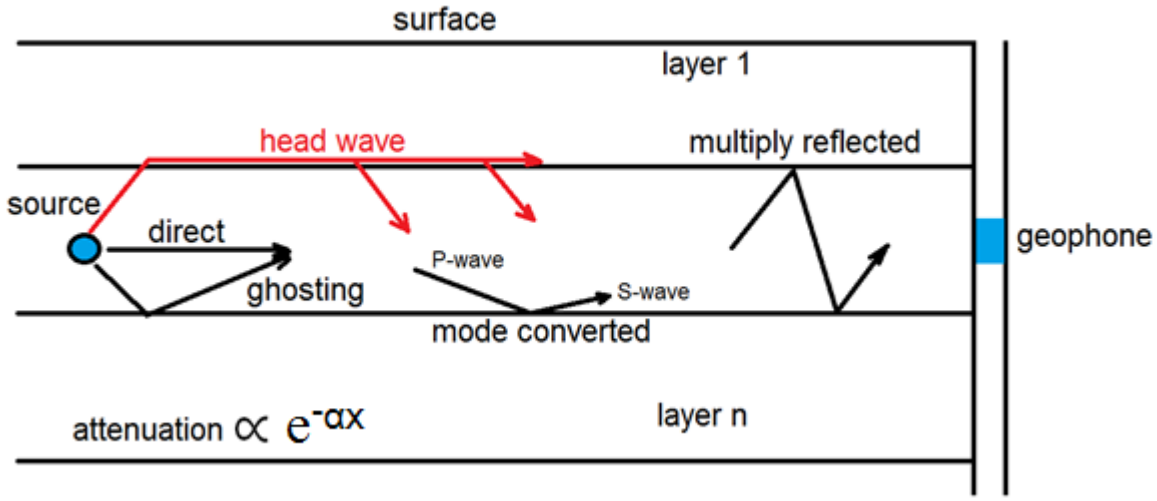

Figure 4.2 – A number of possible path effects for microseismic data recorded by a geophone at depth. Multiply reflected energy, attenuation, mode converted energy, ghosting and head waves call change the character of the source wavelet.

Earthquake seismologists have long recognized and distinguished between path, source and recording site effects. Lermo and Chavez-Garcia (1993) used single-station spectral ratios of S to P waves to estimate site-recording effects. They examined how earthquake source spectra can be complicated by path propagation. Chen and Atkinson

(2002) separated source, path and site effects for a better estimate of source radiation. Graves and Clayton (1992) discuss path effects for earthquakes recorded in the Los Angeles, California area using numerical modeling. They found that path effects were influenced strongly by the source and receiver locations. These studies all show that during the propagation of waves from the source to a site, many changes in a waveform can occur. For example, multiple reflections can result in secondary signal phases, attenuation can cause frequency-dependent amplitude reduction and phase shifts, and reverberation in sedimentary layers can cause frequency-dependent amplification (Scherbaum, 1994).

Some path effect studies are based upon the analysis of clusters of individual events known as 'multiplets' (Kumano et al., 2007). Kokon and van der Baan (2012) define a microseismic doublet as a repetition of a microseismic event; they define a group of three or more events with nearly identical waveforms as a multiplet group. Microseismic data multiplet analysis assumes that waveform similarity can be used to define multiplet clusters. These clusters should contain events within close proximity to each other. Waveform similarity is related to similar focal mechanism and similar travel path (Kumano et al., 2007).

Some crosswell borehole tomography research has focused on layer-parallel path effects. Lines et al. (1992) examined channel waves in cross-borehole data and showed that they could be used to estimate thicknesses of inter-well wave guides. Liu et al. (1992) modeled channel waves in anisotropic coal seams. They used a finite-difference algorithm to model varying source and receiver positions within a coal-seam and noted that the frequency content of the vertical components of channel waves are especially

sensitive to off-centre source and receiver positions. Lou and Crampin (1993) examined guided waves in isotropic and crack-induced anisotropic layers. They noted that seismic waves in cracked layers may vary substantially for different crack orientations; they further surmised that guided waves may be used to monitor temporal changes in layered strata.

The increasing use of microseismic monitoring in recent years has stimulated research on phenomena similar to earthquake and crosswell tomography path effects. It has been demonstrated that reservoir rock heterogeneity can introduce pronounced changes in the characteristics of a wave travelling through a medium. For example, Greenhalgh et al. (2007) showed such waveform changes by finite-difference modeling of the seismic response of waves travelling in a low-velocity coal seam with faults and internal discontinuities such as brecciated zones. They found that the horizontal component of the particle displacement is confined more in thin coal seams that the vertical component. Teanby et al. (2003) measured shear-wave splitting to monitor time-dependent crack properties induced by pore pressure changes or stress using numerous microseismic events recorded in a borehole. They found that tidal loading of the Valhall oil field in the North Sea may be causing stress changes that correlated to shear wave splitting. Fagan (2012) performed frequency-domain clustering of similar microseismic events (multiplets) to identify spectral differences that were used to refine spatially organized subclusters of microseismic events based on subtle changes in frequency content. This approach is based on the premise that clusters of nearby events share a similar source-receiver propagation path and so are expected to exhibit similar path effects, whereas other events with a dissimilar path may not.

The focus of this work is to investigate path effects in microseismic monitoring, with potential application to inferring characteristics of the transmission media. In our experience, path effects are clearly expressed in microseismic waveform data and are readily observable during monitoring surveys acquired in deep wellbores. In this chapter, we present examples of path effects on P-wave arrivals generated by hydraulic fracturing and recorded during microseismic monitoring. This work is part of an on-going study to analyze P- and S- waves using elastic wave modelling as a continuation of previous acoustic wave modelling. We begin by presenting data from a microseismic dataset recorded in western Canada. Next, we build a one-dimensional geological model using sonic and density logs from the monitoring wellbore, as input to a finite-difference wave-equation modelling algorithm. We supplement these models with some simple finite-difference wave-equation models. The simulations reveal the nature of anticipated path effects for downhole microseismic data. Finally, we explore how the path effects can be used to enhance the interpretation of the microseismic data by refining source locations within the hydraulically fractured zone and grouping multiplet arrivals. These observations confirm a previous suggestion by Hogan and Eaton (2012) that path effects could potentially be used as a method for verification of source depth.

4.3 **Observations**

The data used for this study were acquired during borehole microseismic monitoring of a hydraulic fracture treatment for a horizontal well drilled in western Canada in 2010, as shown in Figure 4.3. A number of vertical wells on the map have been producing from the Cretaceous-aged reservoir zone for up to 30 years. Operators

are now drilling and completing hydraulically fractured horizontal wells in the area because of low primary oil and gas recovery from the vertical wellbores and recent higher commodity prices. Hydraulically fractured horizontal wells should have a higher ultimate oil recovery and better commercial viability than vertical wells (Holditch, 2006).

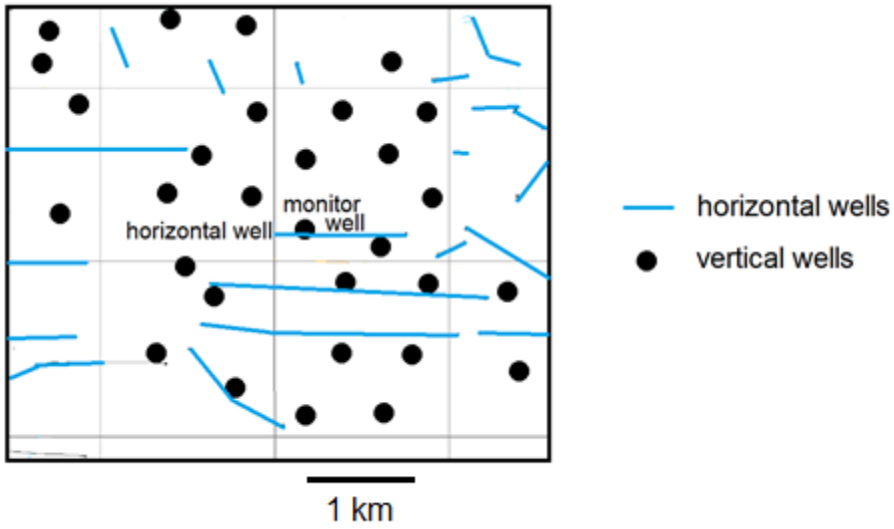

Figure 4.3 – A plan view of the central Alberta horizontal treatment well and vertical observation monitor well. The observation well is 50 m north of the horizontal well. All wells displayed have produced hydrocarbons from a Cretaceous zone at about 1300 m depth.

The producing zone is a late Cretaceous marine clastic unit deposited in central Alberta. In the study area, the average porosity is 10 % with an average permeability of 1 mD. The low permeability reservoir beds dip to the southwest at about 3 m/km and there are no known faults within 5 km of the observation wellbore as determined from 300 vertical wellbores extending outward from the vertical monitoring wellbore on Figure 4.3. Gently dipping beds with no apparent faulting support the use of the horizontal velocity model discussed below.

Microseismic data were recorded using an array of 12 three-component geophones in a monitoring wellbore 50 m north of the 1000 m long west to east horizontal wellbore, as shown in Figure 4.4. The monitor borehole was drilled to a depth of just over 1400 meters and was lined with steel casing and cemented to the surrounding strata. The sondes were clamped 12 m apart and recorded data at 0.25 ms sample rate. The data recorded on the horizontal geophones were oriented to north and east directions with rotations defined by hodograms from a five-station vibroseis checkshot survey. Microseismic events containing P- and S-wave arrivals are evident with frequencies up to 800 Hz.

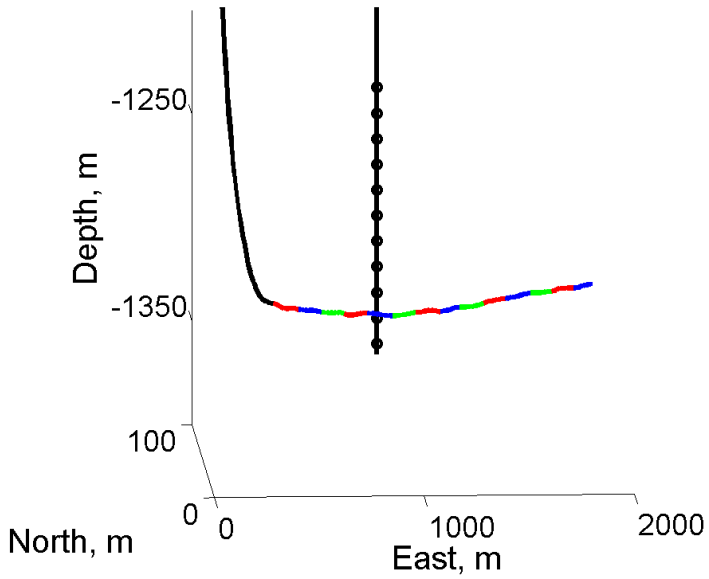

Figure 4.4 – A perspective view of the central Alberta horizontal treatment well and vertical observation well. All values are in meters. The observation well is only 50 m away from the horizontal well. The 14 hydraulic fracture stages are shown in colour.

The monitor wellbore is one of two vertical wellbores that were used to record microseismic events over 5 ½ hours from a 12-stage hydraulic fracture stimulation in the open-hole horizontal well. Each stage used approximately 100 m^3 of fluid and 25 tonnes of sand. Formation breakdown occurred for all stages between 22 and 33 MPa of surface pressure, possibly indicating areas of lower permeability, as discussed below. During initial processing of the data, 850 events were located. All but 150 events were located within the 20 m thick reservoir zone. Over 100 locations were up to 50 m above the reservoir zone; about 30 locations were up to 100 m below the reservoir zone. Moment magnitudes determined during initial processing ranged from -2.7 to -4.4. Calculated event distances ranged up to 700 m, but most were within 300 m of the sensor array. The contractor noted a relatively low noise level of about 700 nV for the geophone array.

Figure 4.5 shows a 0.3 s segment of data containing a representative example of a high S/N P- and S-wave event. Based on careful inspection of the dataset, 19 events similar to the event in Figure 4.3 were saved for this analysis. The inspection involved identifying events corresponding to an average S/N ratio greater than ~15. This ratio was computed by first computing the onset of the P–wave energy. An interactive first break picking algorithm using a running window Akaike Information Criterion algorithm (St-Onge, 2011) was used to determine the onset time for the arrivals. Then the trace energy for the Z-component traces for a 50 ms window starting at the onset of the arrival was compared to the trace energy for the previous 50 ms. All 20 events had P- and S-waves that were recorded on at least 2/3 of the 36 channels.

All 20 events were cross-correlated trace-by-trace to each other over a 0.3 s window. Figure 4.6 shows one of the 190 possible cross correlations between two events,

clearly showing high correlation between events 9 and 10. A cross-correlation energy estimate was computed by the sum of the square of the amplitudes from -0.1 s to 0.1 s lag for the sum of the individual 36 cross-correlations. These cross-correlation energy calculations clustered the events into four groups, similar to the final groupings shown in Figure 4.7. However, some of the high cross-correlations were skewed by high amplitude noise, especially on events 1 and 2 in Figure 4.7. Therefore, inspection of these cross-correlations was used as a confirmation for the final clustering.

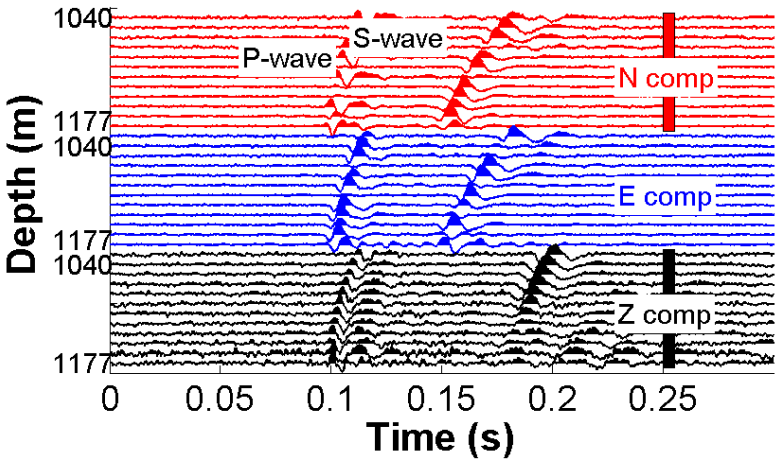

Figure 4.5 – Event 3 from the microseismic survey. The data for the horizontal channels were rotated using a vibroseis checkshot survey. A 10 to 800 Hz bandpass filter was applied to the data. The P- and S-wave arrivals are evident on most traces. The lack of consistent energy across the N and E horizontal components may be caused by poor geophone coupling or poor azimuth resolution.

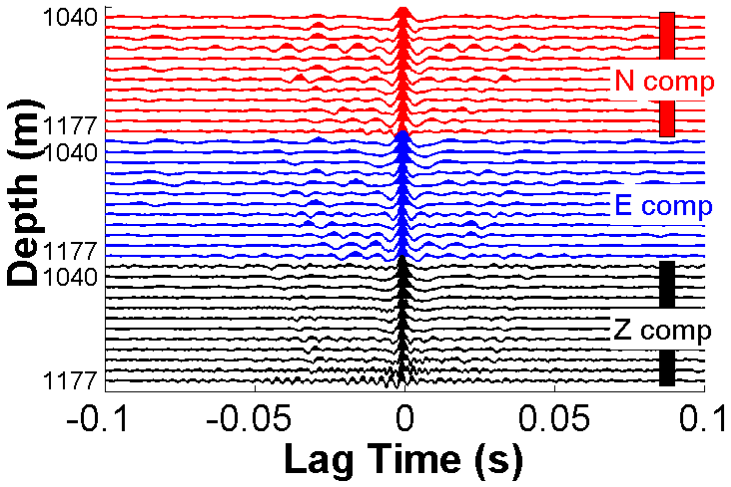

Figure 4.6 –Cross-correlations for each trace from events 9 and 10. The high cross-correlation resulted in the two events being attached to group C as shown in Figures 4.7 and 4.8.

Figure 4.8 shows 17 of the 20 events grouped into four clusters and plotted as a function of detection time versus propagation distance. Three of the events were not grouped because of low cross-correlation values. A P- to S-wave time difference algorithm was used to obtain the radial source to receiver distance. First, a velocity model was built using the using the sonic log from the observation wellbore as discussed below. Then a grid search using a MATLAB algorithm computed travel times for P– and S– waves. The minimum sum of the squares of the time residuals was used to determine the event distance. A hodogram from the P-wave particle motion was used to obtain the direction to the source. The hodogram analysis showed that the grouped events were within 10° of each other. The data clustered in both time and distance, except for two events.

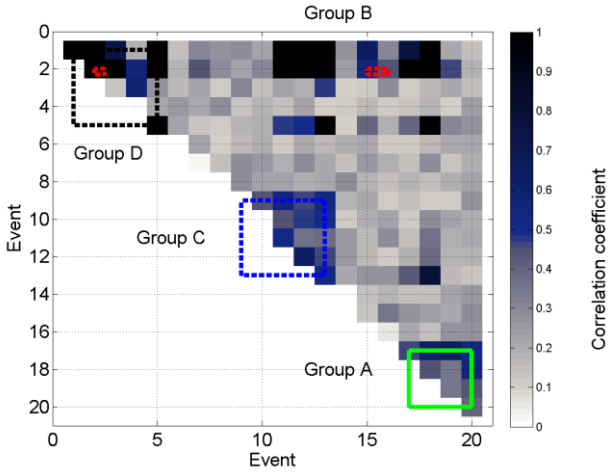

Figure 4.7 – Cross-correlation amplitude matrix for the 20 events (normalized to the highest cross-correlation energy for the sum of the 36 traces. The four clustered event groups are also shown. Some correlation coefficients are skewed by high amplitude signal signals and noise, such as the cross-correlations for events 1 and 2. This matrix was refined by inspection.

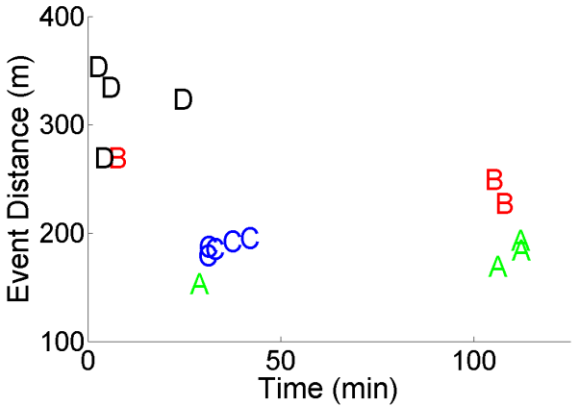

Figure 4.8 – Time vs. fracture distance cross-plot for 17 events from the microseismic survey. The events were grouped into four clusters lettered A to D based upon cross-correlations between all event pairs. Three of the events were not used as part of the clusters.

Figure 4.9 shows an enlargement of the Z-component traces for the P-wave arrivals for two events from cluster D. Although the P-wave arrivals appear similar in character (i.e. phase) and moveout, event 3 clearly has perceptibly higher frequency signal content. Figure 4.10 shows the frequency-amplitude spectra for the deepest vertical geophone for these two events. This geophone was placed within the 20 m thick reservoir zone. There is a spectral peak for both events at about 150 Hz. The curves have a similar form after about 300 Hz, but the frequency content for event 3 is consistently about 6 dB lower than event 4. Events 3, 4, 1, and 5 are interpreted to form a distinct group (group D in Figure 4.8).

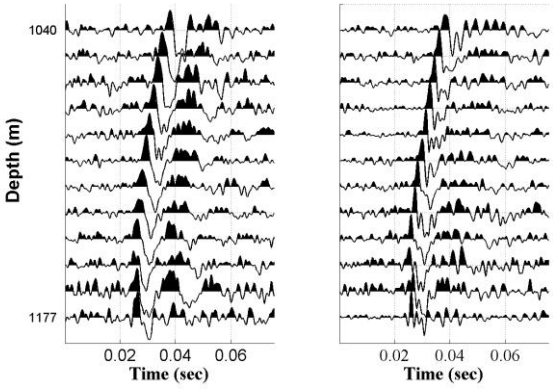

Figure 4.9 – A close up of the vertical-component traces for the P-wave recorded on event 3 (left) and 4 (right). The P-wave arrivals for event 4 contain perceptibly higher signal frequency content that can be seen in the narrower peaks and trailing troughs on the trace data.

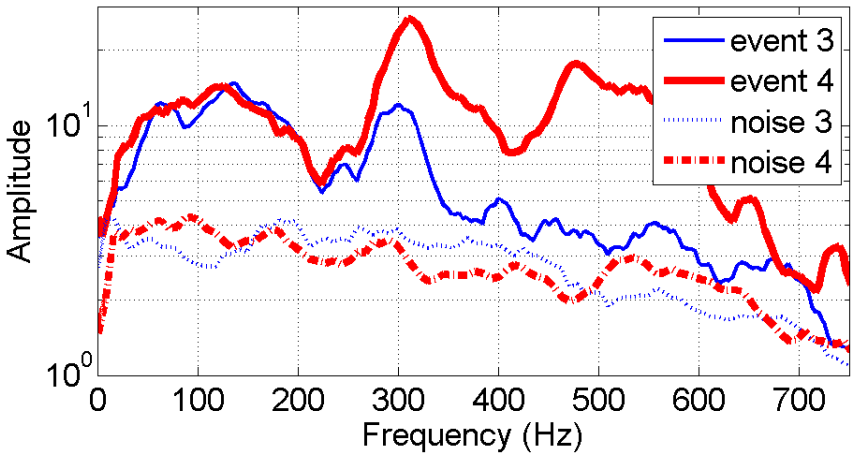

Figure 4.10 – Frequency-amplitude spectra for the deepest vertical geophone for event 3 and 4. Above 250 Hz, event 3 recorded consistently higher signal. The signal increase between 270 and 330 Hz and 440 to 540 Hz was observed on a number of the events. Also shown is the noise spectrum estimated using the preceding 0.1 s window before P-wave energy onset.

Figures 4.11 and 4.12 show the frequency-amplitude spectra for P-wave energy as recorded by the vertical-component geophones 80 m above the reservoir zone and 6 m within the reservoir zone for the four events clustered into group D. Three of the spectra are very similar in Figure 4.11. However, event 3 has consistently lower frequency amplitudes at this geophone depth. In Figure 4.12, three amplitude spectra show a 6 dB local high between 280 and 320 Hz and two spectra show a high between 440 to 540 Hz.

In summary, 17 of 20 high S/N events were clustered into four groups based upon high values of cross-correlation and visual inspection. The events occurred with the first

two hours of a 5 ½ hour hydraulic fracture microseismic dataset recording. The events clustered in both time and distance, except for three events. Examination of frequency spectra within the clusters reveals two consistent characteristics. Events inferred to originate from the same area may be characterized by lower frequency spectra above 300 Hz, or higher spectra between ~280 to 320 Hz and ~440 to 540 Hz. Based upon the path effect work of others (for example, Hogan and Eaton (2012), Lines et al. (1992) and Fagan (2012)), these results are worthy of further study.

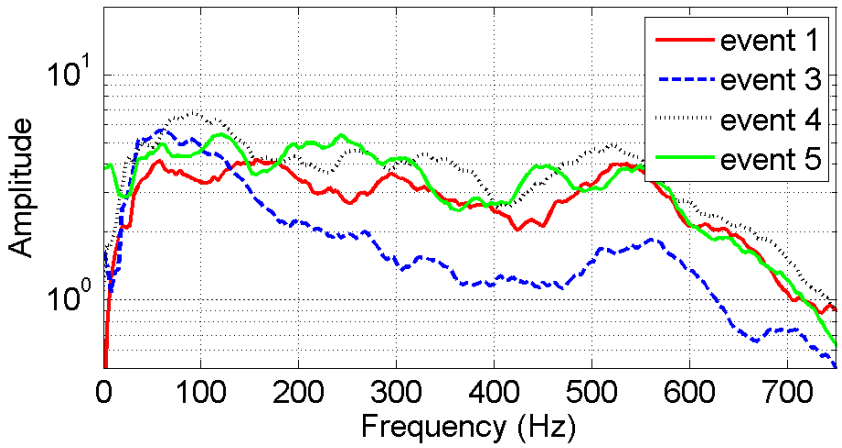

Figure 4.11 – Frequency-amplitude spectra for the vertical geophone 80 m above the reservoir zone for the four P-wave arrivals in group D on Figure 4.8. Three events have similar amplitudes at about 100 Hz and a similar shape thereafter. However, event 3 (dot-dashed blue line) has an overall lower frequency spectrum above 150 Hz.

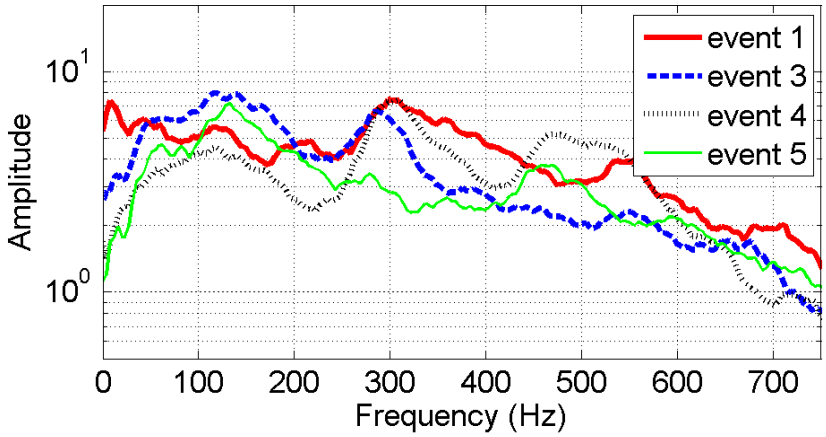

Figure 4.12 – Frequency-amplitude spectra for the vertical geophone 6 m in the reservoir zone for the four P-wave arrivals in group D on Figure 4.8. The events have similar amplitudes. However, three of the events have higher frequency amplitude spectra between 280 and 320 Hz, and one event has an elevated spectrum between 440 and 540 Hz.

4.4 **Finite-Difference Modeling**

Figure 4.11 shows the velocity and bulk density logs from the monitor wellbore. These logs were used to develop the finite difference model used here. The S-wave velocities were estimated from the P-wave velocities and density using Castagna's relationship (Castagna et al., 1985). The relatively low-velocity reservoir zone was 20 m thick in the wellbore and the subsurface depth to the top of the zone is about 1300 m. There is little variation in the reservoir thickness within 5 km of the wellbore; however, there are permeability variations, as estimated from variable productivity from the surrounding vertical wells.

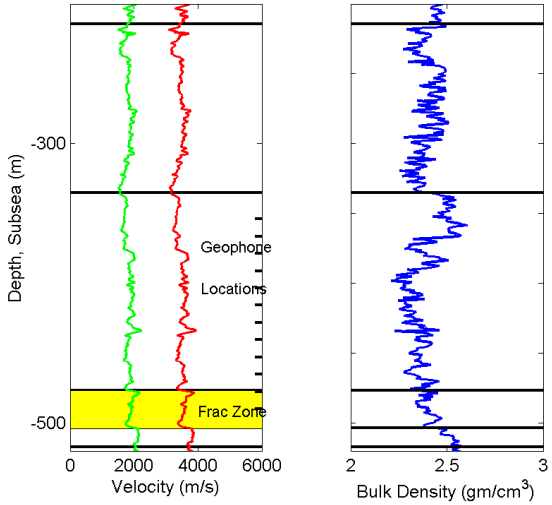

Figure 4.13 – P- and S-wave velocity log (left) and bulk-density log (right) from the monitor well, located 50 m north of the 1000 m horizontal treatment wellbore.

A velocity model was constructed by extending all data shown in Figure 4.13 into a 2-D grid (Figure 4.14). The modeled wavefields are propagated using an anisotropic elastic second-order finite-difference code based on the algorithm developed by Boyd (2006). The published MATLAB code has been modified to allow localized excitation using an arbitrary moment tensor and to improve performance of the absorbing boundary conditions. We calculate synthetic data using an explosive source and a minimum-phase 300 Hz dominant source signal (Figure 4.14). The velocity model is defined using a 1 m grid in both directions and the finite-difference time steps are 0.1 ms. These parameters were selected to minimize grid dispersion in the finite-difference code, and to ensure that the program did not exceed memory limitations.

In the synthetic data study, the source and geophone locations are laterally separated by 200 m, approximately the same as the detected events, which had a mean distance of 230 m and a median distance of 195 m. The source and receiver sampling positions were placed in the middle of a 400 m wide model to minimize edge effects. Moreover, the source and geophone positions were placed vertically from the highest computed source location and the highest geophone position to the base of the sonic log, as shown in Figure 4.14. The wave-field sampling (geophone) locations sampled particle motion in two Cartesian directions. The models here are laterally homogeneous and isotropic.

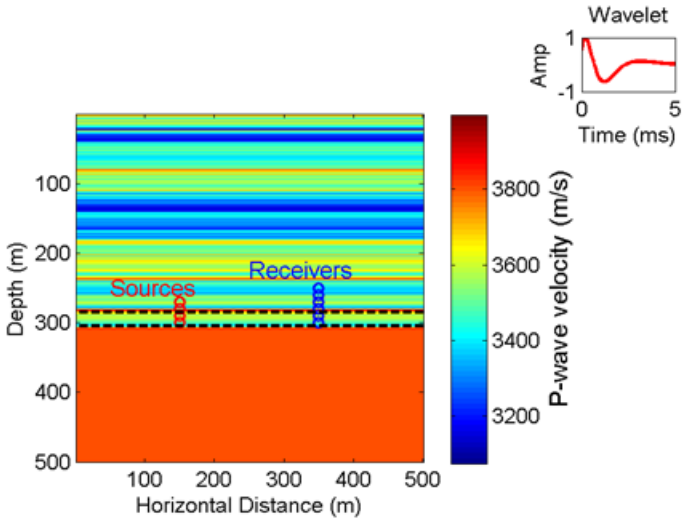

Figure 4.14 – P-wave velocity for the model constructed using the P-wave, S-wave and density profiles in Figure 4.13. Mode conversions were modelled, and the sources and receivers were placed to minimize model edge effects. A minimum-phase Ricker wavelet with a dominant frequency of 300 Hz was used.

Figure 4.15 shows the vertical component traces for the explosive source modeled at the 300 m level, within the reservoir zone. This is a representative result from the finite-difference algorithm. Although there is some energy after the P-wave energy, the P-wave energy is coherent along all traces. Figure 4.16 shows frequency-amplitude spectra for three sources placed 200 m away. One source was just above and two were with within the reservoir zone in the finite-difference model. The spectrum from the deepest source point shows a distinct signature, including 100 Hz wide amplitude peaks centered at ~350 Hz and 550 Hz. These peaks are similar in character to event 4 and (to a lesser extent) event 1 in Figure 4.10.

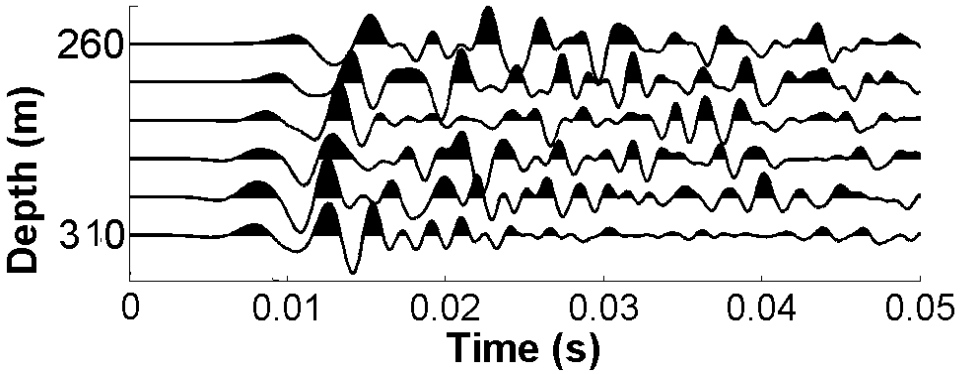

Figure 4.15 – The P – wave energy from the 300 m modeled source.

Figure 4.17 shows simulated frequency-amplitude spectra for two sources placed at the reservoir zone at 290 m and within the reservoir at 300 m and their wave-fields sampled at 300 m depth, also within the reservoir zone. The spectra have similar amplitudes up to ~400 Hz, and then the shallower source within the zone consistently has higher amplitudes. This is similar to the spectra in Figure 4.10. Since the source signatures in the simulations are identical, the differences in the modeled results can be ascribed to path effects.

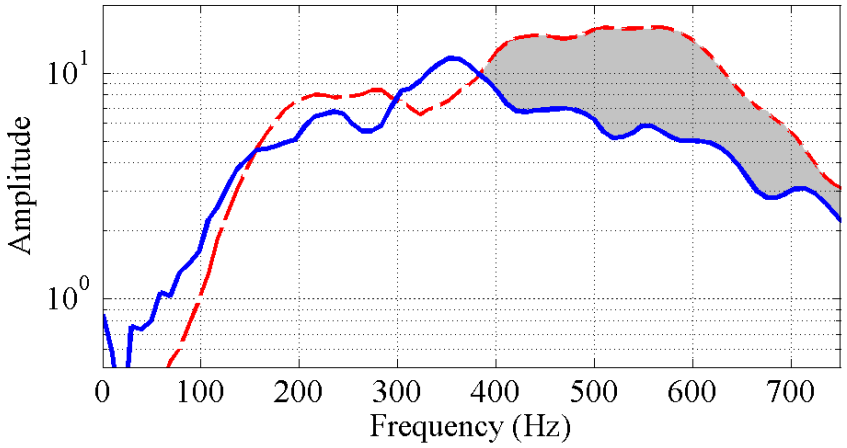

Figure 4.16 – Frequency-amplitude spectra for a vertical geophone at 300 m depth for shots at 290 m (red dashed line) and 300 m (blue) depth in the finite difference model. Both sources and receivers were in the reservoir zone. The modeled events show differences in high-frequency character (gray shaded area) that resemble the events shown in Figure 4.8.

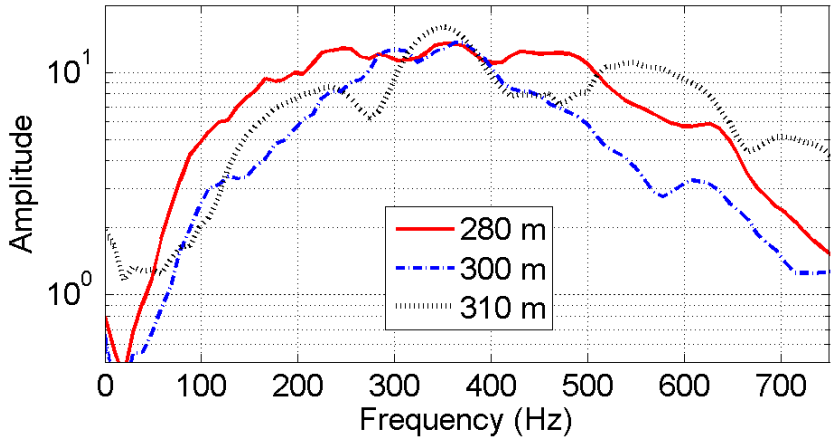

Figure 4.17 – Modeled frequency-amplitude spectra for the vertical-component wave field at 290 m depth (within the target zone) for sources located at three depths across the reservoir. About half of the 20 recorded events had spectral peaks similar to the 300 to 350 Hz peak for the 310 m depth.

4.5 **Discussion**

4.5.1 Recorded data and the finite-difference model

Figure 4.5 shows a high S/N ratio event that is representative of the events studied here. Most of the first-break arrival times for the P- and S-waves are unambiguous. Figure 4.6 demonstrates a very high correlation between events 9 and 10 in group C. Indeed, the plot resembles an autocorrelation function, suggesting that both events originated in very close proximity (Kokon and van der Baan, 2012). This is consistent with most results used to produce Figures 4.7 and 4.8. In total, there were 190 cross-correlations for the 20 datasets. The cross-correlation energy values could be used to sort most of the events into unambiguous groups, as shown in Figure 4.8. However, some high amplitude noise and some S–wave energy clearly arrived at a slightly delayed time, resulting in some spurious high amplitude cross-correlation energy values. As a result, a visual inspection of all of the cross-correlations was used for the final event groupings.

Two of the groups have closely spaced events in both time and space. Group D contains four events that occurred very early within the treatment in a 22-minute window, with calculated offset distances ranging from 269 to 334 m. Group C contains five events that occurred just after this in a 12-minute window, with calculated offset distances ranging from 179 to 195 m. Two groups include one event that occurred early in the treatment program. Group A contains three events that occurred within a 17-minute window at about 2 hours, with calculated offset distances ranging from 179 to 195 m. There is also one event that occurred at about 30 minutes at a closer distance. Finally, group B contains three events with one event occurring very early and two events about

100 minutes later. Here, the calculated offset distances ranging between 227 and 269 m. The two events separated in time correlated well with the other events in their group, indicating a possible reactivation of fracture energy at their locations. Three events that occurred relatively early in the monitoring program did not meet the criteria for multiplet classification and so were discarded from this study.

Figures 4.9 and 4.10 both show representative results for this study. The P- and S-wave S/N ratio was high (15.7 average RMS S/N ratio for the P-wave events compared to the trace 100 ms prior to the arrivals shown in Figure 4.7). Some events within a cluster are characterized by higher-frequency response. Consider Figure 4.10, which shows the frequency-amplitude spectra at one geophone level for two events from the same cluster. The two events occurred less than two minutes apart, have very similar moveout (Figure 4.9) and a marked change in the frequency amplitude spectrum above 300 Hz. This change is consistent with spectral characteristics evident in Figure 4.16, where energy spectra from different depths in the reservoir model were computed.

Figure 4.11 shows observations from vertical component geophones located 80 m above the treatment zone, which reveals similar spectra for 3 events from group A (Figure 4.8). However, the fourth event in the group has a subtle yet distinct drop in frequency amplitude across the spectrum. Similarly, Figure 4.12 shows results for a vertical-component geophone located 6 m within the treatment zone. The events have similar amplitude spectra, but three of the events have higher frequency amplitude spectra between ~280 to 320 Hz and ~440 to 540 Hz. In both cases, we surmise that this drop may be due to path effects, such as channel waves produced by waveguides (Lines et al., 1991). Greenhalgh et al. (2007) discusses similar variations in signal caused by a seismic

source placed within a coal seam. The source gives rise to channel waves, or multiply reflected body waves within the seam. Based on the finite-difference modeling I conjecture that changes in source depth produce corresponding changes in the measured amplitude spectrum as a result of destructive/constructive interference associated with path effects.

The finite-difference modeling is designed to simulate a relatively simple geologic model based upon the borehole logs from the monitoring well. A 300 Hz minimum phase Ricker wavelet was modeled from a number of source locations to a number of receiver locations above and below the treatment zone. The model results shown in Figure 4.16 are similar to two of the events from group 3 in Figure 4.10. The red and blue lines in Figure 4.16 track until about 400 Hz. Thereafter, the 10 m deeper source within the reservoir zone has lower amplitude. This is consistent with the separation observed on Figure 4.10. As proposed by Hogan and Eaton (2012), this observation suggests that characteristic site-specific elements of the spectral signature may provide a way to fine-tune inferred source depths. We remark that an unambiguous separation for a 10 m source depth difference could not otherwise be achieved based on time picks alone, due to the unavoidable presence of picking uncertainties. Thus, a method that enables more precise depth determination is of practical interest.

4.5.2 Simple Finite Difference Model

It can be difficult to interpret the finite difference model results using the model shown in Figure 4.14, due to model complexity. In an attempt to simplify the analysis, a number of simple finite difference models based upon Figure 4.14 were constructed, as

shown in Figure 4.18. This approach was used instead of constructing zero-offset synthetic traces or ray tracing algorithms, since these approximate methods are not full-wavefield approaches and so would not adequately represent the desired path effects. A number of source depths and receiver depths as shown in Figure 4.18 were tested for a number of models.

Consider Figures 4.19, 4.20 and 4.21, showing the results of an explosive source modeled with a 300 Hz minimum phase wavelet. The source was placed at 120 m depth and was one of 12 depths modeled, as shown in Figure 4.18. There is little variation in the sampled energy at all levels except the 140 and 150 m depths within the low velocity layer. Figure 4.20 shows the frequency amplitude spectra for the 140 and 150 m depths as similar to the other traces, except they contain notches in the spectra. The cross-correlation in Figure 4.21 shows the wavelet consistency, except at 140 and 150 m.

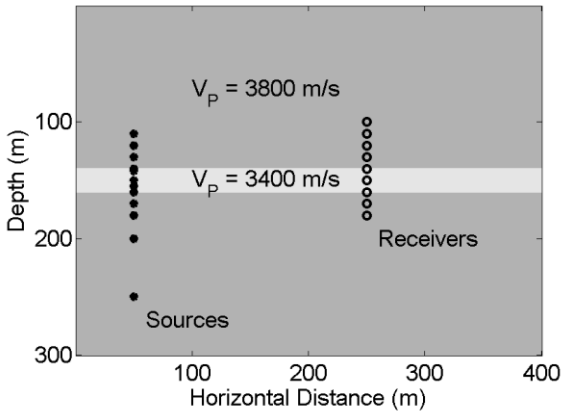

Figure 4.18 – The P-wave velocities for a simple model to test some path effect hypotheses. The low velocity layer is 20 m thick.

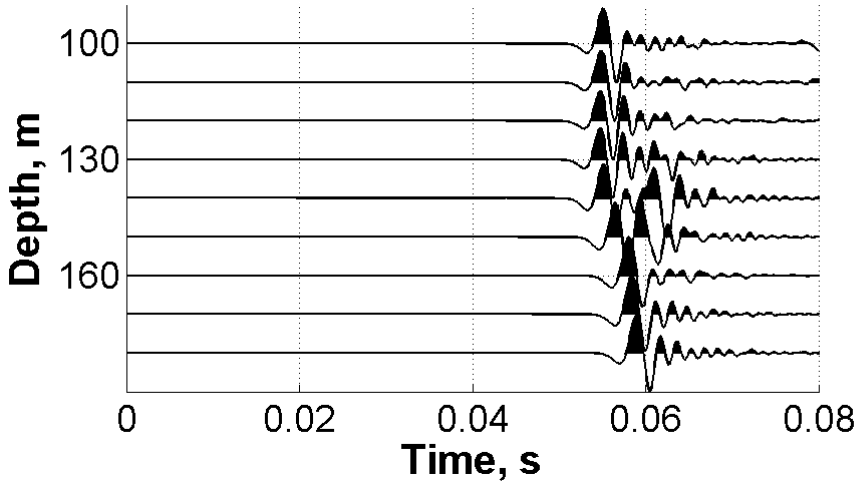

Figure 4.19 – The vertical channel recording for a 300 Hz minimum-phase Ricker wavelet source at 120 m depth, 20 m above the low velocity zone. There is no attenuation in the model; all variations in the measured wavelet can be attributed to path effects.

As shown in Figure 4.22 and discussed by Chung and Lawton (1999), thin-bed reflectivity can introduce notches in the frequency spectra. The notches will occur at a frequency difference equal to the inverse of the time difference between the reflected wavelets (see Figure 4.22). From Figure 4.21, there are two wavelets with envelope peaks 5.5 ms apart at the 140 m depth. This would correspond to a Δf ~180 Hz. For the 150m depth, there are two wavelets 4.3 ms apart. This would correspond to a Δf ~230 Hz. These notches may correspond to the notches observed in Figure 4.12. The notches in event 4 are ~180 Hz apart. These results are similar to thin bed response as discussed by Partyka et al. (1999) and Chung and Lawton (1999).

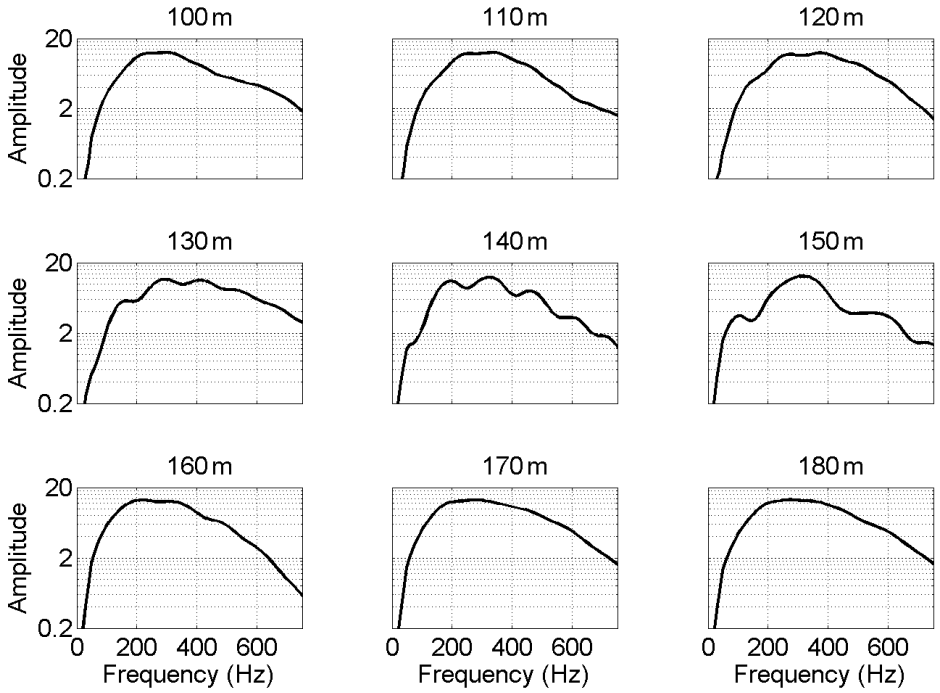

Figure 4.20 – The frequency amplitude spectra for the receiver traces shown in Figure 4.19.

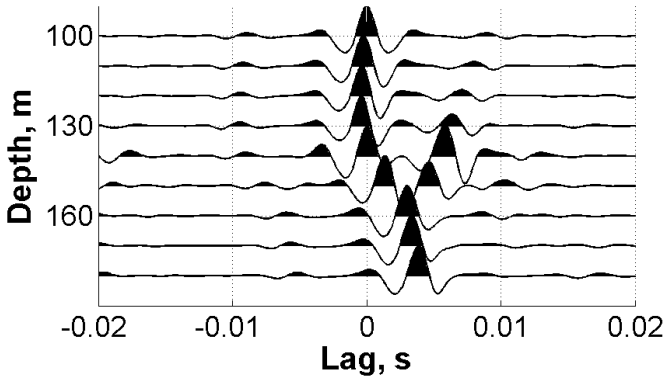

Figure 4.21 – Cross-correlations for the traces in Figure 4.19 with the 100 m depth receiver (the 100 m level is an autocorrelation). There is little change in the cross-correlation above the zone and a phase change below the zone. For the traces at 140 and 150 the correlations show energy with two different time lags.

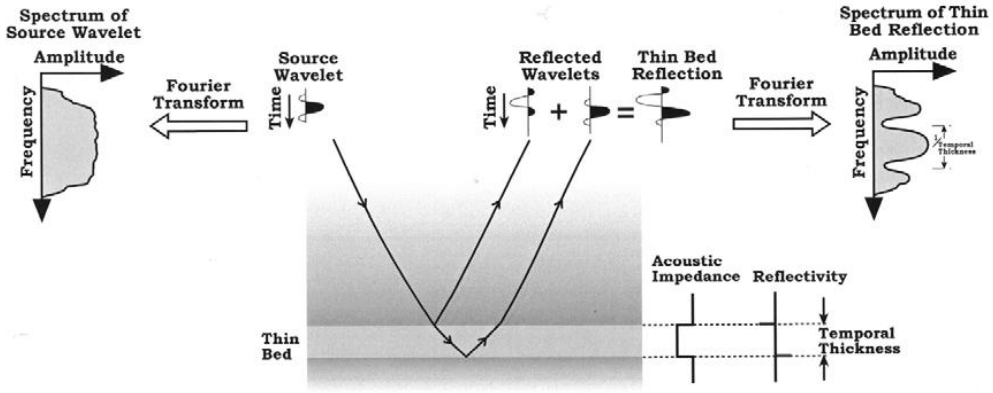

Figure 4.22 – Thin-bed reflectivity can introduce notches in frequency spectra (from Partyka et al., 1999).

Consider Figures 4.23 and 4.24 showing the sampled wavefields and spectra for an explosive source modeled at 160 m depth for the model shown in Figure 4.18. This is at the base of the low velocity zone. The energy envelope at the shallow traces from 100 to 130 m depth occurs over a short time period. After the arrival onset, the sampled waveform starts to become complicated. In particular, the 180 m depth sampled energy in Figure 4.23 shows the arrival of energy before the onset of the trough at 0.062 ms. It is thought that this energy is the direct arrival travelling in the higher velocity zone. This direct arrival would travel directly from the source to the receiver at 3800 m/s.

Next, consider the 140 and 150 m sampled depths in Figure 4.23. Here, the sampled energy occurs over a much longer time, appearing to contain high-frequency noise. This is also shown as the increase in the frequency content at the 140 and 150 m depth as shown on Figure 4.24. This effect is interpreted to represent interbed multiples, as discussed by Scherbaum (1994) and Chen and Atkinson (2002).

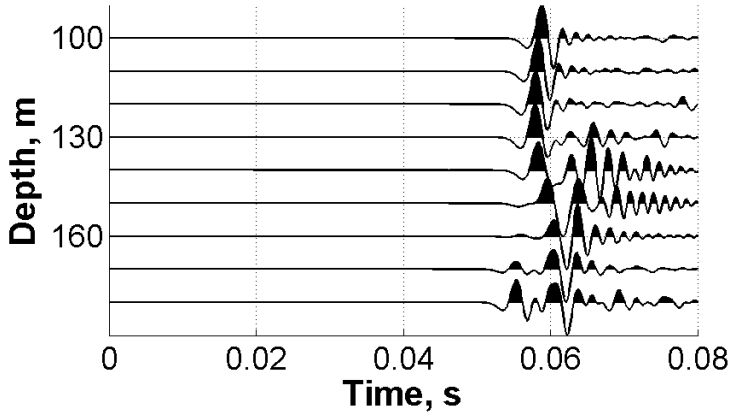

Figure 4.23 – The vertical channel modelled recording for a 300 Hz minimum-phase Ricker wavelet source at 160 m depth. The traces from 140 to 180 m sample anomalous path effects. The first event at 180m could be a direct arrival.

We can compare these results to Figures 4.25 and 4.26, which show the modelled P-wave energy for the vertical traces for event 2 and two of the trace spectra. The "ringy" traces (i.e. energy onset followed by sinusoidal oscillations) are sampled at the two geophone positions within the reservoir zone. Also, from the traveltime minimum for the P-wave energy, it appears as though the microseismic source was located within the reservoir. The ringy appearance of the synthetic data could be due to path effects of the low-velocity reservoir acting as a waveguide. From this comparison, it may be expected that data sampled within a low-velocity waveguide can be adversely affected by path. This is consistent with Pike and Eaton's (2013) investigation of coal seams.

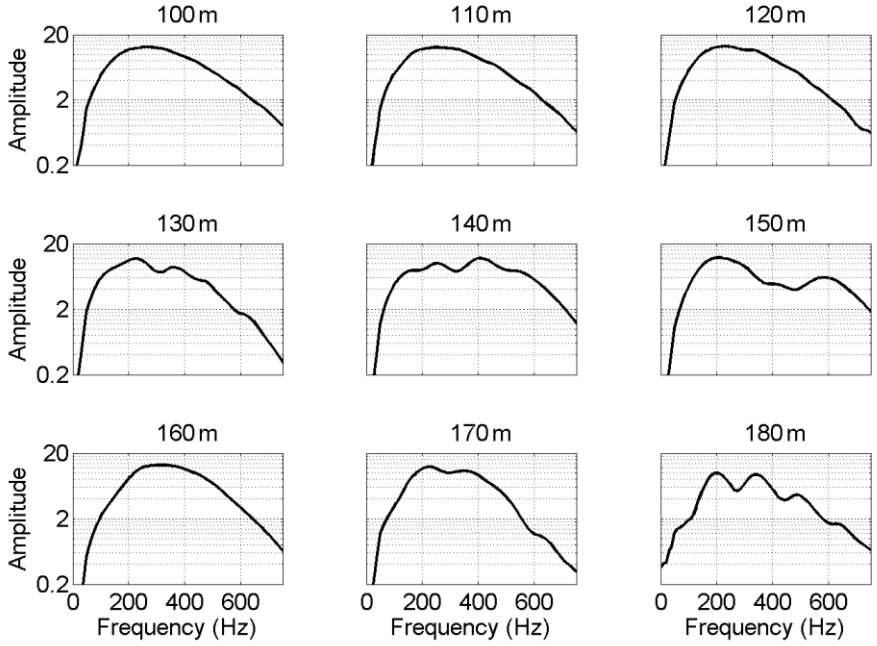

Figure 4.24 – The frequency amplitude spectra for the receiver traces shown in Figure 4.23.

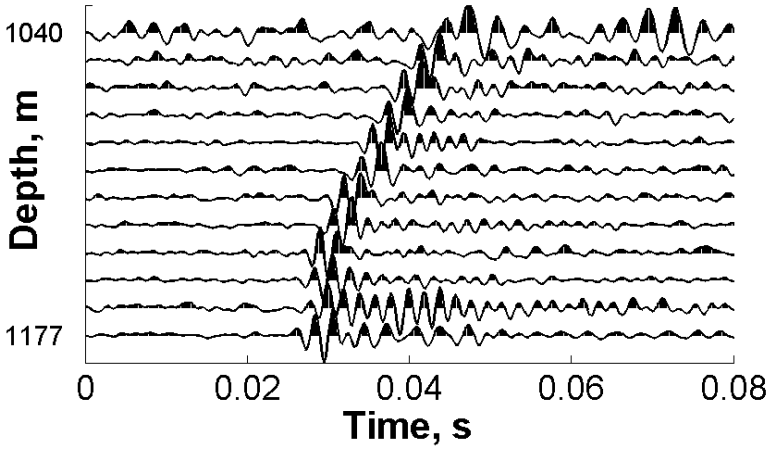

Figure 4.25 – The vertical channel P-wave recording for the second dataset. Note the 'ringy' energy recorded at the bottom two geophones. Both of these geophones were clamped within the reservoir zone. The minimum arrival time near the bottom of the array may locate the source within the reservoir.

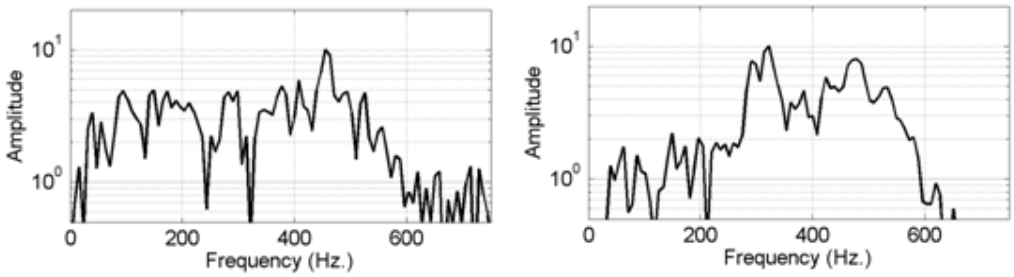

Figure 4.26 – The spectra for the shallowest trace (1040 m) and the second from deepest trace (1165m) from Figure 4.25. The short time window gives the FFT a `blocky` appearance.

Some of the synthetic data constructed using the model in Figure 4.16 were resorted and plotted in Figure 4.27. Sources at eight depths are sampled at the 160 m position, coinciding with the base of the reservoir. The spectra for these traces are shown in Figure 4.26. Again, notches are apparent in the spectra for the 150 and the 160 m source depths.

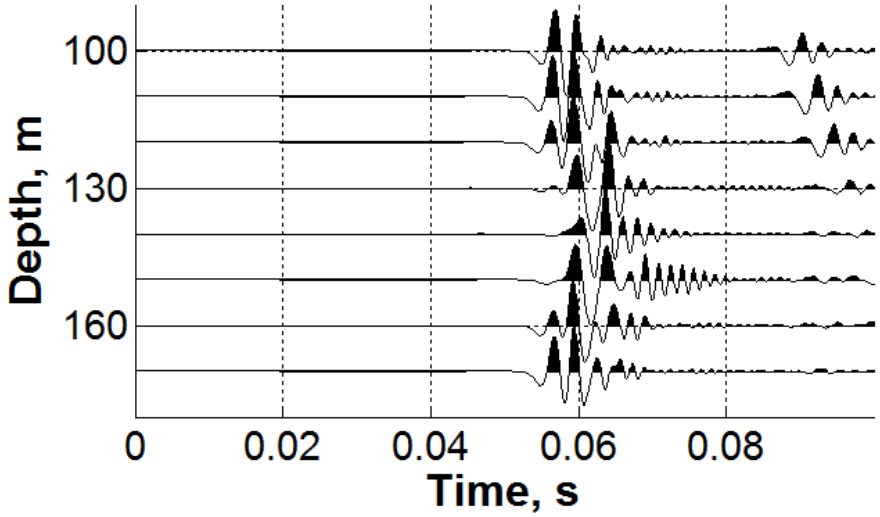

Figure 4.27 – The sampled energy at the base of the low velocity zone (160 m) for eight different source depths using the model shown in Figure 4.22.

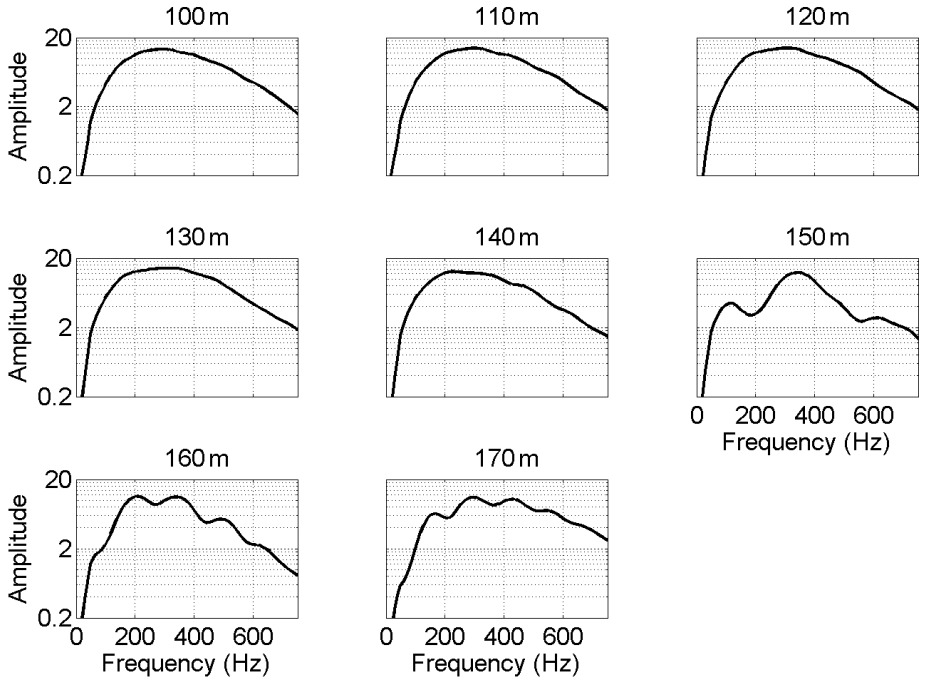

Figure 4.28 – Frequency spectra for the horizontal component traces in Figure 4.27 from 0.0 to 0.08 s. Note the spectral notches at the 150 m depth.

4.5.3 Wedge Model

A simple wedge model was constructed, as shown in Figure 4.29. A source and a sampling position were placed within the wedge. The low-velocity wedge was thickened from 3 to 25 m. Some results are shown in Figures 4.28 and 4.29. The most remarkable changes in the source wavelet occurred as the wedge thickness exceeded 19 m, manifested by notches and amplification at specific frequencies. From Figure 4.31, the 19 and 21 m thick zones display about 10 dB of amplitude change in the 400 to 700 Hz range. It appears as though 19 m represents a tuning level at which the path effects are particularly sensitive to bed thickness. The recorded data presented here were for a

reservoir about 20 m thick. This suggests that the reservoir thickness in this example may have been close to the tuning thickness required to result in significant path effects.

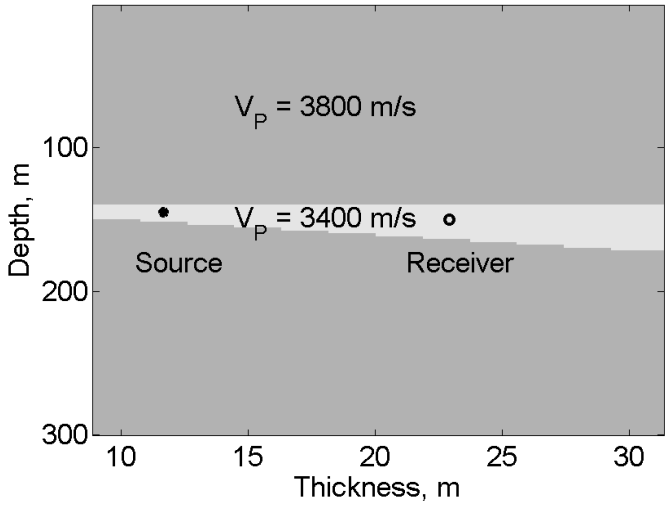

Figure 4.29 – A simple wedge model thickening a low velocity layer from three to 31 m.

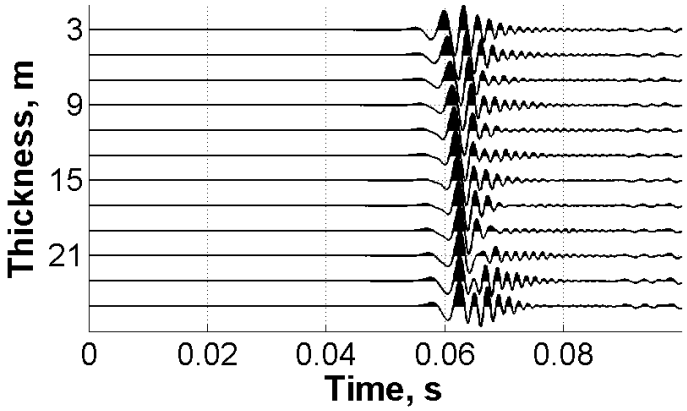

Figure 4.30 – The vertical component sampling for the wedge model shown in Figure 4.29.

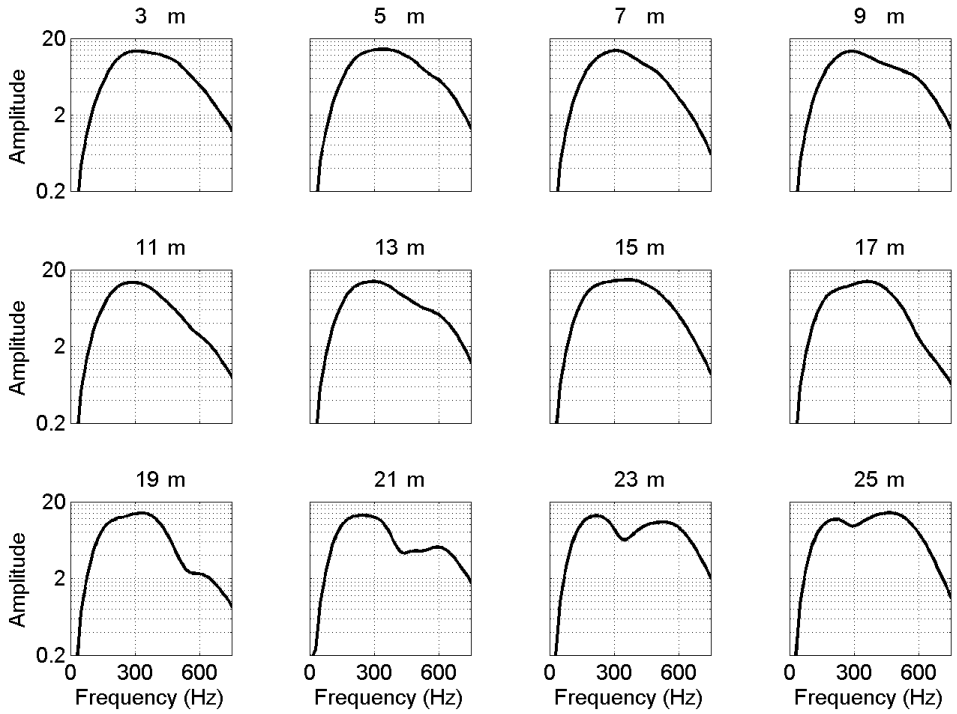

Figure 4.31 – Frequency spectra for the traces in Figure 4.30. Note the spectral notches at 19 and 21 m thickness.

4.5.4 Depth Grouping

The observation of persistent differences within certain frequency bands led to an automatic attempt to classify the frequency variations. An attempt was made to cluster modeled events in an automatic fashion based upon local notches and peaks in their frequency amplitude spectra. A cross-correlation was tried in the frequency domain. However, it was felt that some high amplitude spectra skewed these results that are not shown here. Fagan (2012) presents a statistical clustering of microseismic spectra to agglomerate events. The algorithm clusters events based upon small changes in

individual frequency spikes in the studied data. The frequency variations we observe here have a much broader spectrum than those described by Fagan (2012).

A simple algorithm and data display was developed for visual comparison of spectral variations for a number of arrivals. Consider Figure 4.32, showing the average amplitude ratio of the 280 to 320 Hz band vs. the 50 to 150 Hz band for the 20 events. The higher band was variable in the both the dataset and the finite difference models (see Figures 4.10, 4.12, 4.20 and 4.28). The lower frequency band was chosen as a baseline. Overall, this ratio is higher for the two geophones within the reservoir. In addition, the ratio is higher for event 4 than event 3 at the deepest geophone level, consistent with Figure 4.10. Inspection of other data confirms that this spectral ratio approach provides a robust indication of the aforementioned 280 to 320 Hz signal increase, with a few exceptions. The shallowest geophone consistently records an anomalous higher ratio, whereas, the geophone at 420 m has a consistently lower ratio. These anomalous recordings at certain geophone levels may represent local path or geophone coupling effects.

Figure 4.32 shows the average amplitude ratio of the 280 to 320 Hz band vs. the 50 to 150 Hz band for the finite-difference model results. Before construction of this amplitude-ratio matrix, it was thought that these results would be clear. The results in this figure show that the 290 to 360 Hz bands do not have a definitive pattern of amplitude ratios if the source and/or geophones are within the reservoir. The specific amplifications of frequency bands are expected to depend upon a number of factors, such as the velocity structure, the source and receiver lithology and geometries as well as the source mechanism and the waves generated.

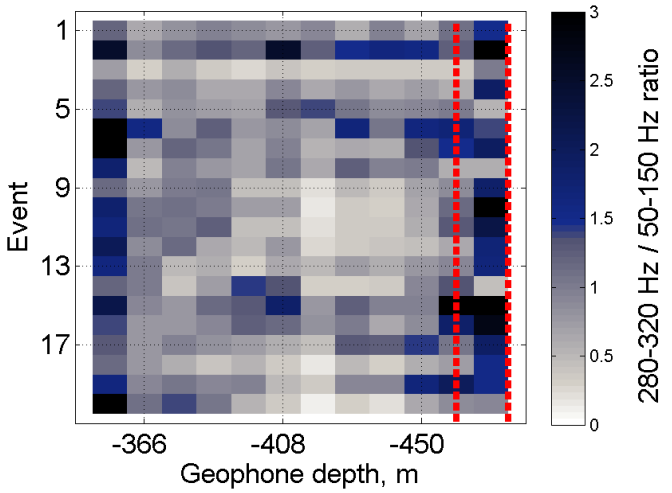

Figure 4.32 – Computed 280 to 320 Hz vs. 50 to 150 Hz. amplitude ratios for the 20 events. The two deepest geophones, within the reservoir, have the highest ratios. The shallowest level is contaminated with high frequency noise. The low ratio at the -420 m geophone depth may be receiver path effects.

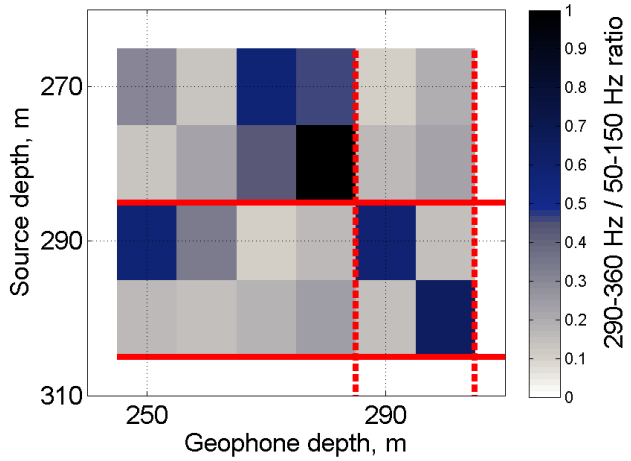

Figure 4.33 – Computed 280 to 320 Hz vs. 50 to 150 Hz. amplitude ratios for the six finite difference calculations. The reservoir zone is between the two red lines. Geophones at These ratios should be free of source and receiver path effects.

Figure 4.34 shows the average amplitude ratio of the 440 to 540 Hz band vs. the 50 to 150 Hz band for 19 of the 20 events. The ratios for event 2 were omitted due to the presence of high amplitude, high frequency noise that skewed the results. Overall, this ratio is consistently higher for the two geophones within the reservoir, as shown in Figure 4.25. These results are not surprising; if the sources for these events occurred within or near the reservoir, the slightly lower velocity reservoir could act as a waveguide for the higher frequencies. Multiple reflections within the waveguide would thus behave as a convolution filter. The increased path distance of multiple reflections would alter the attenuation characteristics as well. These observations are consistent with Scherbaum (1994), Lines et al. (1994) and Greenhalgh et al. (2007).

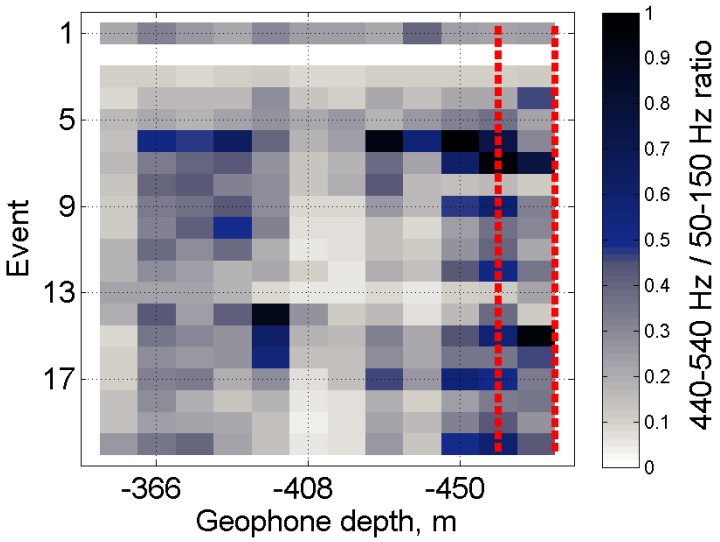

Figure 4.34 – Computed 440 to 540 Hz vs. 50 to 150 Hz. amplitude ratios for 19 of the 20 events. There are some patterns in the display, such as the high ratios at the two deepest geophones. The geophones at -408 and -420 m recorded consistently low ratio values. These could be receiver coupling effects, similar to site effects in earthquake seismology.

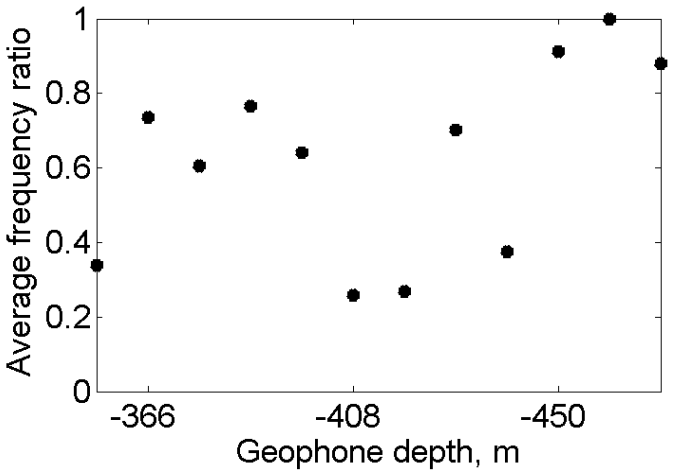

Figure 4.35 – The average frequency band ratio from Figure 4.34 averaged as a function of depth. The two deepest geophones have the highest amount of energy ratio. This could be lower dispersion in the lower velocity layer.

Figure 4.36 shows the average amplitude ratio of the 440 to 540 Hz band vs. the 50 to 150 Hz band for the finite-difference model results. If the receiver or the source is in the reservoir, there is a much higher likelihood of high amplitudes within the 440 to 540 Hz bandwidth. This is an empirical observation based upon the modeling of the P-wave frequencies in this study. It is thought that the frequency band of the path effects is a tuning phenomenon that depends on bed/waveguide thickness. A series of notches and amplification zones in the spectrum will develop. These spectral characteristics are likely to be complex in a real earth model, resulting in broadening of discrete pass/reject bands, such as the 440 to 540 Hz bandwidth.

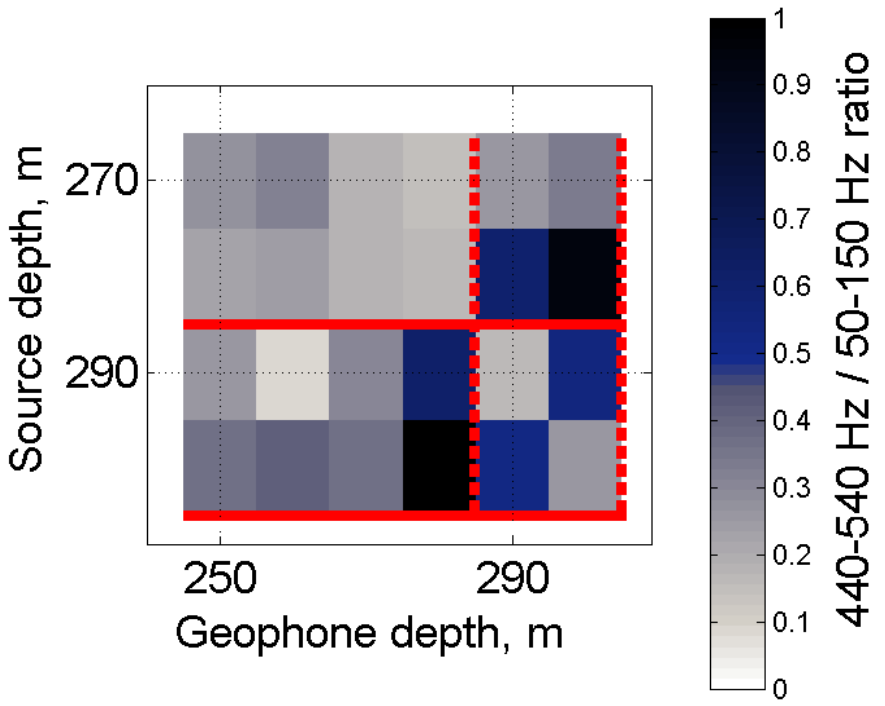

Figure 4.36 – Computed 440 to 540 Hz vs. 50 to 150 Hz. amplitude ratios for the six finite difference calculations. The reservoir zone is between the two red lines. These ratios should be free of source and receiver path effects.

4.6 **Summary**

In summary, we observe subtle but repeatable spectral amplitude changes for events coming from the same area of a hydraulic fracture treatment. We are able to model similar (although not identical) spectral characteristics using finite-difference modeling of P-wave arrivals. The source of the path effects is most likely due to interaction of the wavefield with layer boundaries; in particular, since the propagation direction is almost layer-parallel, post-critical, multiply reflected waves that slightly lag the direct arrival and are expected to modify the waveform of the direct wave. Since the finite-difference

modeling contains all types of waves, including multiples and head waves, these waveform modifications are implicitly contained within the modeled source spectra. Differences between the modeling results and observations may be attributed to complexities in the geological model that are not accounted for in the simplified, isotropic, non-attenuating, horizontally layered approximation.

Nonetheless, path effects could be used to reveal a more complete model of the rock geometry at the hydraulic fracture level and to group events from the same spatial region and/or depth. A spectral ratio method that may lead to a semi-automated scheme to group events should be further investigated.

4.7 **Conclusions**

Microseismic data acquired during a hydraulic fracture treatment in western Canada recorded 20 high S/N events of which 17 were clustered into four distinct groups and analyzed for path effects. Spectral analysis of the events reveals variations in recorded signals in the 280 to 320 Hz and 460 to 540 Hz bands. A coherent spatiotemporal pattern of events emerges from this clustering process. Spectra derived from elastic finite-difference synthetic seismograms shows that variations may be explained by path effects. This example suggests that identification and analysis of path effects could be used to reveal a more complete model of the rock geometry and improved depth-localization of microseismic sources.

Chapter Five: A Long-period long duration microseismic event

5.1 Summary

Passive seismic data recorded in a deep observation wellbore for the hydraulic fracture monitoring of a multi-stage treatment are analyzed to search for long-period long-duration (LPLD) events. Over 1000 conventional (high-frequency) P- and S-wave arrivals were located in a contractor analysis of the data. These arrivals were used to estimate event source positions. A previously unrecognized anomaly persists for over 20s and contains numerous low frequency events on all three geophone component orientations, with relatively consistent apparent velocities. The composite event represents the superposition of about 90 individual P- and S-wave arrivals and has characteristics similar to previously published LPLD examples. Such events observed on microseismic data may be analogous to deep low frequency tremor attributed to slow-slip processes along pre-existing fractures or strike-slip regimes at subduction zones. The identification and understanding of LPLD events in hydrocarbon producing regions is expected to contribute to the refinement of hydraulic fracturing processes.

5.2 Introduction

Hydraulic fracturing has emerged as an important method to improve the permeability and production for tight hydrocarbon reservoirs. Microseismic data are increasingly being recorded to locate induced fractures and fracture networks (e.g. Maxwell et al., 2010; Pettitt et al., 2009). Microseismic data are typically used to detect the arrival of P- and/or S-wave at a borehole from an induced fracture source and to infer a “stimulated rock volume” (Mayerhofer et al., 2008).

Some researchers have used other data to refine microseismic interpretations, with varying degrees of success. Urbancic and Baig (2013) compare microseismic deduced fracture patterns with core data and found good agreement. Maity and Aminzedeh (2012) and McGillivray (2004) both discuss positive results using integrated surface seismic data with well logs and microseismic data to improve the interpretation of time-lapse monitoring of hydraulic fractures. However, Hayles et al. (2011) tried to integrate 3-D surface seismic interpretations with microseismic interpretations from three different contractors; they concluded that "microseismic processing remains in its infancy."

Surface seismic and teleseismic data models have been used to aid in microseismic data interpretation. As discussed below, Zoback et al. (2012) interpret microseismic data anomalies as analogous to observations of tectonic tremor as reported by Shelley et al. (2006) for earthquakes. Moreover, Eaton et al. (2013) interprets LPLD events recorded on microseismic data in NEBC as analogous to observations of tectonic tremor.

"Episodic tremor and slip" is a phrase used to describe aseismic rumbling (tremor) thought to be caused by slow slip along a plate boundary or slow slip at subduction zones and strike slip faults at depth (Rogers and Dragert, 2003). Brown et al. (2013) recognized that Obara (2002) may have been the first to report this phenomenon associated with a plate margin. Obara (2002) was studying Japan earthquake records and noted deep long-period tremors occurring in nonvolcanic regions over a period of a few weeks. This is also discussed by Shelly et al., who examined low frequency earthquakes in Shikoku, Japan, and their relationship to episodic tremor and slip.

Tremor is recorded as low-frequency events over a long period of time, sometimes weeks. Brown et al. (2013) report similar events along the Alaska-Aleutian subduction zone that occur over periods of up to 20 minutes.

A similar type of tremor phenomenon is thought to occur in active volcanoes. In the case of volcanoes, the possible mechanism of generation is flow-induced oscillation from magmatic fluid travelling within channels (Julian, 1994). Volcanic tremor can be characterized by gradual or abrupt onset of low frequency oscillations that can change as a function of time. Usually the tremor can be correlated to the activity of a nearby volcano (Segall et al., 2006). Tary and van der Baan (2013) present microseismic resonance frequency anomalies similar to volcanic tremor and conjecture that the anomalies are caused by hydraulic fracture induced fluid flow in fracture networks.

5.2.1 Pembina Cardium Formation

In recent years, there has been an increase in the number of horizontal wells drilled and hydraulically fractured to improve hydrocarbon production productivity (see Chapter 1). This process includes recent horizontal drilling in the last five years in the Pembina Cardium pool in central Alberta (Figures 5.1 and 5.2). This pool is the largest in Canada based upon well count; there are currently 7404 wells in the pool at the Pembina field. This number includes 5617 wells currently producing about 64,000 barrels of oil per day (BOPD) or 10,175 cubic meters of oil per day (m^3/d) of oil (Figure 5.3). Cumulative totals are 1.323 billion barrels of oil and 1.34 TCF of gas (source: Accumap, accessed on June 1, 2013).

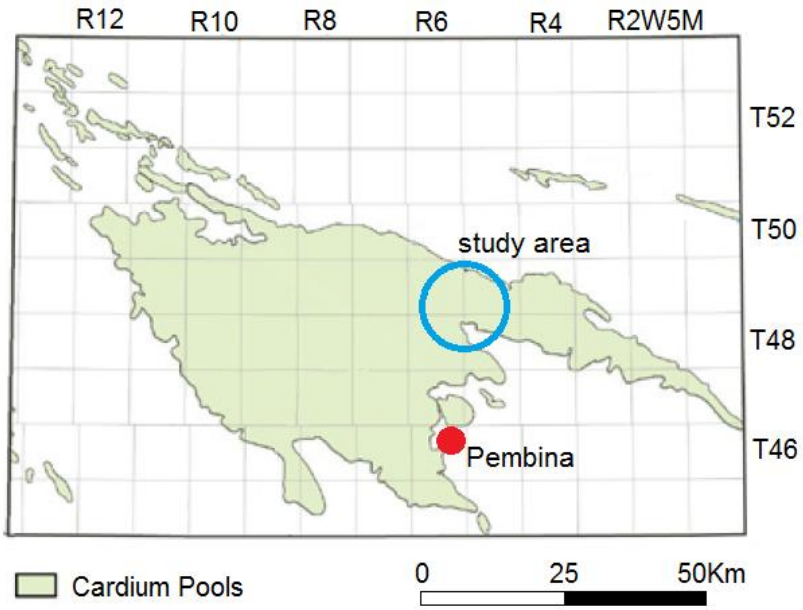

Figure 5.1 – Pembina area Cardium pool outline (adopted from Fic et al., 2011). The hydraulic fracture treatment well discussed here is within the study area shown.

The Pembina Cardium pool contains a tight, low permeability Cretaceous-aged Cardium sandstone/shale reservoir. The Cardium reservoir in the study area is broken down into two facies (Butrenchuk et al, 1995). The lower facies is a well-rounded clast-supported conglomerate that is matrix free or has a coarse sandstone matrix. The upper facies is a well-rounded conglomerate in a mudstone matrix. In the area, porosities range from 9 to 13%, with permeabilities in the 0.1 to 10 mD range (Fik et al., 2011). Using a 6% porosity cutoff as a minimum for net pay estimates, the study area has an average pay thickness of ~16 m over a gross thickness of the ~ 20 m interval (McNamara, 2012). It is important to note there is local variation in the porosity and permeability of the reservoir.

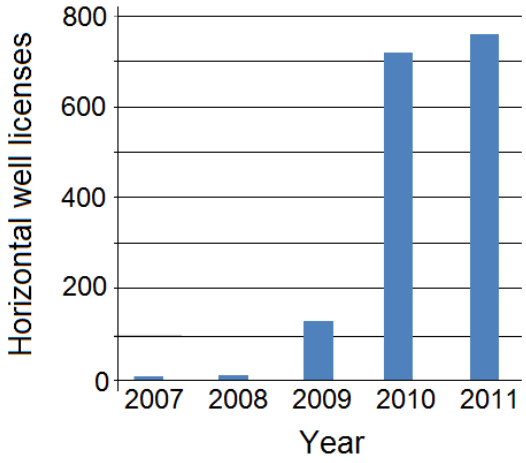

Figure 5.2 – Pembina area Cardium pool horizontal well licenses, by year. There has been a dramatic increase in horizontal drilling, beginning in 2009. Most of these wells were stimulated by hydraulic fracturing (NEB, 2011).

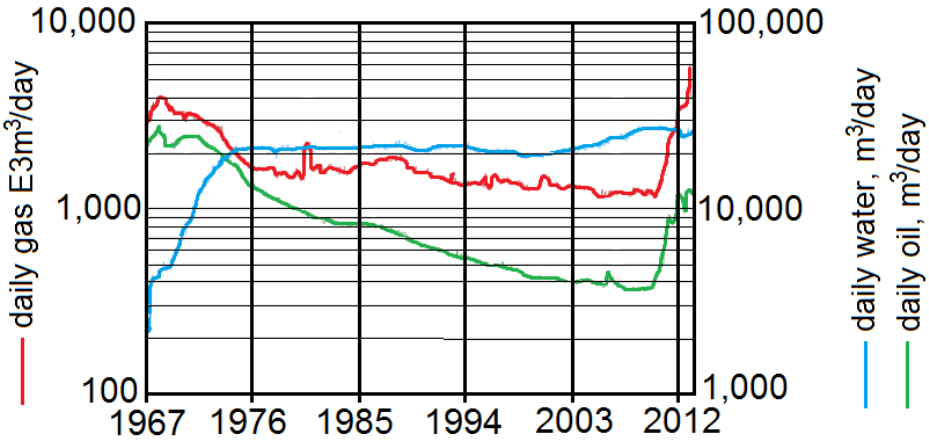

Figure 5.3 – Pembina area Cardium production (source: Accumap, accessed June 1, 2013), showing a dramatic increase in production since 2009 (see Figure 5.2).

5.2.2 Hydraulic Fracturing

The pressures required to achieve breakdown in hydraulic fracture treatments applied to the Cardium reservoir follow similar relationships used for other reservoirs (McNamara, 2012). The pressure required to create and propagate fractures can be estimated from previous experience in the area, laboratory measurements or theoretical calculations based upon rock strength and depth versus pressure gradients (Eberhard, 2011).

Hawkes et al. (2005) discuss the benefits of using area experience to minimize unforeseen differences between laboratory and field measurements. Many contractors performing hydraulic-fracture stimulations apply a fracture gradient from experience using a form of (5.1) to determine the pressures required for fracture initiation and propagation (Eberhard, 2011) to estimate the well head treating pressure required to induce fractures (WHTP):

$$WHTP = BHTP + P_{PIPE} + P_{PERF} - P_{PORE\ PRESSURE,} \tag{5.1}$$

Where *BHTP* is the bottom hole tubing pressure which is equal to the fracture gradient times the depth plus the excess pressure estimated to propagate the fracture. Also, P_{PIPE} is the friction pressure from the fluid resisting flow within the pipe, P_{PERF} is the pressure drop across the perforations (= 0 for open-hole completions), $P_{PORE\ PRESSURE}$ is the pore pressure in the reservoir.

Consider (5.1) for a horizontal well at a constant depth within a reservoir with homogenous thickness, porosity and permeability. For an open-hole hydraulic fracture treatment, the *WHTP* should be greater at the toe of the well, to account for friction

losses. All else being equal, as the stimulation stages progress from the toe back to the heel, a homogenous reservoir should therefore fracture at a lower *WHTP*.

5.2.3 Seismic Data

The data presented here were donated to the Microseismic Industry Consortium for analysis. The continuous dataset is 5.5 hours in length and consists of 12 3-C geophone data recorded in a deep borehole monitoring P- and S- wave energy from a hydraulic fracture treatment performed in August 2010. The geophones were mechanically clamped to the side of the borehole and their orientations were determined by a five location surface seismic vibroseis survey.

In this study, a 20 s anomaly recorded on all 36 channels about half-way into a hydraulic fracture treatment is presented. The anomaly is analyzed by examining its characteristics, including frequency spectra, apparent velocity and P- and S- wave signal content. These characteristics are compared to two LPLD events presented in the literature, as well as a recorded earthquake. We also analyze the wellhead treating pressures and microseismic data interpretation. The location of an interpreted fault is considered as a potential source for the LPLD event. The fault orientation is compared to other fault orientations in the area. These orientations agree well with principal stress directions. We summarize by briefly exploring the implications of observing LPLD events on microseismic data.

5.3 Observations

The microseismic data were recorded in a vertical wellbore 25 m north of a west-to-east oriented 1500 m long horizontal wellbore (Figure 5.4). A 14-stage open-hole hydraulic fracture treatment was monitored with twelve 3-component geophones separated by 12.47 m within the vertical wellbore. The horizontal geophones were rotated to north and east compass directions using azimuth information obtained by a five-position surface vibroseis dataset recording.

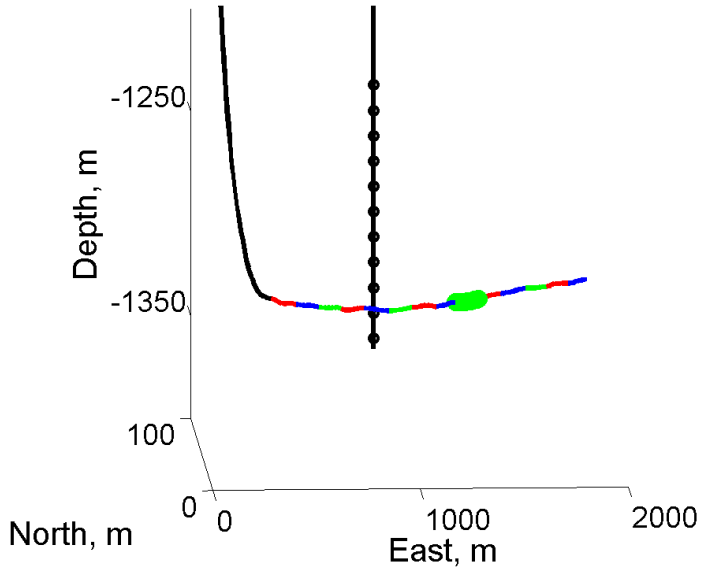

Figure 5.4 – A plot showing the horizontal wellbore and the offset vertical monitor wellbore. The hydraulic fracture stages are shown in colour. The thicker green-coloured stage is the 6th stage, as discussed below.

The microseismic dataset was analyzed by inspection of spectrograms. As shown in Figure 5.5, spectrograms are frequency amplitude vs. time plots of time series data. A

representative single geophone was selected for this analysis. Figure 5.5 shows 100 s of data beginning at 2 hours and 46 minutes from the start of the data recording.

Based on examination of the entire 5.5 hours of continuous recording, the low-frequency event shown in Figure 5.5 is unique in this dataset. The event has little coherent energy above 60 Hz and persists longer than any other recorded signal or noise. Moreover, the anomaly was recorded on all channels. Although the event is evident after 30 s of recording on the spectrogram, the anomaly after this time was difficult to see on the trace data. Finally, this energy was not identified in the contractor report.

Figure 5.6 shows the rotated but unfiltered trace data for the first 20 s of the anomaly. Although the time scale is too compressed to show detailed events, there is almost vertical time alignment observed for a number of events for each of the three component arrays. Figure 5.7 shows an expanded and bandpass filtered 3 s portion of Figure 5.6. There are a number of events that are evident on these data, especially on the vertical channels.

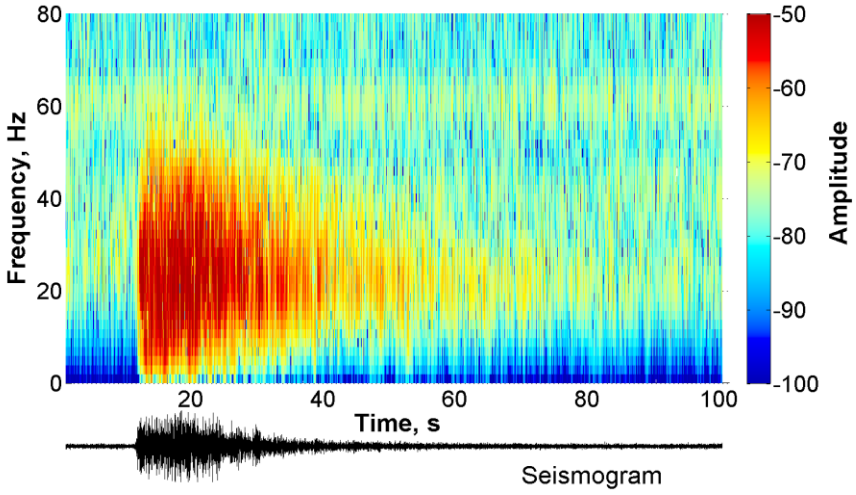

Figure 5.5 – A spectrogram for the 10th vertical component trace (1152 m depth) from the dataset along with the 10th vertical trace. The 60 Hz maximum signal at the onset of the event gradually decreases to about 30 Hz near the end of the event.

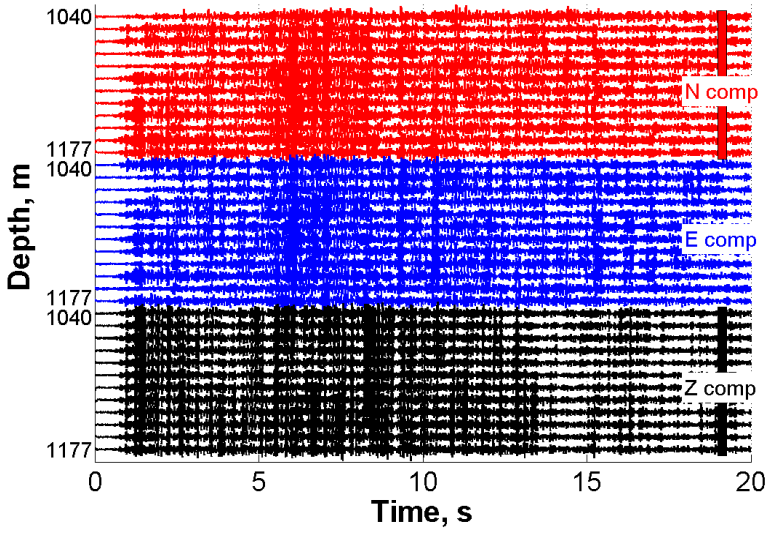

Figure 5.6 – A 20 s record (starting at 10 s with respect to Figure 5.5) showing an LPLD event recorded on all channels. About 90 individual events can be discerned.

A 300 ms window for the vertical traces from Figure 5.7 is shown in Figure 5.8. Prior to plotting, these data had a 5 – 100 Hz bandpass filter applied. There are five events highlighted that are compared to a constant velocity line. There are small variations between the constant velocity lines and the traveltimes for the events across the array that manifest as different apparent velocities in the velocity spectrum ("vespagram") in Figure 5.9. A vespagram is a measure of stacking velocity coherence as a function of time. The deep offset traces are used for the t_0 locations. Trace amplitude sums are computed from these locations at -3000 to -6000 m/sec (the positive downward slope is defined as negative) and their resulting coherence is plotted in colour.

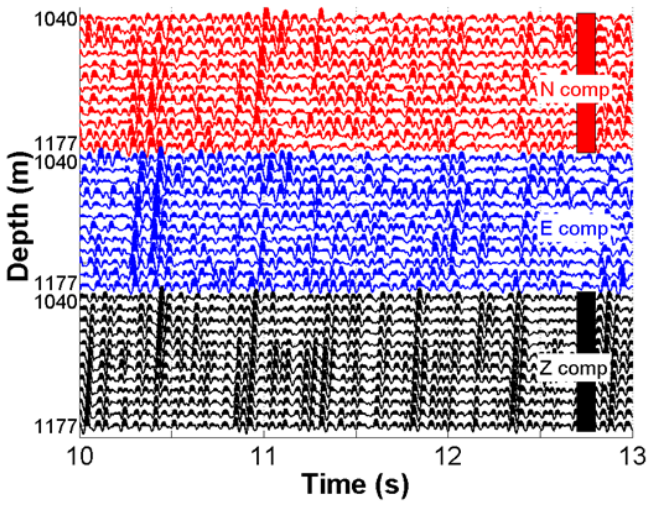

Figure 5.7 – A trace-normalized three second recording from Figure 5.1. The data were rotated to north and east orientations and have been bandpass filtered with a 5-100 Hz filter. The coherent energy is strongest on the Z component, except for the arrival at ~ 10.3 s.

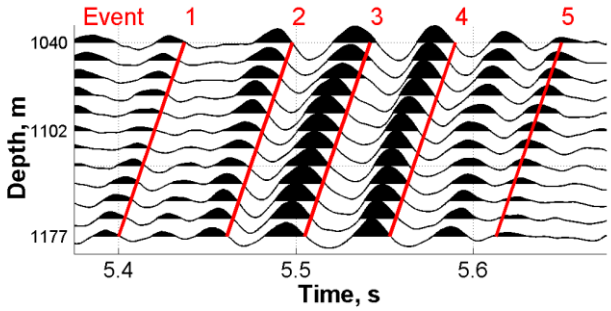

Figure 5.8 – A 300 ms window for the Z-component traces showing 5 events. The events appear similar in phase and frequency content. Compared to the red lines (V = 3790 m/s), there are subtle differences in the apparent velocity. This is consistent with Das and Zoback (2012).

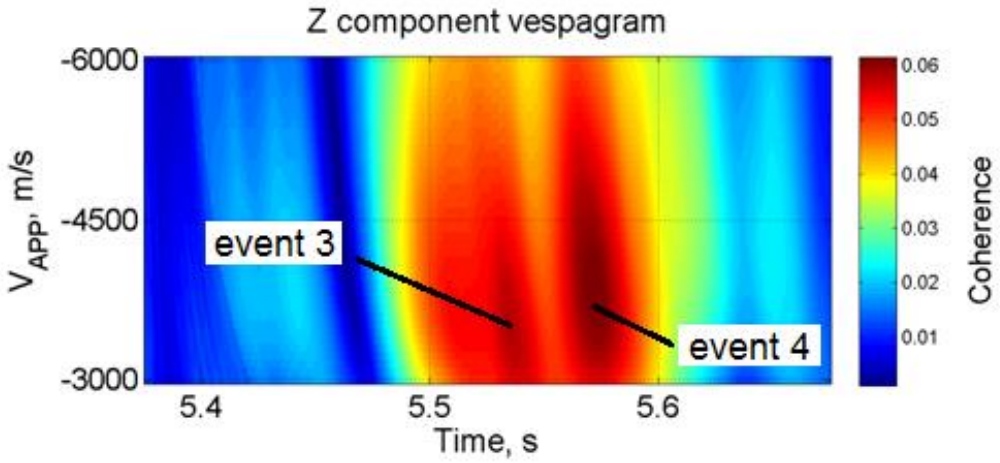

Figure 5.9 – A velocity spectrum ("vespagram") for the traces shown in Figure 5.8. Events 3 and 4 appear to have a similar linear moveout in Figure 5.8, but the vespagram shows a higher absolute velocity for event 4.

Figure 5.10 shows a hodogram representative of the dataset. Hodograms represents crossplots of recorded signals on different channels (Mahob and Castagna, 2001). A

principal component analysis of hodograms can give the direction of arrival for incoming energy. In this case, most of the energy is recorded on the vertical channel.

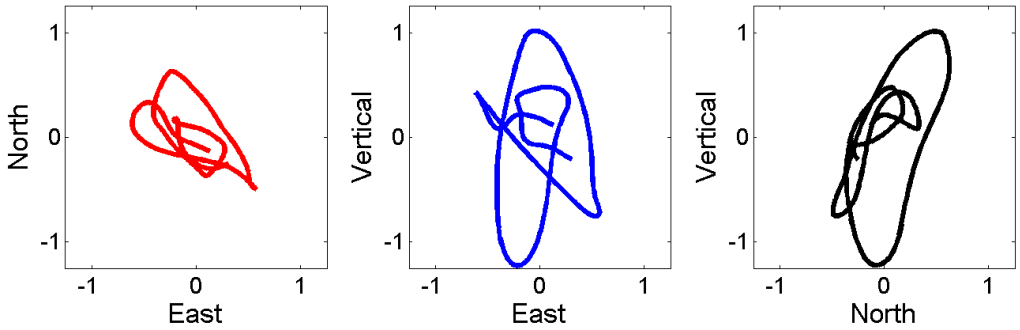

Figure 5.10 – Hodogram crossplots for the event at 10.8 s in Figure 5.7. A large portion of the energy is on the vertical channels.

The frequency amplitude spectrum in Figure 5.11 shows a very low dominant frequency of about 20 Hz for the possible LPLD event. Microseismic events on the dataset have broad frequency spectra ranging from 10 to over 600 Hz (see chapter 4). The background noise on the dataset (as determined by the spectra for the 1164 m depth vertical component trace 0.1 s before the data shown in Figure 5.6) is approximately equal in amplitude to the higher frequencies in the LPLD event.

Figure 5.12 shows a microseismic event recorded in the survey. These events are discussed in Chapter 4 of this thesis. Clearly, the event and the anomaly shown in Figure 5.7 are different. The frequency content, non-linear moveout and separation of the P- and S-waves on Figure 5.12 exemplify this difference.

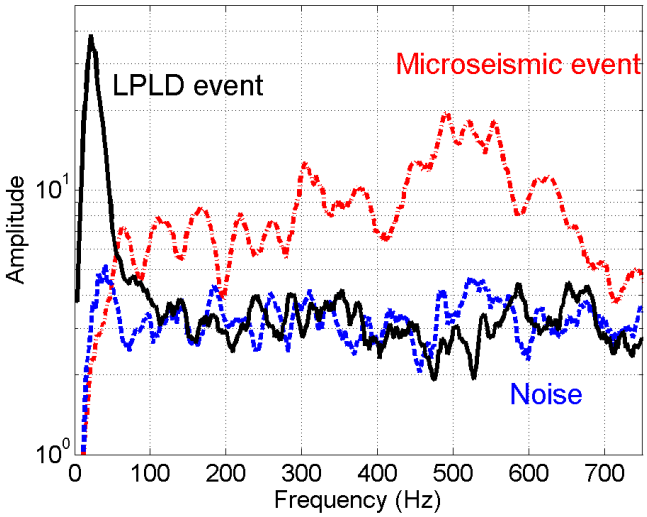

Figure 5.11 – Spectrum from one Z-component trace at 1164 m depth for the LPLD, the microseismic event in Figure 5.12 (vertical channel at 1165 m depth) and background noise. The LPLD event has comparatively very low frequency.

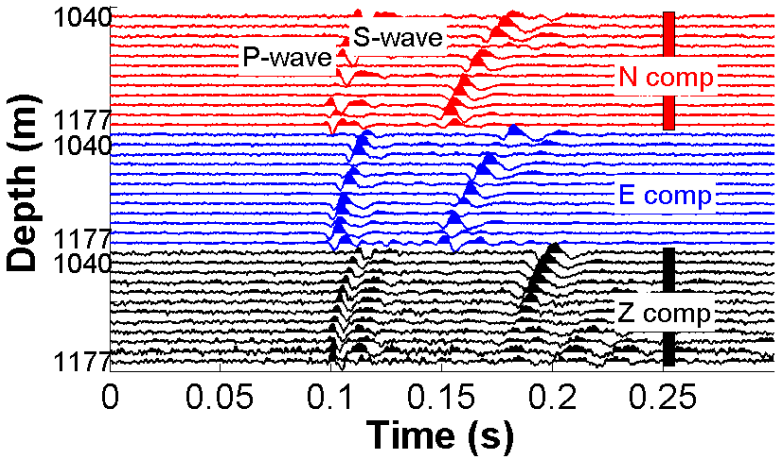

Figure 5.12 – Representative high-frequency event from the microseismic survey. A 10 to 800 Hz bandpass filter was applied to the data. The well-define P- and S-wave energy do not resemble the event in Figure 5.5.

Figure 5.13 shows the apparent velocity calculated for 28 events recorded on the Z-channel traces shown in Figure 5.6. The criteria used to choose the 28 events were two-fold. The signal had to be consistent for all Z-channel traces, and the events had to be at least 0.3 s apart. There does not appear to be a trend in the apparent velocity as a function of time. The events have a negative apparent velocity, implying that the source is below the geophone array.

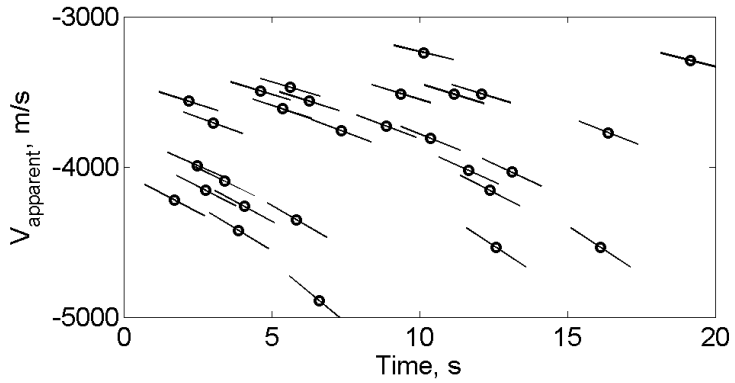

Figure 5.13 – The apparent velocity calculated for 28 events in the 20 s anomaly using the Z-channel data. The minimum V_{APP} ~ 3240 m/s, the maximum V_{APP} ~ 4890 m/s and the median V_{APP} ~ 3790 m/s. The line slopes are equivalent to the V_{APP}.

In summary, a 20 s event was recorded on 36 geophones midway through the recording of a 5.5 hour long hydraulic-fracture monitoring program. The anomaly is interpreted to contain about 90 separate events that have a median linear apparent velocity of ~ 3790 m/s (minimum ~ 3240 m/s, maximum ~ 4890 m/s). The event contains low frequency that initiates at frequencies up to ~ 60 Hz, declining to ~ 20 Hz at the end of the event. This frequency range is below typical dominant frequencies for P- or S-wave events recorded in this dataset.

5.4 **Discussion**

5.4.1 Comparison to a recorded earthquake

The 20 s anomaly recorded on all 36 channels is characterized by numerous low frequency P- and S-wave arrivals with linear apparent velocities between 3790 and 4890 m/s. The anomaly is consistent with those presented by Zoback et al. (2012) and Eaton et al. (2013), who both compare their observations to tectonic tremor as reported by Shelley et al. (2006) for earthquakes.

An alternative interpretation is that the signals may originate from a regional earthquake (Eaton et al. 2013 or Eaton and Boroumand, 2013). Consider Figure 5.14 comparing the 10^{th} vertical trace on the potential LPLD event to an earthquake recorded in the area as shown on Figure 5.15. The earthquake was recorded ~ 500 km north of the study area and was located ~ 100 km southwest of the study area. The earthquake is larger in magnitude (3.5 Mw) compared to the events presented here (-4.4 to -2.7 Mw).

The earthquake trace has some very low-frequency motion and three distinct arrivals. The low frequency is partly due to the distance travelled to the recording station; a closer station (in the study area, for example) should have detected higher frequencies. These arrivals are thought to be the P- and S-waves, as well as a wide angle reflection from the Moho discontinuity. The LPLD event has higher frequency content than expected by an earthquake (Figure 5.11). Careful inspection of the LPLD event (Figure 5.7) reveals it is not characterized by an impulsive start with experimental decay, as usually exhibited by earthquakes. Based upon the comparison of the large number of events and the frequency content of the earthquake, it is not felt the anomaly examined here is an earthquake.

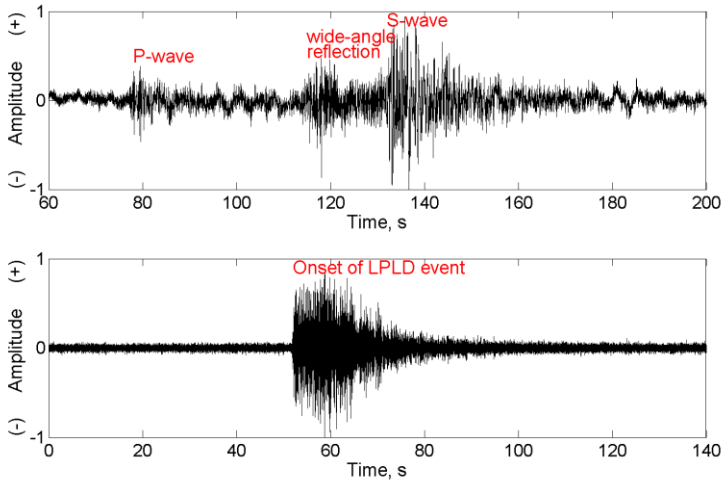

Figure 5.14 – Comparison between a 3.5 Mw magnitude earthquake recorded at RDEA station on June 3, 2013 at 9:14 AM and the LPLD event (the trace amplitude a representative vertical trace (depth 1152 m) from Figure 5.6.

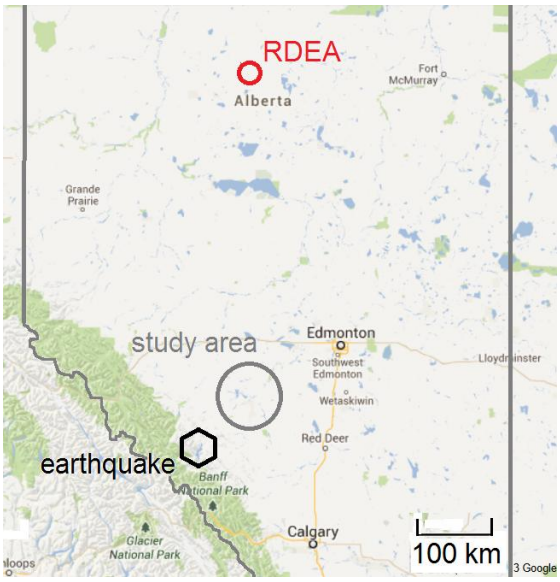

Figure 5.15 - The 3.5 Mw magnitude earthquake plotted on Figure 5.14 was recorded at RDEA station on June 3, 2013 and located at 52.443° -116.431° as shown.

5.4.2 Contractor report for pressures

Consider Figure 5.16 showing the surface injection pressure for 12 stages of the 14-stage hydraulic fracture treatment. Also shown are the wellhead treating pressures estimated to produce breakdown provided by the contractor using Eqn. 1. Recall that the well was an open-hole hydraulic fracture treatment that started at the far end of a 1600 m horizontal leg. The initiation and propagation of fractures occurred for the nine stages at the toe of the well. Then, the reservoir quality may have decreased at the heel of the wellbore, as increased pressures could not initiate a fracture. Also, note that the LPLD event occurred immediately after stage 6.

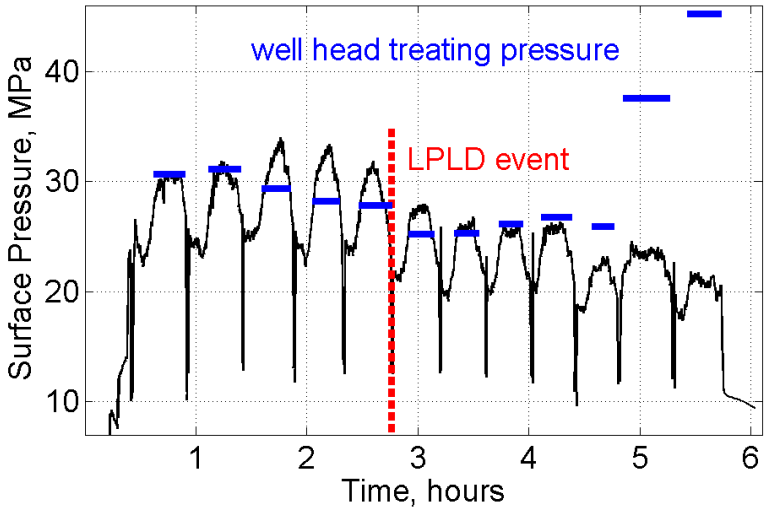

Figure 5.16 – A plot of the surface pressure for 12 stages of the hydraulic fracture treatment. The estimated well head treating pressures to achieve breakdown is shown in blue; fractures were not initiated in the last 4 stages.

Before stage 6, over 30 MPa was required to achieve reservoir breakdown to initiate fractures in the formation. During fracture stage six, there were few microseismic events recorded (Figure 5.17). Numerous microseismic events were recorded for stages 7

through 10. These stages had lower breakdown pressures, maybe indicating weaker reservoirs. There were few events at the end of the treatment, as hydraulic breakdown was not achieved.

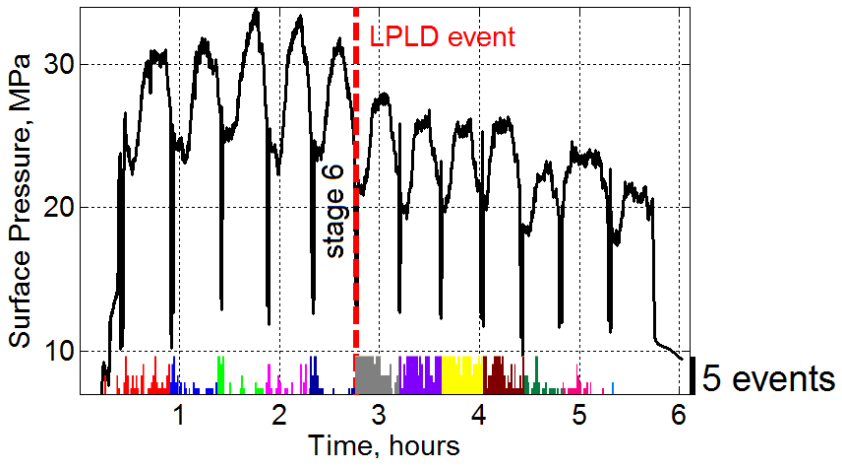

Figure 5.17 – A plot of the surface pressure for 12 stages of the hydraulic fracture treatment with the detected microseismic events. The potential LPLD event occurred at the bleed-off period of the sixth hydraulic stage (the first stage was not pressurized).

5.4.3 Contractor located microseismic events

Figure 5.18 highlights where the contractor located microseismic events for hydraulic fracture stages 4 and 5 (in the upper half of the figure) and 4, 5 and 6 (in the lower half of the figure). The two plan views show interpreted source locations of the detected events with respect to the horizontal well. The upper figure shows the event locations for fracture stage 4 in a green circled "cloud" centered at the stage 4 lateral location ("stage locations" on the figure), as well as a number of events ~ 200 m west.

The events for fracture stage 5 are shown in pink. Most of these events were located to the west of the stage 5 port lateral location. Moreover, most of these events overlay the westerly stage 4 events. The contractor report remarked that the observation well witnessed growth (as defined by event locations propagating outward from the wellbore) in the stage 6 port location during both stage 4 and 5. Specifically, the entire stage 5 appears to have been pumped into the stage 6 area as shown on the bottom half of Figure 5.18, at the location of the contractor interpreted fault. Finally, the stage 6 locations shown in blue are in this same position.

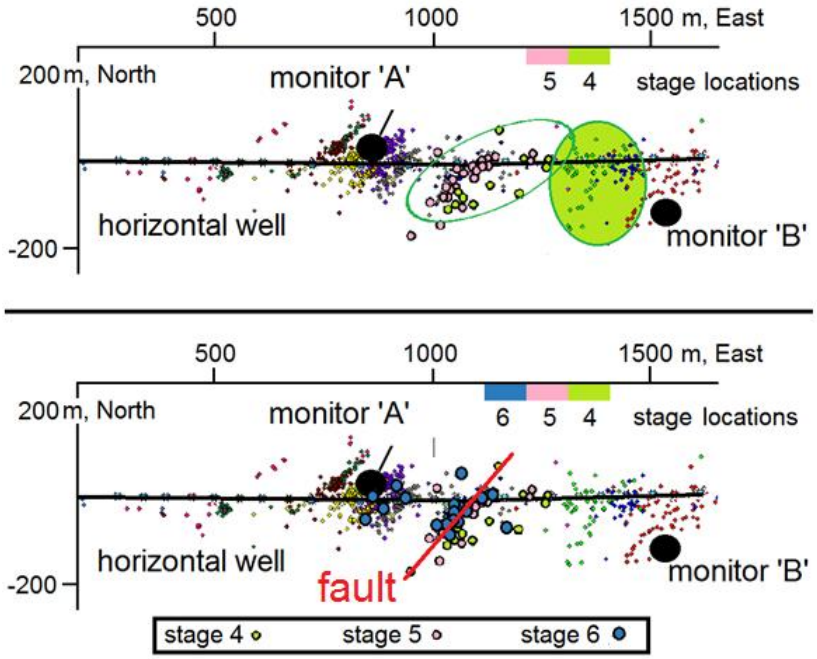

Figure 5.18 – A plan view of the contractor's located events detected using monitor well 'A'. Stage 4 had located events in the green shaded and open green circles (highlighted for effect only, not event magnitude). Stage 5 events were located close to most fracture stage 6 events, as shown on the bottom view. The red North 45° East striking fault is interpreted by the contractor.

Figure 5.19 is a depth view of the stage 6 located events. Also shown on this figure is an estimate of the emergent angles implied by using the Colorado Group and Cardium zone S-wave velocities (~ 2000 m/s, see Figure 4.11) and Figure 5.13. Both Figures 5.18 and 5.19 show good correlation between an anomalous fault and very low frequency microseismic events emanating from the region for 20 s.

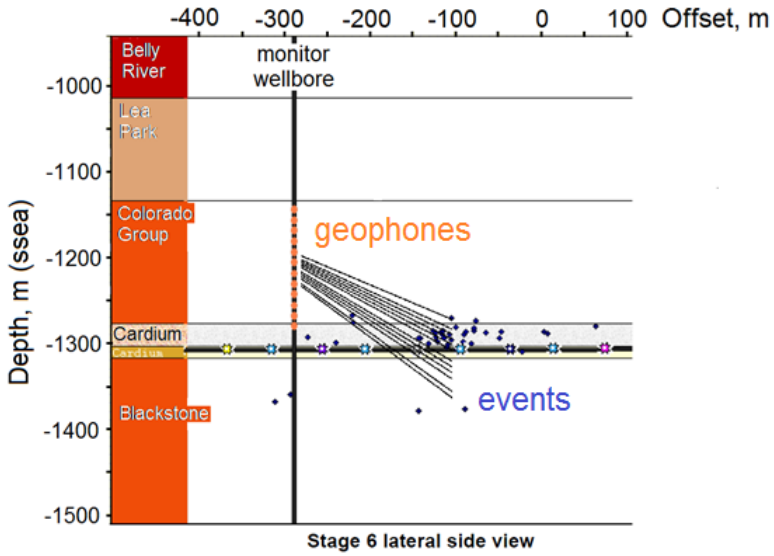

Figure 5.19 - A plan view of the contractor's located events for stage 6 overlain with the calculated emergent angles from Figure 5.11.

5.4.4 Interpreted fault location compared to other results

The interpreted fault in Figure 5.18 can be compared to geological observations, other microseismic data results and the principal stress in the area. Some geological observations are inconclusive. There is evidence of a North 65° West striking fault in the area (Hunter, 1996). Hart and Plint (1993) map a succession of Northwest to Southeast trending thickness variations in the Cardium reservoir on the order of 10 to 20 m that they

attribute to basement structural elements, and, therefore, basement faulting influence. These geological results do not confirm the North 45° East striking fault presented here. However, other geophysical data show good agreement.

Presentations of other microseismic data show compelling results for the initiation of North 45° East trending fractures from hydraulic fracture treatments in the area. Duhault (2012) discusses a number of recent Cardium hydraulic fracture treatments. Most of the treatments had North 45° East striking geometries and should have been along the direction of maximum stress (Figure 5.20). This correlates well with the world stress map shown in Figure 5.20.

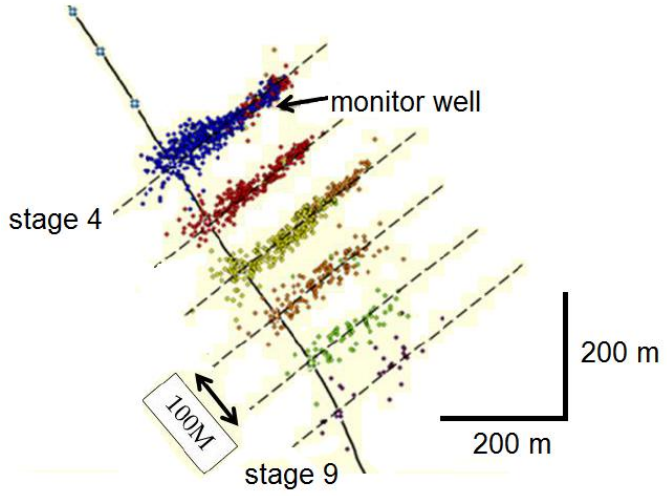

Figure 5.20 - A plan view of the contractor's located events a Cardium hydraulic fracture treatment (from Duhault, 2012).

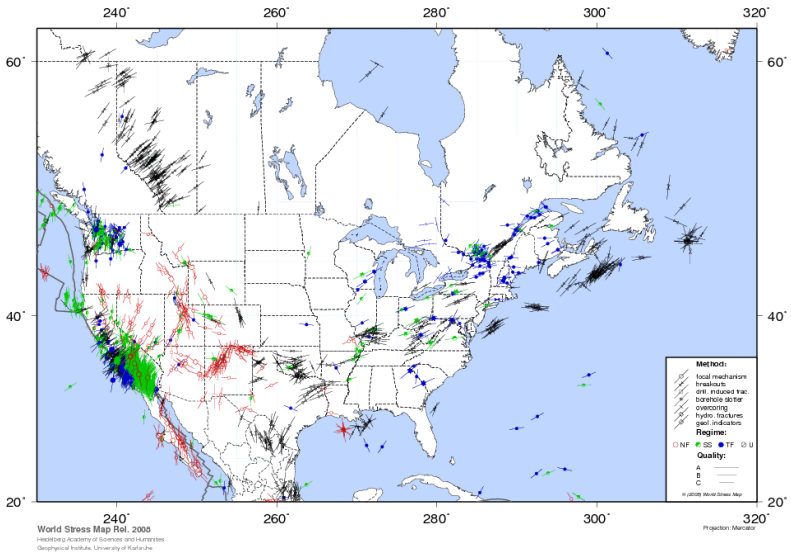

Figure 5.21 – The North America portion of the world stress map showing the North 45° East principal stress direction for Alberta (from Heidbach et al., 2008).

The anomaly presented here is consistent with events identified as LPLD events recorded on microseismic data as reported by Das and Zoback (2012). Their observations and those presented here have many similarities. The anomalies have an upper frequency limit (this study, ~ 60 Hz; Das and Zoback (2012), ~ 100 Hz) that is much lower than P-wave microseismic arrivals that gradually declines as a function of time. There are consistent apparent velocities within both datasets; each LPLD event is composed of multiple adjacent sources within a narrow range of angles. This suggests a localized source area, perhaps representative of movement on a pre-existing fracture or fault.

There are significant differences with respect to relative abundance of LPLD events. Das and Zoback (2012) report multiple LPLD events; we report one event in 5 ½ hours of recording. Eaton et al. (2013) suggested that the abundance of LPLD events may

be related to complexity of the pre-existing fracture network, where more complex fracture networks result in more abundant LPLD activity. It would be constructive to try to examine 3-D surface seismic datasets or reservoir production modeling to examine the possibility of delineating fracture networks with these data as a comparison to the microseismic observations.

The anomaly presented here is similar to events considered to be LPLD events as presented by Eaton et al. (2013). They identify anomalies in the ~ 5 to 30 Hz range as potential LPLD anomalies. However, these anomalies are short in duration (~ 0.1 s). Eaton et al. (2013) also present persistent low frequency recordings in the 8 to 10 Hz and ~15 Hz range that may preclude high frequency microseismic events. These signals have also been interpreted as the resonance of fluid-filled cracks (Tary and van der Baan, 2012), similar to flow-induced oscillation from magmatic fluid travelling within channels (Julian, 1994). We did not observe precursory low frequency tremor prior to the anomaly presented here.

It therefore appears here as though a single LPLD event was generated close to the hydraulic fracture stages and initiated with the "out of area" events for stages 4 and 5. Events initiated early that were interpreted to be a North 45° East fault, consistent with the strike of the principal stress in the area. There were few events for stage 6, but the events were consistent with the strike of the fault. Then the LPLD event occurred at the end of the stage. After this time, the number of microseismic events increased in each of the four successive fracture stages. This increase could have been influenced by a change

in the stress after the LPLD event. The measured emergent angles for the event are consistent with the geometry of the recording array and the fault defined by stages 4, 5, 6.

Das and Zoback (2012) concluded that all of their observations suggest that the LPLD events are generated by slow shear slip on a few preexisting natural fractures due to the high fluid pressure in the reservoir. Das and Zoback et al. (2012) also noted that their LPLD events were from slow slip on faults that are misoriented with respect to the principal stress directions. We could not correlate the source of the events here with existing fractures, as 3-D seismic data were unavailable near the microseismic data presented here. However, the postulated fracture orientation is consistent with results presented by Duhault (2012) and the principal stress direction for Alberta (Heidbach et al., 2008) with a North 45° East strike.

Perhaps the most intriguing observation of the LPLD event presented here is the context of the observed breakdown pressure decreases, the increased number of microseismic events after the event occurrence, the interpretation of a fault, microseismic events laterally occurring out of stage and Figures 3.9 and 3.10 show a change in the borehole acoustic transmissivity after the LPLD event. All of these observations point to a marked change in borehole stress conditions after occurrence of the LPLD event.

5.5 **Conclusions**

A long-period long duration seismic event was identified during the hydraulic stimulation of tight sandstone. The event had numerous closely spaced P- and S-wave arrivals. The interpretation of the microseismic events is consistent with a contractor

mapped North 45° East striking fault at the LPLD event location. This event may have been generated by slow shear slip on a pre-existing natural fracture that had fluid injected by the hydraulic fracture. This process might be contributing significantly to the stimulation. Microseismic data should be examined for other LPLD events to aid in our understanding of the hydraulic fracturing process.

Future work should include the examination of all available 2-D and 3-D seismic data to look for shallow faulting at the Cardium level. Future horizontal wells should be considered for an FMI scanning too to look for *in-situ* fractures. More existing microseismic datasets could be reviewed for potential LPLD events. Detection and mapping of these events could aid in the understanding of existing and induced fracture network complexity.

Chapter Six: Conclusions

This thesis investigates phenomena recorded on microseismic monitoring data that have received little or no attention in the applied geophysics literature. The objective of this thesis is to describe the phenomena using physical principles and to investigate how their properties may be used to increase our understanding of the subsurface. Here, through careful inspection of very large datasets, I have isolated, modelled and interpreted four phenomena recorded on microseismic data in Canada.

Through these studies, I have shown that microseismic data contains more information about the subsurface than is commonly considered in the current paradigm for analysis and interpretation of microseismic data. In the first study, events that appear to be Lamb waves were observed and presented. The waves have a unique apparent velocity and are moderately dispersive. Their apparent velocities were modelled using weak and strong cement casing, indicating the potential application of measured changes in the apparent velocity to monitor for failed cement behind the casing.

In the second study, a frequency phenomenon resembling a comb filter is reported. The resemblance results from the borehole geophones acting as temporally varying boundary conditions for borehole acoustic transmissivity. The observations are robust, occurring for the duration of the monitoring on most of the recording sondes in two datasets. The observations were modeled using an acoustic transfer matrix approach, first presented in the early part of the last century. The results imply that these signals may reflect stress changes external to the wellbore.

The third study examines variations in frequency amplitude spectra observed on microseismic events emanating from an area. A finite difference model was used to show that these variations may be the result of the source depth and geophone location within a reservoir zone. This result could be used to improve focal depth estimation for geolocation algorithms presently being used to locate fracture sources in microseismic data used to monitor hydraulic fractures.

The fourth study examined a unique phenomenon thought to be a long-period long-duration seismic event from hydraulic fracture fluid leaking off into a zone that was not yet targeted during a selective hydraulic fracture treatment. Calculations show that apparent velocities of linear events recorded over 20 seconds could have been caused by a slow slip phenomenon along a possible pre-existing fracture, which are known to occur in the area.

Below, we summarize the four approaches used here to develop a better understanding of microseismic data recorded in boreholes. Next we discuss the major contribution this thesis has made to the scientific community. Finally, we look at some of the directions that future studies could take to continue or branch off from this study.

6.1 Summary of Thesis Work

6.1.1 Lamb Waves

Microseismic data recorded during several hydraulic fracture treatments in western Canada reveal numerous coherent low-frequency (<100 Hz) arrivals characterized by conspicuous dispersion and quasi-linear moveout. The apparent velocities and dispersion characteristics of these events are consistent with Lamb waves, a type of elastic guided wave first described by Lamb (1917) that propagates within finite media such as plates or cylindrical casing. A simple borehole model used as a basis for calculations suggest that Lamb wave speeds are sufficiently sensitive to the shear velocity of cement to enable their use for monitoring degradation of cement over time.

In a thin plate, Lamb waves can be thought of as the superposition of two Rayleigh waves travelling along both sides of the plate (Feenstra, 2005), or alternatively as a coupled P-S_V guided mode. For a cylindrical wellbore, the thin plate is wrapped unto itself. Lamb waves are characterized by discrete modes that arise at certain frequencies. For a wellbore at seismic frequencies, Lamb waves can travel in a longitudinal mode. Some 100 events that appear to be a Lamb wave were observed on one microseismic dataset. A numerical model estimated the apparent velocity of the Lamb waves. This model was adjusted to examine the effect that failed cement in a borehole with no shear strength would have on the Lamb wave velocity. Results show that the change in velocity is on the order of ~200 m/s. This may be enough of a contrast to use Lamb waves as a detection measurement for failed casing cement.

6.1.2 Borehole Acoustic Transmissivity

Passive seismic data from two microseismic datasets acquired in steel-cased boreholes recorded comb-spectra consisting of discrete and narrow pass-bands. The phenomenon can be described by one-dimensional acoustic waves travelling along the steel casing in opposite directions. Clamping of the geophones alters the acoustic properties of the casing, resulting in wave reflections with resulting frequency spectra that has a comb-like appearance. The starting frequency of these pass-bands is predicted by a simple relationship between the P-wave velocity of steel and the clamped geophone spacing distance. The frequency pass-bands are predicted using a very simple acoustic transfer matrix, borrowed from acoustic research, and initially described by Mason (1927).

Analysis of continuous passive recordings during hydraulic-fracture treatments shows that the transmission-band frequencies vary with time and correlate with injection pressures. The results of modeling, coupled with the field observations of injection pressure, indicate that the observed phenomena are related to stress perturbations in the host formation, suggesting a possible novel application of passive seismic monitoring for downhole detection of relative stress changes.

*6.1.3 **Path Effects on Microseismic Data***

P- and S-wave events sampled on microseismic data from one dataset recorded in western Canada during a hydraulic-fracture treatment in western Canada were analyzed to investigate path effects. Seventeen events were grouped into four clusters based upon

a P- and S-wave geolocation algorithm and event cross-correlations. Spectral analysis of the arrivals shows variation in the signal, between and within different sets of events, especially within the 280 to 320 Hz and 440 to 540 Hz frequency bands. A 2-D elastic finite-difference simulation using a layered model shows that this variation could be ascribed to path effects associated with propagation of the signal from the source to the receivers, including wide-angle multiple reflections and head waves. Beyond recognizing their influence on recorded signals, the path effects could be used to group events from the same spatial region and/or depth.

6.1.4 ***Long-period long duration microseismic event***

Passive seismic data recorded in a deep observation wellbore for the hydraulic fracture monitoring of a multi-stage treatment are presented. The data contained an anomalous group of events that persisted for 20 s. This composite event is characterized by low frequency compared to microseismic events, and the individual events had consistent apparent velocities between 3240 and 4890 m/s. The event may be the collection of about 90 individual P- and S-wave arrivals. The anomaly appears to be a long-period long-duration (LPLD) microseismic event, similar to aseismic tremor identified in the past 11 years. LPLD events observed on microseismic data have been likened to deep low frequency tremor attributed to slow-slip processes along pre-existing fractures or strike-slip regimes at subduction zones. A pre-existing fracture in the area at the location of the LPLD event was identified in the original analysis of the microseismic signals. Further identification and analysis of these anomalies should increase our understanding of hydraulic fracture processes.

6.2 General Contributions

Perhaps the most significant contribution of this study is the idea that some uninterpreted signal and some coherent noise recorded on seismic data can provide useful information about the subsurface, effectively turning these observations into signal. Moreover, careful inspection of microseismic data may provide insights that cannot be obtained by automatic algorithms that simply detect and locate P- and S-wave arrivals.

All of the phenomena presented here recurred numerous times on the datasets considered. For example, Lamb waves were observed 96 times on one dataset. The comb-spectra phenomena modeled using an ATM was observed on every trace recording data for 60 hours of microseismic monitoring. The frequency amplitude notches in the path effect study were observed in four different sets of microseismic arrivals. Finally, an interpreted LPLD event was overlooked in the original processing report. It is therefore anticipated that careful inspection of other microseismic datasets will yield other new, unexplained observations. The recognition and explanation of such observations will help to advance the science of microseismic data interpretation.

This study makes a number of contributions to the geophysical interpretation of microseismic data. For example, it may be possible to excite and record Lamb wave velocities in a wellbore over a period of months or years and examine the velocity profiles as a function of time. A change in the Lamb wave speed could be indicative of cement bond failure. This result could be used in conjunction with cement bond loggers and variable density logs that are currently used for cement integrity. Together, the current logs can lead to unambiguous conclusions about the quality of the cement bond

log (Bellabarba et al., 2008); an additional interpretation tool may improve this analysis, particularly in a monitoring context.

The borehole acoustic transmissivity work could lead to a number of applications. There is the potential to record the changes in the transmissivity as a function of time and infer temporal changes in stress around a borehole. Legacy datasets could be examined for this phenomenon and relative stress calculations (as a function of time) could be estimated and calibrated with other external measurements such as strain meters. The acoustic transmissivity was characterized here for all hydraulic fracture initiations for the 9 stages recorded on one dataset. In an area of low S/N for P- and S-wave arrivals, this result could help to monitor the hydraulic fracture initiation at the observation wellbore. Finally, the acoustic transmissivity phenomenon limits the transmission of signal and noise travelling within the steel pipe; this simple fact could be used to improve the S/N of the P- and S-wave energy.

In a general sense, this work adds to the study of phenomenon using time-dependent acoustic transfer matrices. Few other phenomena have been described using time-dependent ATM (for a phenomenon described with a time-dependent ATM, see Polifke and Wall, 2002). It may be possible that there are other applications for this approach and it is hoped that the analysis done here will encourage further developments.

The path effects work has the potential to be used to help cluster P- and S-wave arrivals. Currently, most clustering is done with time difference geolocation algorithms. Grouping events based upon frequency content or modelling source and receiver depth to match frequency spectra could help to confirm and/or refine that clustering. It should be straightforward for contractors to automate this process as they would already have a

velocity model and P- and S-waves identified as a matter of their basic interpretation. Frequency analysis and clustering could easily be added to this processing/interpretation work flow.

6.3 Future Work

As with most studies, new discoveries are accompanied by new questions. Further testing of all hypotheses here is warranted. Experiments could be designed to test Lamb waves for casing integrity. A full-scale or scaled model could be used to measure Lamb wave changes with cement variations. A full numerical model using a finite-difference method or similar approach for simulating low-frequency Lamb waves could be constructed.

The recording of variations in borehole acoustic transmissivity with known external borehole pressures could help to calibrate the observations. Borehole datasets recorded with instrumentation other than the sondes used in this study could be examined for this phenomenon. A more complicated model of the acoustic system (e.g. casing pipe and clamped geophones) could be tested on COMSOL. Lindsay and White (1932) present the governing equations for an acoustic wave in a steel rod with supported spring masses. The work here could be easily modified to test this model.

Future work for path effects analysis could include the examination of other datasets. Hydraulic fracture monitoring from more than one borehole could add significantly to a statistical analysis of the data. The analysis of downhole perforations or "ball-drop" detection (i.e. a steel ball is dropped in the borehole to separate one fracture stage from another by sealing the borehole) during the hydraulic fracture stimulation

could also help to constrain path effect analysis. Finally, perhaps a shallow thick reservoir could be used to test observations of effects from different depths.

It is hoped that more research will commence on some of the phenomena presented in Chapter 4 for this thesis. A more in depth analysis of LPLD events, including 3-D seismic interpretation of existing faults could advance the study of slow-slip earthquakes, especially in Canada. This understanding would be important if slow-slip earthquakes are a phenomenon that releases energy from hydraulic fractures.

It is hoped that future work will build on my interpretation of microseismic data and that the science advances.

Patent application

Most of the work regarding the acoustic borehole transmissibility in Chapter 3 is covered by U.S. Patent Pending No. 13/353,376, Canada Patent Application No. 2,802,572 and United Kingdom Patent Pending No. 1300889.1.

References

Abbott, D., Neale, C., Lakings, J., Wilson, L., Close, J., and E. Richardson, 2007, Hydraulic fracture diagnostics in the Williams Fork Formation, Piceance Basin, Colourado, using surface microseismic technology, SPE 108142.

Abdel-Rahman, S. and S. El-Shaikh, 2009, Diagnosis vibration problems of pumping stations: case studies, 13th International Water Technology Conference, 419-434, accessed at http://water-observatory.net/sources/iwtc2009/6-1.PDF on April 20, 2013.

Achenbach, J. D., 1973, Wave propagation in elastic solids: North Holland, ISBN 0-7204-0325-1.

Aki, K., and P. Richards, 2002, Quantitative seismology, 2nd edition, University Science Books, ISBN-13: 978-1891389634.

Akram, J., and D. Eaton, 2012, Adaptive microseismic event detection and automatic time picking, 2012 GeoConvention, Calgary.

Akram, J., and D. Eaton, 2013, Velocity model calibration effects on microseismic locations, 2013 GeoConvention, Calgary.

Alqahtani, N., Tale, M. and A. Al-Qurishi, 2011, Effect of *in-situ* stress and stresses state conditions on fractured and unfractured, homogeneous and laminated rocks permeability, 81st Annual International Meeting, SEG, Expanded Abstracts, 1804-1808, DOI: 10.1190/1.3627556.

Bale, R., Marrchand, T., Wilkinson, K., Wikel, K., and R. Kendall, 2012, Processing 3-C Heavy Oil Data for Shallow Shear-wave Splitting Properties: Methods and Case studies, CSEG Journal May 2012

Barnes, T., and B. Kirkwood, 1972, Passbands for acoustic transmission in an idealized drill string: Journal of the Acoustical Society of America, **51**, 1606-1608, DOI: 10.1121/1.1913006.

Bellabarba, M., Butle-Loyer, H., Froelich, B., Le Roy-Delage, S., van Kuijk, R., and S. Zeroug, 2008, Ensuring zonal isolation beyond the life of the well, Oilfield Review, 20 (1), 18-31, ISSN: 0923-1730.

Bokov, P. M. and A. M. Ionov, 2001, Excitation of a tube wave in a borehole by an external isotropic point source, Acoustical Physics, **47**, 746-750, DOI: 10.1134/1.1418889.

Boyd, O.S., 2006, An efficient matlab script to calculate heterogeneous anisotropically elastic wave propagation in three dimensions. Computers and Geosciences, 32, 259-264.

Brown, J., Prejean, S., Beroza, G., Gomberg, J., and P. Haeussler, 2013, Deep low-frequency earthquakes in tectonic tremor along the Alaska-Aleutian subduction zone, Journal of Geophysical Research: solid earth, vol. 118, 1079–1090, DOI:10.1029/2012jb009459.

Brown, R., 2005, Stress-dependent fracture compliance, 75th Annual International Meeting, SEG, Expanded Abstracts, 135-138, DOI: 10.1190/1.2142222.

Burago, N. A., A. S. Ibatov, P. V. Krauklis, and L. A. Krauklis, 1980, Dispersion of tube and Lamb waves recorded in acoustic logging, Journal of Mathematical Sciences, **20**, 2401-2407, DOI: 10.1007/BF01087286.

Butler, R., 1994, Horizontal wells for the recovery of oil, gas, and bitumen, The Petroleum Society of the Canadian Institute of Mining, Metallurgy and Petroleum, Calgary, ISBN:0-9697990-1-2.

Butrenchuk, E., Cornish, S., Leggitt, S., and M. Mills, 1995, The impact of facies on reservoir performance: Pembina Cardium reservoir, Alberta, CSPG/CWLS 1995 Core Session, The Economic Integration of Geology and Formation Evaluation, 47-78.

Canada National Energy Board, 2009, A primer for understanding Canadian shale gas, NEB, Ottawa.

CAPP, 2012, Canadian Association of Petroleum Producers Statistical Handbook 2012, accessed at http://www.capp.ca/library/statistics/handbook/Pages/default.aspx on 30 April 2013.

Carcione, J., and F. Poletto, 2000, Simulation of stresS-waves in attenuating drill strings, including piezoelectric sources and sensors: Journal of the Acoustical Society of America, 108, 53 – 64, DOI: 10.1121/1.429443.

Castagna, J.P., M. L. Batzle, and R. L. Eastwood, 1985, Relationships between compressional-wave and shear-wave velocities in clastic silicate rocks: Geophysics, **50**, 571-581

Chambers, K., and J.-M. Kendall, 2010, Investigation of induced microseismicity at Valhall using the Life of Field Seismic array, The Leading Edge, **29 (3)**, 290-295, DOI: 10.1190/1.3353725.

Chen, S., and G. Atkinson, 2002, Global comparisons of earthquake source spectra, Bulletin of the Seismological Society of America, **92**, 885-895.

Chung, H.-M., and D. Lawton, 1999, A quantitative study on the effects of tuning on AVO effects for thin beds, Canadian Journal of Exploration Geophysicists, 35 (12), pp. 36-42.

CSUR, 2013, Hydraulic Fracturing (brochure), Canadian Society for Unconventional Resources, Calgary.

Das, I. and M. Zoback, 2011, Long-period, long-duration seismic events during hydraulic fracture stimulation of a shale gas reservoir, The Leading Edge, **30 (7)**, 778-786, DOI: 10.1190/1.3609093.

Das, I. and, Zoback, M., 2012, Microearthquakes associated with long period, long duration seismic events during stimulation of a shale gas reservoir, SEG Technical Program Expanded Abstracts 2012: 1-5, DOI: 10.1190/segam2012-1484.1.

Davies, J., 2008, Inspection of pipes using low frequency focused guided waves, Ph. D. Thesis, Imperial College, http://www3.imperial.ac.uk/nde/publications/phd%20theses, accessed on April 20, 2013.

Dickens, P., France, R., Smith, J., and J. Wolfe, 2007, Clarinet acoustics: introducing a compendium of impedance and sound spectra, Acoustics Australia, **35**, 17-23, DOI: 10.1.1.165.2118.

Drumheller, D., 1989, Acoustical properties of drill strings, Journal of the Acoustical Society of America, **85**, 1048-1064, DOI: 10.1121/1.2026251.

Drumheller, D., 2002, Wave impedances of drill strings and other periodic media, Journal of the Acoustical Society of America, **112**, 2527-2539, DOI: 10.1121/1.1513365.

Duhault, J. (2012) Cardium formation hydraulic "frac" microseismic: observations and conclusions. SEG Technical Program Expanded Abstracts 2012: 1-5, DOI: 10.1190/segam2012-0835.1

Eaton, D., and F. Forouhideh, 2011, Solid angles and the impact of receiver-array geometry on microseismic moment-tensor inversion, Geophysics, **76**, WC77-WC85, DOI: 10.1190/geo2011-0077.1.

Eaton, D., and N. Boroumand, 2013, Estimating energy balance for hydraulic fracture stimulations: lessons learned from Basel, Geoconvention 2013 Technical Program Expanded Abstracts, Calgary

Eaton, D., van der Baan, M., Tary, J., and Pike, K., 2013, Low-frequency tremor signals from a hydraulic fracture treatment in northeast British Columbia, Canada, Geoconvention 2013 Technical Program Expanded Abstracts, Calgary

Eberhard, M., 2011, Fracture Design Stimulation – Monitoring Workshop, Haliburton Workshop, March 10-11, 2011, Denver.

Eisner, L., Thornton, M., and J. Griffin, 2011, Challenges for microseismic monitoring, 81st Annual International Meeting, SEG, Expanded Abstracts, DOI/10.1190/segam2012-1519-1523.

Faber K., and P. Maxwell, 1997, Geophone spurious frequency: what is it and how does it affect seismic data quality?, Canadian Journal of Exploration Geophysicists, **33**, 46-54.

Fagan, D., 2012, Statistical clustering of microseismic event spectra to identify subsurface structure, M. Sc. Thesis, Boise State University.

Farghal, N., and S. Levin, 2012, Hunting for microseismic reflections using multiplets, 82nd Annual International Meeting, SEG, Expanded Abstracts, DOI:/10.1190/segam2012-1422.1.

Feenstra, P., 2005, Modeling and Control of Surface Acoustic Wave Motors, Ph. D. Thesis, University of Twente, http://doc.utwente.nl/50813/1/thesis_Feenstra.pdf, accessed on April 20, 2013.

Fic, J., Plumridge, T., Pedersen, P., and M. Spila, 2011, Reservoir architecture of the Cardium Formation in East Pembina, Alberta, Expanded abstracts, Recovery – 2011 CSPG CSEG CWLS Convention, Calgary.

Forgues, E., Schisselé-Rebel, E., and J. Cotton, 2011, Simultaneous Active/Passive Seismic Monitoring of Steam Assisted Heavy Oil Production, 81st Annual International Meeting, SEG, Expanded Abstracts, 4082-4086, DOI: 10.1190/1.3663401.

Fu, Q., and Y. Luo, 2009, Locating micro-seismic epicentres in common arrival time domain, 79th Annual International Meeting, SEG, Expanded Abstracts, 1647-1651, DOI: 10.1190/1.3255166.

Fung, Y., A. Kaplan and E. Sechler, 1955, On the vibration of thin cylindrical shells under internal pressure: The Ramo-Woodridge Corporation, http://www.dtic.mil/dtic/tr/fulltext/u2/605578.pdf accessed 1 January, 2013

Gaiser, J., Fulp, J., Petermann, S., and G. Karner, 1988, Vertical seismic profile sonde coupling, Geophysics, 53 (**2**), 206-214, DOI: 10.1190/1.1442456.

Galvagni, A., and P. Cawley, 2010, The reflection of guided waves from simple supports on pipes, Journal of the Acoustical Society of America, **129**, 1869-1880, DOI: 10.1121/1.3543958.

Gazis, D., 1959, Three-dimensional investigation of the propagation of waves in hollow circular cylinders. I. Analytical foundation: The Journal of the Acoustical Society of America, **31**, 568-578, DOI:10.1121/1.1907753.

Grandi-Karam, S., 2008, Multiscale determination of *in-situ* stress and fracture properties in reservoirs, PhD Thesis, Massachusetts Institute of Technology, accessed at http://erl.mit.edu/lab-reports.php on April 20, 2013.

Graves, R., and R. Clayton, 1992, Modeling path effects in three-dimensional basin structures, Bulletin of the Seismological Society of America, **82**, 81-103.

Greenhalgh, S., B. Zhou, D. Pant, and A. Green, 2007, Numerical study of scattering and waveguide excitation in faulted coal seams, Geophysical Prospecting, **55**, pp. 185-198.

Haimson, B. C., and F. Cornet, 2003, ISRM suggested methods for rock stress estimation – Part 3: hydraulic fracturing (HF) and/or hydraulic testing of pre-existing fractures (HTPF): International Journal of Rock Mechanics and Mining Sciences, **40**, 1011-1020, DOI:10.1016/j.ijrmms.2003.08.002.

Hardage, B., 2001, Developments, trends and future directions in vertical seismic profiling and crosswell seismic profiling, CSEG Recorder, September 2001, 73-78.

Hart, B., and A. Plint, 1993, Tectonic influence of deposition and erosion in a ramp selling: Upper Cretaceous Cardium Formation, Alberta Foreland Basin, The American Association of Petroleum Geologists, **22 (12),** 2092-2106.

Hatchell, P., and S. Bourne, 2005, Rocks under strain: Strain-induced time-lapse shifts are observed for depleting reservoirs: The Leading Edge, **24 (12)**, 1222-1225, DOI: 10.1190/1.2149624.

Hawkes, C., Bachu, S., Haug, K., and A. Thompson, 2005, Analysis of *In-situ* stress regime in the Alberta Basin, Canada for performance assessment of CO_2 geological sequestration sites, Fourth Annual Conference on Carbon Capture and Sequestration DOE/NETL Proceedings, Virginia.

Hayles, K., Horine, R., Checkles, S., and J. Blangy, 2011, Comparison of microseismic results from the Bakken Formation processed by three different companies: Integration with surface seismic and pumping data, 81st Annual International Meeting, SEG, Expanded Abstracts, 1468-1472, DOI: 10.1190/1.3627479.

Heidbach, O., Tingay, M., Barth, A., Reinecker, J., Kurfeß, D., and Müller, B., 2008, The World Stress Map database release 2008, DOI:10.1594/GFZ.WSM.Rel2008, 2008

Hickman, S., and M. Zoback, 1983, The interpretation of hydraulic fracturing pressure-time data for *in-situ* stress determination, in Hydraulic Fracturing Stress Estimates, National Earthquakes Hazard Reduction Program, U.S. National Committee for Rock Mechanics

Hogan, C. and D. Eaton, 2012, Path effects in subsurface microseismic monitoring, The Leading Edge, **31**, 1326-1329.

Holditch, S., 2006, Tight gas sands, Journal of Petroleum Technology, June 2006, SPE 103356.

Hunter, V., 1996, Possible basement influence on cretaceous Cardium sand body orientations in the Garrington area, Alberta Basin, B. Sc. Thesis, McMaster University, accessed at http://digitalcommons.mcmaster.ca on May 31, 2013.

Johnston, R., and J. Shrallow, 2011, Ambiguity in microseismic monitoring, , 81st Annual International Meeting, SEG, Expanded Abstracts, 77-81, DOI: 10.1190/1.3627490.

Julian, B. R., 1994, Volcanic tremor: Nonlinear excitation by fluid flow, Journal of Geophysical Research, **99**, 11859-11977, DOI: 10.1029/93JB03129.

Kanasewich, E. R., 1981. Time Sequence Analysis in Geophysics, The University of Alberta Press, DOI: 10.2307/3314985-a.

Karpfinger, F., 2009, Modelling borehole wave signatures in elastic and poroelastic media with spectral method, Ph. D. Thesis, Curtin University of Technology, Australia, http://link.library.curtin.edu.au/p?cur_digitool_dc131194, accessed on October 31, 2012.

King, P., 2007, Acoustic properties of periodically and quasi-periodically modulated waveguides. M. Sc. Thesis, The University of Salford

King, P., and T. Cox, 2007, Acoustic band gaps in periodically and quasiperiodically modulated waveguides: Journal of Applied Physics, **102**, 014902, DOI: 10.1063/1.2749483.

Kocon, K. and van der Baan, M., 2012, Quality assessment of microseismic event locations and traveltime picks using a multiplet analysis, The Leading Edge, 31(11), 1330–1337, DOI: 10.1190/tle31111330.1

Kumano, Y., Asanuma, H., Hotta, A., Niitsuma, H., Schanz, U., and M. Häring, M., 2007, Reservoir structure delineation by microseismic multiplet analysis at Basel, Switzerland, 2006. SEG Technical Program Expanded Abstracts 2007, 1271-1276, DOI: 10.1190/1.2792735

Kwong, A. and K. Edge, 1998, A method to reduce noise in hydraulic systems by optimizing pipe clamp locations, Proceedings of the Institution of Mechanical Engineers, Part 1: Journal of Systems and Control Engineering, **212**, 267-280, DOI: 10.1243/0959651981539451.

Lakings, J., Duncan, P., Neale, C., and T. Theiner, 2006, Surface based microseismic monitoring of a hydraulic fracture well stimulation in the Barnett shale. 76th Annual International Meeting, SEG, Expanded Abstracts, 605-608, DOI: 10.1190/1.2370333.

Lamb, H., 1917, On waves in an elastic plate, Proceedings of the Royal Society, London, 114-128, DOI: 10.1098/rspa.1917.0008.

Lawn, B, and T. Wilshaw, 1975, Fracture of Brittle Solids, Cambridge University Press, ISBN: 0521206545, 9780521206549.

Lei, T., Bikash, S., and M. Sanders, 2012, Estimation of horizontal stress magnitudes and stress coefficients of velocities using borehole sonic data, Geophysics, **77 (3)**, WA181-WA196, DOI: 10.1190/geo2011-0277.1.

Lermo, J., and F. Chavez-Garcia, 1993, Site effect evaluation using spectral ratios with only one station, Bulletin of the Seismological Society of America, **83**, 1574-1594.

Li, Y. and P. C. Leary, 1990, Fault zone trapped seismic waves. Bulletin of the Seismological Society of America **80 (5)**, 1245–1271.

Li, C., Dohmen, T., Morton, S., Katahara, K., Hayles, K., Checkles, S., and J. Blangy, 2012, Evaluating the quality of microseismic event locations, 82th Annual International meeting, SEG, Expanded Abstracts, DOI:10.1190/segam2012-1155.1.

Lines, L., K. Kelly, K., and J. Queen, 1992, Channel waves in cross-borehole data, GEOPHYSICS, **57**, 334–342.

Linsday, R. B. and F. E. White, 1932, The theory of acoustic filtration in solid rods: Journal of the Acoustical Society of America, **34**, 155-168, DOI: 10.1121/1.1915598.

Linsday, R. B. and F. E. White, 1934, The theory of acoustic filtration in solid rods: Journal of the Acoustical Society of America, 34, 155-168, DOI: 10.1121/1.1915598.

Linsday, R. B., 1929, Note on the theory of acoustic wave filters, Physical Review, 34, 652-655, DOI: 10.1103/PhysRev.34.652

Linsday, R. B., 1934, Filtration of elastic waves in solid rods, Journal of the Acoustical Society of America, V, 196-200, DOI: 10.1121/1.1915648.

Liu, E., S. Crampin, and B. Roth, 1992, Modeling channel waves with synthetic seismograms in an anisotropic in-seam seismic survey, Geophysical Prospecting, **40**, 513-540.

Liu, G., and Y. Li, 2011, Vibration analysis of liquid-filled pipelines with elastic constraints: Journal of Sound and Vibration, **330**, 3166-3181, DOI: 10.1016/j.jsv.2011.01.022.

Long, R., M. Lowe, and P. Cawley, 2003, Attenuation characteristics of the fundamental modes that propagate in buried iron water pipes, Ultrasonics, 41, pp. 509-519, DOI: 10.1016/S0041-624X(03)00166-5.

Lou, M., and S. Crampin, 1993, Modelling guided waves in cross-hole surveys in uncracked and cracked rock, Geophysical Prospecting, **41**, 241-265.

Lous, N., Rienstra, S., and I. Adan, 1998, Sound transmission through a periodic cascade with applications to drill pipes: Journal of the Acoustical Society of America, **103**, 2302-2311, DOI: 10.1121/1.422749.

Mahob, P. and J. Castagna, 2001, The use of polarization attributes to identify anomalies: AVO hodograms, 72nd Annual International Meeting, SEG, Expanded Abstracts, 203-206, DOI: 10.1190/1.1816545.

Maity, D. and F. Aminzadeh, 2012, Framework for time lapse fracture characterization using seismic, microseismic & well log data. SEG Technical Program Expanded Abstracts 2012: pp. 1-6, DOI: 10.1190/segam2012-0387.1

Marfurt, K., Schneider, R., and M. Mueller, 1996, Pitfalls of using conventional and discrete Radon transforms on poorly sampled data, Geophysics, **61**, 1467-1482, DOI: 10.1190/1.1444072.

Markos, P., and C. Soukoulis, 2008, Wave propagation: From Electrons to Photonic Crystals and Left-Handed Materials, Princeton University Press, ISBN: 9780691130033

Mason, W. P., 1927, A Study of the Regular Combination of Acoustic Elements, with Applications to Recurrent Acoustic Filters, Tapered Acoustic Fibers, And Horns, Bell System Technical Journal, **6**, 258-294, accessed on May 31, 2013 at http://www3.alcatel-lucent.com/bstj/vol06-1927/articles/bstj6-2-258.pdf

Maxwell, S. and F. Reynolds, 2012, Guidelines for Standard Deliverables from Microseismic Monitoring of Hydraulic Fracturing, CSEG, Calgary.

Maxwell, S., Rutledge, J., Jones, R., and M. Fehler, 2010, Petroleum reservoir characterization using downhole microseismic monitoring, Geophysics, **75 (5)**, 75A129-75A137, DOI: 10.1190/1.3477966.

Maxwell, S., Urbancic, T., Falls, S., and R. Zinno, 2000, Real time microseismic mapping of hydraulic fractures in Carthage, Texas, 70th Annual International Meeting, SEG, Expanded Abstracts, 10.1190/1.1815677..

Mayerhofer, M., Lolon, E., Warpinski, N., Cipolla, C., Walser, D. and C. Rightmire, 2010, What is stimulated reservoir volume, SPE Production and Operations, 25, 89-98, DOI: 10.2118/119890-PA.

McCollum, B., and W. LaRue, 1931, Utilization of existing wells in seismograph work, AAPG Bulletin, December 1931, v. 15, p. 1409-1417.

McGillivray, P., 2004, Microseismic and time-lapse monitoring of a heavy oil extraction process at Peace River. SEG Technical Program Expanded Abstracts 2004: 572-575, DOI: 10.1190/1.184241.

McNamara, B., 2012, Production data from the Cardium Formation evaluated within a geologic framework to identify criteria useful in selecting areas for exploitation

by multi-stage fracturing of horizontal wells, AAPG Search and Discovery Article #20158 (2012).

Microseismic Inc website, accessed on May 17, 2013 at http://www.microseismic.com/about/history

Mostafa, A., Amorin, R., Brazil, E., Eaton, D., Carpendale, S., Sharlin, E., and M. Costa Souza, 2012, Exploratory visual modeling and analysis of microseismic events, 2012 GeoConvention, Calgary.

National Energy Board, 2011, Tight oil developments in the western Canadian Sedimentary Basin, Ottawa

Nobakht, M. and C. Clarkson, 2013, Hybrid Forecasting Methods for Multi-Fractured Horizontal Wells: EUR Sensitivities, Advances in Petroleum Exploration and Development, **3 (1),** 1-10, DOI:10.3968/j.aped.1925543820120301.152

Obara, K., 2002, Nonvolcanic deep tremor association with subduction in southwest Japan, Science, **296**, 1679–1681, DOI: 10.1126/science.1070378.

Partyka, G., Gridley, J., and J. Lopez, 1999, Interpretational applications of spectral decomposition in reservoir characterization, *The Leading Edge*, 18(3), 353–360, DOI:

Pettitt, W., Reyes-Montes, J., Hemmings, B., Hughes, E., and P. Young, 2009, Using continuous microseismic records for hydrofracture diagnostics and mechanics, 79th Annual International Meeting, SEG, Expanded Abstracts, 1542-1546, DOI: 10.1190/1.3255143.

Pickett, G. R., 1963, Acoustic character logs and their application in formation evaluation, Journal of Petroleum technology, **15**, 659-667, DOI: 10.2118/452-PA.

Pike, K., and D. Eaton, 2013, Impact of low velocity coals on microseismic data processing, Spirit River Formation: preliminary results, 2013 Microseismic Industry Consortium Sponsors Meeting, Calgary

Polifke, W., and Wall, C., 2002, Non-reflecting boundary conditions for acoustic transfer matrix with large-eddy simulation, Centre for Turbulence Research, proceedings of the Summer Program 2002, Stanford University.

Raggio, L., J. Etcheverry, and N. Bonadeo, 2007, Determination of acoustic shear and compressional wave velocities for steel samples by impulse excitation of vibrations, IV Conferencia Panimericana de END, Buenos Aires, October 2007, accessed on April 20, 2013, at: http://www.ndt.net/article/panndt2007/papers/34.pdf.

Rajagopal, P., 2007, Towards higher resolution guided wave inspection: scattering studies, Ph. D. Thesis, Imperial College, London, accessed on April 20, 2013, at: http://www3.imperial.ac.uk/nde/publications/phd%20theses.

Rama Rao, V. N., and J. K. Vandiver, 1999, Acoustics of fluid-filled boreholes with pipe: Guided propagation and radiation, Journal of the Acoustical Society of America, **105**, 3057-3066, DOI: 10.1121/1.424635.

Rocha-Gaso, M., C. March-Iborra, A. Ángel Montoya-Baides, and A. Arnau-Vives, 2009, Surface Generated Acoustic Wave Biosensors for the Detection of Pathogens: A Review, Sensors, **209**, 5740-5769, DOI: 10.3390/s90705740.

Rogers, G. and H. Dragert, 2003, Episodic tremor and slip on the Cascadia subduction zone: the chatter of silent slip, Science 300 1942, DOI: 10.1126/science.1084783

Rost, S. and C. Thomas, 2002, Array seismology: Methods and applications, Reviews of Geophysics, **40**, 1008, DOI: 10.1029/2000RG000100.

Rutledge, J., Phillips, W., and M. Mayerhofer, 2004, Faulting induced by forced fluid injection and fluid flow forced by faulting: an interpretation of hydraulic-fracture microseismicity, Carthage Cotton Valley gas field, Texas, Bulletin of the Seismological Society of America, **94 (5)**, 1817-8130, DOI: 10.1785/012003257.

Scherbaum, F., 1994, Basic concepts in digital signal processing for seismologists, Springer-Verlag.

Schmitt, D. R., Currie, C., and L. Zhang, 2012, Crustal stress determination from boreholes and rock cores: Fundamental principles, Tectonophysics, **580**, 1-26, DOI: 10.1016/j.tecto.2012.08.029.

Schmitt, D., Smither, C., Ahrens, T. and B. Jensen, 1986, Borehole in-situ holographic stress and elastic moduli measurements. 66th Annual International Meeting, SEG, Expanded Abstracts, 9-12, DOI:10.1190/1.1892954.

Schoenberg, M., Marzetta, T., Aron, J., and R. Porter, 1981, Space-time dependence of acoustic waves in a borehole, Journal of the Acoustical Society of America, 70, 1496-1507, DOI: 10.1121/1.387107.

Segall, P., Desmarais, E., Shelly, D., Miklius, A., and P. Cervelli, 2006, Earthquakes triggered by silent slip events on Kilauea volcano, Hawaii, Nature, 442, 71-74, DOI:10.1038/nature04938.

Seibel, M., Baig, A., and T. Urbancic, 2010, Single versus multiwall microseismic recording: what effect monitoring configuration has on interpretation, Expanded Abstracts, SEG 80th Annual Meeting, DOI/10.1190.13513251

Selamet, A., Dickey, N., and J. Novak, 1995, Theoretical, computational and experimental investigation of Helmholtz resonators with fixed volume: lumped versus distributed analysis, Journal of Sound and Vibration, **187**, 358-367, DOI: 10.4271/940612.

Shabelansky, A., Malcolm, A., Fehler, M., and S. Bakku, 2012, Seismic imaging of hydraulically-stimulated fractures: a numerical study of the effect of the source mechanism, 2012 SEG Annual Meeting Expanded Abstracts, November 4-9, 2012, Las Vegas, Nevada, DOI: 10.1190ésegam2012-1182.1.

Shelly, D. R., G. C. Beroza, S. Ide, and S. Nakamula, 2006, Low frequency earthquakes in Shikoku, Japan, and their relationship to episodic tremor and slip: Nature, **442**, 188–191, DOI:10.1038/nature04931.

Silk, M. G., and K. F. Bainton, 1979, The propagation in metal tubing of ultrasonic waves modes equivalent to Lamb waves, Ultrasonics, **17**, pp. 11-19, DOI: 10.1016/0041-624X(79)90006-4.

Singh, K., and A. Mallik, 1979, Parametric instabilities of a periodically supported pipe conveying fluid, Journal of Sound and Vibration, **62**, 379-397, DOI: 10.1016/0022-460X(79)90631-X.

Song, I., Suh, M., Won, K., and B. Haimson, 2001, A laboratory study of hydraulic fracturing breakdown pressure in table-rock sandstone, Geosciences Journal, 5 (3), 263-271, DOI: 10.1007/BF02910309.

St-Onge, A., 2010. Akaike information criterion applied to detecting first arrival times on microseismic data, 80th Annual International Meeting, SEG, Expanded Abstracts, DOI/10.1190.13627522.

St-Onge, A., and D. Eaton, 2011, Noise examples from two microseismic datasets, CSEG Recorder, October, 2011, 46-49.

Stevens, J. L. and S. M. Day, 1986, Shear velocity logging in slow formations using the Stoneley wave, GEOPHYSICS, **51**, 137–147, DOI: 10.1190/1.1442027.

Stewart, G. W., 1922, Acoustic wave filters, Physical Review, **20**, 528-551, DOI: 10.1103/PhysRev.20.528.

Suckale, J., 2010, Moderate-to-large seismicity induced by hydrocarbon production, *The Leading Edge*, **29**, 310–319, DOI: 10.1190/1.3353728.

Tary, J.-B., van der Baan, M., and D. Eaton, 2013, On the interpretation of resonance frequencies recorded during microseismic experiments, geoconvention 2013, Expanded abstracts.

Tary, J., and M. van der Baan, 2012, Potential use of resonance frequencies in microseismic interpretation, The Leading Edge, 31, 1338-1346.

Teanby, N., J.-M. Kendall, R. H. Jones and O. Barkved, 2004, Stress-induced temporal variations in seismic anisotropy observed in microseismic data, Geophysical Journal International, **156**, 459-466.

Todorov, T., and Margrave, G., 2010, CDP noise attenuation using local linear models, CREWES Research Report, 80, **22**.

Urbancic, T., and A. Baig, 2013, Using microseismicity to identify and verify increased fracture complexity during hydraulic fracture stimulations, Geoconvention 2013, Expanded abstracts.

Valko, P., and M. Economides, 1995, Hydraulic Fracture Mechanics, John Wiley & Son, New York, ISBN: 0471956643.

Virgin, L. N., 2007, Vibration of axially loaded structures, Cambridge University Press, New York, ISBN: 9780511460647.

Walter, W. R. and J. N. Brune, 1993. Spectra of seismic radiation from a tensile crack, Journal of Geophysical Research, **98,** 4449–4459, DOI: 10.1029/92JB02414.

Warpinski, N., 2009, Microseismic monitoring: inside and out, Journal of Petroleum Technology, November 2009, pp. 80-85, DOI: 10.2118/118537-MS.

Warpinski, N.R., Wright, T.B.,Uhl, J.E., Engler, Drozda, P.M., Peterson, R.E., and Branagan, P.T., 1996, Microseismic Monitoring of the B-Sand Hydraulic Fracture Experiment at the DOE/GRI Multi-Site Project SPE Annual Technical Conference andExhibition, 6-9 October 1996, Denver

Wayland, J., and D. Lee, 1986, Seismic mapping of EOR processes, GEOPHYSICS: the Leading Edge of Exploration, **5**, 36-40, DOI/10.1190/1.1439209

Yilmaz, O., 2001, Seismic data analysis: processing, inversion and interpretation of seismic data, SEG Books, Tulsa, ISBN: 978-1-56080-094-1.

Youzwishen, C. and G. Margrave, 1999, Finite difference modeling of acoustic waves in MATLAB: CREWES Research Report 11, accessed at: http://nut.geo.ucalgary.ca/ForOurSponsors/ResearchReports/1999/1999-06.pdf on December 6, 2012

Zimmer, U., 2011, Microseismic design studies, GEOPHYSICS, **76**, WC17 – WC25, DOI: 10.1190/GEO2011-0004.1.

Zoback, M., Kohli, A., Das, I., and M. McClure, 2012, The importance of slow slip on faults during hydraulic fracturing stimulation of shale gas reservoirs, SPE 155476.

Appendix 1 – Lamb waves

Consider a free plate, thickness *h*, as shown in Figure A-1. As discussed by Davies (2008), P- and S_V waves are coupled in a free plate. The stress-free surfaces at $y = \pm h/2$ on the plate confines the P and S_V vectors to have the same wavevector component in the *z* direction k_z, $s = k_z$, *l*, as shown in Figure A-2. The two wave vectors prescribe two circles of radii k_s and kl whose axial component kz must match for a propagating modal solution. These conditions lead to the Rayleigh-Lamb frequency equations for a plate.

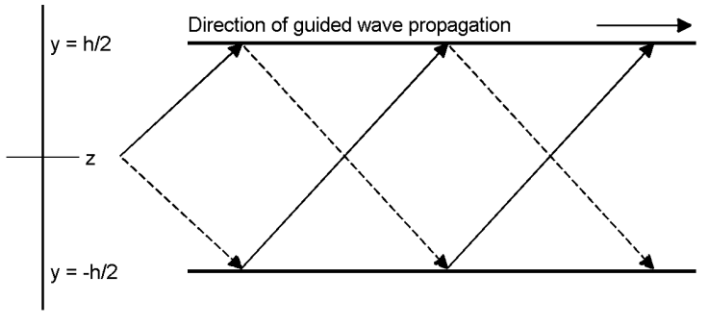

Figure A-1 – Free plate schematic showing geometry for internally reflected body waves (from Davies, 2008). The plate has a thickness h and traction-free surfaces.

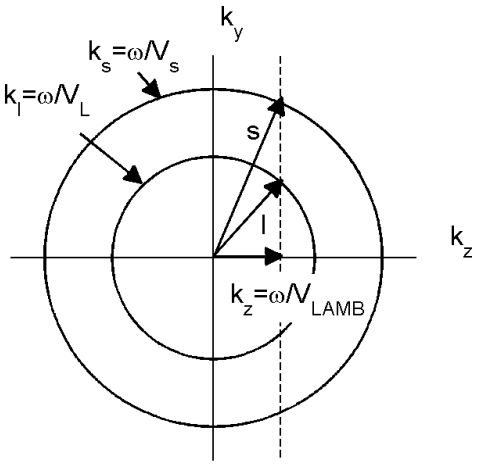

Figure A-2 – Wavenumber graphical representation of the free plate dispersion relation for coupled S_V and P partial waves (from Davies, 2008). Here k represents wavenumber, ω represents angular velocity and V represents velocity. The axial components of k_s and k_l are required to be the same.

Appendix 2 - Lamb Frequency Equations for a Free Plate

Formulation of the dispersion curves comes from the solution of the period equation, as presented in Achenbach (1973), for symmetric and asymmetric waves, respectively.

$$\frac{tan(qh)}{tan(ph)} = \frac{-4k^2\,pq}{(q^2-k^2)^2} \qquad \text{Symmetric} \qquad \text{(A-1)}$$

$$\frac{tan(qh)}{tan(ph)} = \frac{-(q^2-k^2)^2}{4k^2pq} \qquad \text{Antisymmetric} \qquad \text{(A-2)}$$

Where $p^2 = \frac{\omega^2}{c_L^2} - k^2$, p = longitudinal wavenumber,

$q^2 = \frac{\omega^2}{c_T^2} - k^2$, q = transverse wavenumber,

$c_L = \sqrt{\frac{\lambda+2\mu}{\rho}}$ (longitudinal velocity), $c_T = \sqrt{\frac{\mu}{\rho}}$ (transverse velocity),

$\mu = \frac{E}{2(1+\upsilon)}$, $\lambda = \frac{E\upsilon}{(1-2\upsilon)(1+\upsilon)}$, Lame constants

E = Young's modulus, υ = Poisson's ratio , ω = circular frequency, k = wave number, ρ = density, h = plate thickness

Solution(s) for (A-1) and (A-2) can be evaluated numerically.

Appendix 3 - Dispersion Code

In Chapter 2 of this thesis, we use Karpfinger's (2009) numerical approach for simulating wave propagation in cylindrically layered model for Lamb waves. His algorithm is based on the spectral method, meaning that the underlying governing equations are discretized using spectral differentiation matrices. This results in the formulation of a generalized eigenvalue problem. For a given frequency, the eigenvalues correspond to the axial wavenumbers of different modes. The code is available on the SEG website for software, http://software.seg.org/GEOindex.html.

Appendix 4 - Processing to isolate the line spectra

For the borehole acoustic transmissivity in Chapter 3, an algorithm was developed to isolate components of these comb spectra as a function of time, to facilitate further analysis of the time varying nature of the signals. This algorithm was implemented using MATLAB software to detect and catalog these frequencies. First, the raw data were segmented into successive records, usually two seconds in duration. Each segment was transformed to the frequency domain using a Fourier transform, and the MATLAB "findpeaks" algorithm was used to detect local data peaks. The initial frequency in the comb-spectrum was estimated by dividing the geophone array spacing distance into the velocity of steel and input as an initial guess for the "findpeaks" algorithm. This frequency was tracked for the duration of the dataset. All of the higher frequencies in the comb-spectrum were estimated by scaling the initial guess by 5/4, 6/4. 7/4, etc.

Appendix 5 - Derivation of Acoustic Transfer Matrix

Markos and Soukoulis (2008) discuss the transfer matrix method for the analysis of the wave propagation in one-dimensional systems. A compression wave travelling in a cylindrical wellbore with azimuthal symmetry is a one-dimensional system. For the velocities and dimensions of wellbore casing, a compression wave can be treated as a plane wave. A general transfer matrix relating acoustic pressure, Φ, and volume velocity, U, based upon King (2007), is derived below. Consider Figure A-3.

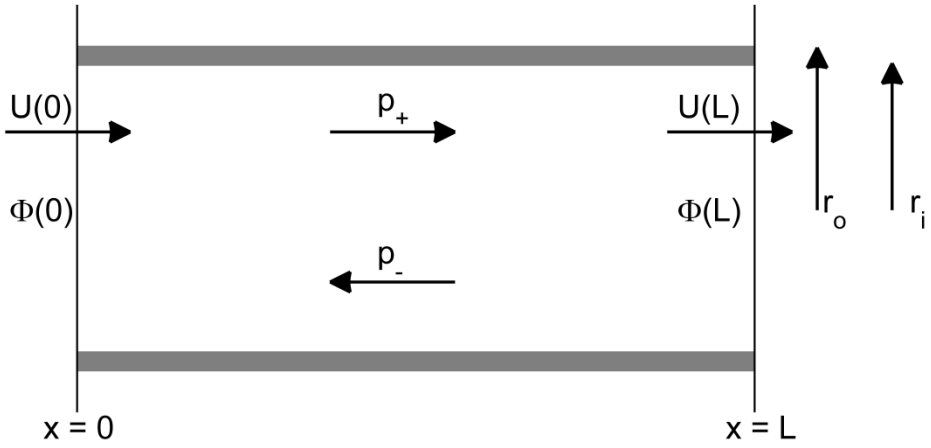

Figure A-3 – a schematic representation of a cut away cylinder where plane waves can travel either left to right (p+) or right to left (p-). The cylinder has diameters defined by radii r_i and r_o (inner and outer, respectively).

The transfer matrix relating the acoustic pressure, Φ, and volume velocity U (or particle velocity u times the surface area $S = \pi(r_o^2 - r_i^2)$) , at x = 0 to x = L can be written as a function of angular frequency ω as:

$$\begin{pmatrix} \Phi(0) \\ U(0) \end{pmatrix} = \begin{pmatrix} A(\omega) & B(\omega) \\ C(\omega) & D(\omega) \end{pmatrix} \begin{pmatrix} \Phi(L) \\ U(L) \end{pmatrix} \tag{A-3}$$

The coefficients A, B, C, and D can be calculated using the boundary conditions:

$$A(\omega) = \frac{\Phi(0)}{\Phi(L)}, at\ U(L) = 0, \qquad B(\omega) = \frac{\Phi(0)}{U(L)}, at\ \Phi(L) = 0$$

$$C(\omega) = \frac{U(0)}{\Phi(L)}, at\ U(L) = 0, \qquad D\ (\omega) = \frac{U(0)}{U(L)}, at\ \Phi(L) = 0$$

There can exist right and left travelling plane waves within the cylinder. The total pressure as a function of time t and distance x within the cylinder is given by their sum:

$$\Phi(x, t) = p_+ e^{j(\omega t - kx)} + p_- e^{j(\omega t + kx)} \tag{A-4}$$

where ω = angular frequency, k = wavenumber.

Considering Euler's equation:

$$u = -\frac{1}{\rho_0 c} \int \frac{\partial \Phi}{\partial x} dt \tag{A-5}$$

Where u = particle velocity, ρ_0 = density, c = velocity.

Substituting (A-2) into (A-3) gives the particle velocity u(x, t):

$$u(x,t) = \frac{1}{\rho_0 c}\left(p_+ e^{j(\omega t - kx)} - p_- e^{j(\omega t + kx)}\right) \tag{A-6}$$

If we substitute *U(x, t)* =*S*u(x, t)*, (A-4) also gives the volume velocity:

$$U(x,t) = \frac{S}{\rho_0 c}\left(p_+ e^{j(\omega t - kx)} - p_- e^{j(\omega t + kx)}\right) \tag{A-7}$$

Where S = the cylinder cross section area = $\pi(r_o^2 - r_i^2)$.

For U(L) = 0, (A-7) becomes:

$$\frac{S}{\rho_0 c}\left(p_+ e^{j(\omega t - kL)} - p_- e^{j(\omega t + kL)}\right) = 0$$

$$\xrightarrow{which\ yields} \frac{p_+}{p_-} = e^{2jkL} \tag{A-8}$$

Similarly, for $\Phi(L) = 0$, (A-8) becomes:

$$p_+ e^{j(\omega t - kL)} - p_- e^{j(\omega t + kL)} = 0$$

$$\xrightarrow{which\ yields} \frac{p_+}{p_-} = -e^{2jkL} \tag{A-9}$$

Consider $A(\omega) = \frac{\Phi(0)}{\Phi(L)}, at\ U(L) = 0,$ and (A-8) and (A-9):

$$A(\omega) = \frac{\Phi(0)}{\Phi(L)}, at\ U(L) = 0, = \frac{(p_+ + p_-)e^{j\omega t}}{(p_+ e^{-jkL} + p_- e^{jkL})(e^{j\omega t})}$$

$$= \frac{\frac{p_+}{p_-} + 1}{\frac{p_+}{p_-} e^{-jkL} + e^{+jkL}} \tag{A-10}$$

Combining (A-7) with (A-9) yields: $A(\omega) = \cos(kL)$. Similarly, $B(\omega) = j\rho_0 cS \sin(kL)/S$, $C(\omega) = jS \sin(kL)/\rho_0 c$, and $D(\omega) = \cos(kL)$

Now (A-3) can be rewritten after substitution for A, B, C, and D:

$$\begin{pmatrix} \Phi(0) \\ U(0) \end{pmatrix} = \begin{pmatrix} \cos(kL) & j\frac{\rho_0 c}{S}\sin(kL) \\ j\frac{S}{\rho_0 c}\sin(kL) & \cos(kL) \end{pmatrix} \begin{pmatrix} \Phi(L) \\ U(L) \end{pmatrix} \tag{A-11}$$

Equation (A-11) can be used to define what frequencies will be transmitted along a repeated structure such as a cylinder with restrictions.

Appendix 6 – Borehole finite element model

COMSOL Multiphysics Software version 4.3a was used to model a hollow steel cylinder. The 24.74 m long hollow steel cylinder has an inner radius = 0.10 m and an outer radius = 0.117 m centered at (0, 0, 12.37). Internal restrictions using 0.001 m thick disks were place at z = -12.37, 0.0, and 12.37 m. A union was formed with the discs and the cylinder. The ends of the cylinders were repeated in both (-) and (+) z directions (periodic condition). The outer edges of the cylinder were treated as hard boundaries. The cylinder had a P-wave velocity of 5780 m/s and a density of 7800 kg/m^3. A power edge source was place at (0, 0, 6.18) on the outer edge of the cylinder and a power of 10 W/m was used. A fine mesh was used and swept from the front of the cylinder to the back. A boundary probe was placed at (0, 0, 0) where the total acoustic pressure field was measured using (acpr.p_t) in the acoustics module. Frequencies were swept from 200 to 4000 Hz in 20 Hz steps. A stationary, parametric, linear solver was used to solve for 64945 degrees of freedom in 11 minutes. The physics solved for was pressure acoustics, frequency domain, as defined by

$$\nabla \cdot \rho^{-1} (\nabla p) - k^2 p/\rho = Q \qquad \text{(A-12)}$$

where, ρ = density = 7800 kg/m^3, k^2 = (ω/V) ^{2}, p = pressure (Pa), Q = monopole source.